Hybrid RANS/LES Modelling of OGV/Prediffuser Flow

Jinghua Li

Department of Aeronautical and Automotive Engineering

Loughborough University

A thesis submitted for the degree of

Doctor of Philosophy

Yet to be decided

I would like to dedicate this thesis to my loving parents ...

Acknowledgements

Abstract

In the gas turbine engine, the OGV/prediffuser combination is key to achieve a good design for combustor external aerodynamics. Since the flow includes 3D turbulent wakes and boundary layers in adverse pressure gradients with the possibility of flow separation, the OGV/prediffuser combination offers significant turbulence modelling challenges for CFD. In order to understand the optimum approach for modelling turbulence in this important sub-component of compressor/combustor interaction, a comparison is reported in this thesis with available experimental data for both a conventional and an advanced OGV/prediffuser combination using (i) both high Re and low Re RANS CFD, (ii) LES CFD, and (iii) hybrid RANS/LES CFD. In the hybrid RANS/LES CFD, a new method based on the use of an Algebraic Stress Model and a modified Recycling and Rescaling method has been developed to generate a spatially and temporally correlated unsteady velocity field for the LES inlet conditions from the time-averaged RANS solution at OGV exit. The results show that:

- Both high Re and low Re RANS solutions show good agreement with the experimental data for the OGV wake prediction, but high Re RANS provides better predictions of overall pressure loss and is certainly more cost effective considering computing costs.

- The LES solution shows partial flow separation of the OGV suction side boundary layer prediction which was not noted in the experiment. This is probably caused by the presence of relaminarisation and subsequent transition of the suction side OGV boundary layer. This places high demands on the LES near wall mesh required, as well as providing an extreme challenge for the LES sub grid scale model.

- The Hybrid RANS/LES approach is able to provide a good balance of predictive capability, matching RANS predictions on global performance (pressure rise/loss) and improving the prediction of velocity distribution at prediffuser exit, and it thus offers an optimum approach for OGV/prediffuser flow simulation considering both accuracy and cost.

Contents

List of Figures

Nomenclature

Roman Symbols

A area

C_{pd} static pressure recovery through the prediffuser

C_{pV} static pressure recovery through the vane row

C_p static pressure recovery

C_s Smagorinsky constant

d distance from the wall

H total enthalpy

k turbulent kinetic energy

L integral length scale

$\dot{m}$ mass flow rate

N_x, N_y, N_z grid size on direction x,y,z

$\widetilde{P}$ mass-weighted total pressure

$\widetilde{p}$ mass-weighted static pressure

P pressure

P_{ij} production tensor

P_k production of turbulent kinetic energy

Q Q-criterion

R_{ij} The pressure strain term

Re Reynolds number

Re_L Reynolds number based on integral length scale

Re_t turbulent Reynolds number

S magnitude of strain rate tensor

S_{ij} strain rate tensor

t time

$\overline{u}_i$ Reynolds averaged mean velocity component; spatially filtered velocity component (LES)

$u_i^{'}$ fluctuating velocity component

$u_i(x, y, z, t)$ instantaneous velocity component

Greek Symbols

α latency parameter

$\Delta_x, \Delta_y, \Delta_z$ grid size in the relevant direction

ϵ dissipation rate of turbulent kinetic energy

ϵ^* isotropic dissipation rate

Γ blending function

γ ratio of specific heats

λ overall total pressure loss

λ_d total pressure loss through the prediffuser

λ_V total pressure loss through the vane row

μ dynamic viscosity

μ_L molecular dynamic viscosity

μ_t turbulent dynamic viscosity

ν kinematic viscosity

ν_r eddy viscosity

ν_t turbulent kinematic viscosity

ω specific dissipation rate

$\overline{\Delta}$ filter length

ρ density

τ_{ij}^{Sr} the deviatoric part of the SGS stress tensor

τ_{ij}^{S} SGS stress tensor

τ_{ij} stress tensor

Superscripts

$'$ fluctuating part of Reynolds decomposition

$\overline{()}$ Reynolds averaged mean value; spatially filtered value (LES)

n previous time level

$n+1$ new time level

Subscripts

i index

j index

k index

l index

$target$ target value

x Cartesian coordinate

y Cartesian coordinate

z Cartesian coordinate

SGS   subgrid scale

Other Symbols

$\langle\rangle$ spatially averaged over grid cells

Acronyms

ASM Algebraic Stress Model

CFD Computational Fluid Dynamics

$DDES$ Delayed DES

DES Detached Eddy Simulation

DNS Direct Numerical Simulation

FV Finite Volume

LES Large Eddy Simulation

LNS Limited Numerical Scales

OGV Outlet Guide Vane

R^2M Rescaling/Recycling Method

$RANS$ Reynolds-Averaged Navier-Stokes

SGS Sub-Grid Scale

TVD Total Variation Diminishing

Chapter 1

Introduction

1.1 Background

Since the 1960s, with the advent of high-speed digital computers, combined with the development of algorithms for solving systems of partial differential equations, a revolution in the study and practice of fluid dynamics has taken place. A fundamentally new approach to fluid dynamics – Computational Fluid Dynamics (CFD) – was introduced as a complement to the existing approaches of experimental and theoretical fluid dynamics. CFD uses numerical methods, algorithms and – most important for the topic of the present thesis – models of turbulence to solve and analyse fluid flow problems, i.e. to simulate numerically the turbulent motion of fluids (liquids or gases) in regions of space contained within surfaces defined via appropriate boundary conditions.

During the past five decades CFD has evolved rapidly and contributed much to solution of a wide range of problems in both research and engineering design. Historically the early development of CFD was driven by the needs of the aerospace community and CFD has been enthusiastically embraced in aerospace design and research ever since. All major aircraft manufacturers: Boeing, Airbus, Lockheed Martin, Dassault Aviation, and aircraft propulsion system providers: General Electric, Pratt & Whitney and Rolls-Royce, as well as supporting national research institutes (such as ONERA, DLR) have developed numerous in-house CFD

codes and used these extensively for the study of aircraft and propulsion systems. Much of this industrial development was of course initiated and underpinned by university-based research into numerical methods and mathematical models for important physical phenomena, such as turbulence, combustion etc. The success of these fundamental CFD developments has also created a wide selection of commercial CFD software (FLUENT, CFX, STARCCM etc).

The gas-turbine engine industry has been at the forefront of development and use of CFD for research and design. Today, numerical simulation tools are routinely used to investigate all aspects of gas turbine aerothermal design and performance, e.g. compressor and turbine blade aerodynamics, heat transfer, combustor design, aeroacoustics, etc. In the turbomachinery components of the gas turbine, flows are strongly three-dimensional, unsteady (both because of the relative motion between successive rotor/stator blade rows and also because of the turbulent nature of the flow at high Reynolds numbers), and viscous effects play a dominant role due to the presence of laminar, transitional and fully turbulent boundary layers, as well as possible boundary-layer separation with flow recirculation and secondary flows. To simulate such flows as precisely as possible, prediction requires an accurate and computationally affordable description of the turbulent processes that influence the efficiency (and hence the losses) inherent in any compressor or turbine design. A number of flow solvers developed specifically for turbomachinery fluid dynamics have been in use in industry for many years. These flow solvers are typically based on the Reynolds-Averaged Navier-Stokes approach (RANS)[10][11] either in its steady flow format, or allowing for temporal resolution of blade rotation (unsteady RANS or URANS). In both cases, the instantaneous unsteady flow-field is first decomposed into a mean (averaged) field and a stochastic or turbulent fluctuating field. In RANS the mean flow is statistically stationary, whereas for URANS the mean contains a periodic component related to blade rotation. The governing fundamental equations (the exact Navier-Stokes equations for Newtonian fluids) are then ensemble-averaged (URANS) or time-averaged (RANS). In this approach statistical turbulence models are then introduced to represent the effects of the fluctuating turbulence on the mean flow (For a general introduction into the subject of turbulence and its

modelling, see Pope[12]). Since turbomachinery flows have been a subject of investigation for many years, experience has shown that, in many circumstances, statistical turbulence models have been adequately calibrated and hence good results for turbomachinery performance prediction can often be achieved using the (U)RANS approach [13][14].

In contrast to turbomachinery flow, the combustion system of the gas turbine engine, because it involves multiple strongly interacting phenomena (extremely high intensity turbulent mixing, heat transfer, radiation, chemical reaction and multiphase flow), represents a significantly greater modelling challenge. The turbulent fuel/air mixing in particular is typically dominated by large energetic eddy structures[15]. As a consequence, in the last 10 years the view has arisen that steady state RANS computations are, at best, only a crude approximation of such flows. Numerical models capable of providing the necessary accuracy for the flow in gas-turbine combustors are now viewed as needing to take more explicit account of the dynamics of the energetic turbulent motions than is possible even via (U)RANS modelling [16]. The Large Eddy Simulation (LES) approach has been considered an attractive alternative to RANS statistical models for predicting flows such as those in combustion systems (For a general introduction into the subject of LES, see Sagaut[17]). Pierce and Moin [18], for example, have shown the superiority of LES to RANS in accurately predicting turbulent mixing and combustion dynamics in a simple coaxial combustor configuration. Kim and Syed [19] and Mongia[20] provide a detailed overview of the importance and role of LES in designing advanced gas turbine combustors. Apart from application to modelling simple flames, Moin et al.[21] and Boudier et al.[1] have extended the LES methodology to geometrically complex and realistic configurations. Figure 1.1 shows, via two examples taken from [1], the complex geometry typical of combustors, and the detailed flow features visible in LES predicted temperature contours.

The question of which approach to turbulence modelling is optimal is of course also a question of the balance between computational cost versus predictive accuracy. This question has been brought to the fore in the latest development of CFD in its application to gas turbine technology, namely whole engine modelling.

(a) Combustion chamber

(b) Predicted instantaneous temperature
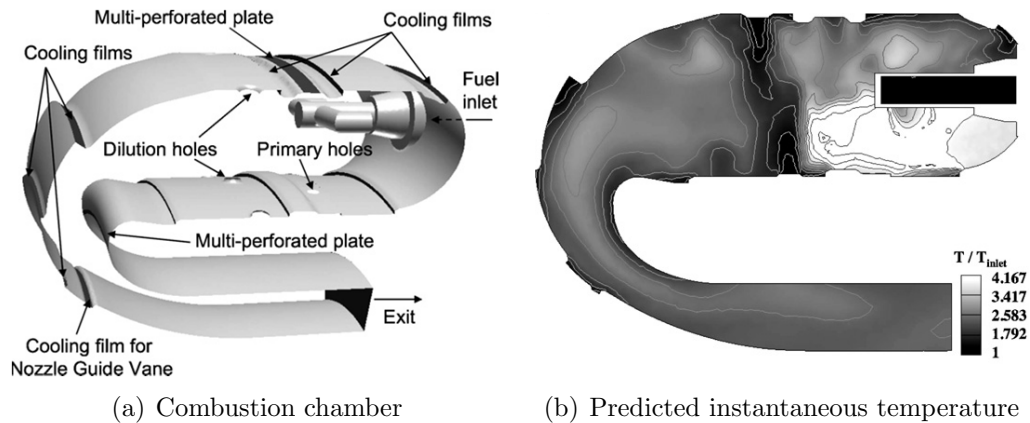
Figure 1.1: Turbomeca combustion chamber considered for LES in an industrial context (taken from[1])

Whilst the vast majority of CFD application to propulsion systems has been to the individual separate components (e.g. fan, compressor, turbine, combustor, intake, nozzle, etc.), the ambition to take advantage of prediction and modelling for the whole engine is such a huge computational challenge that it has only become possible recently with the appearance of large multi-processor compute clusters. The best examples of this work are the publications emerging from the Stanford group, e.g. [2][22][23][24][25], and Figure 1.2 provides an illustration of this research. In order to maintain the balance between accuracy and cost, the route chosen by the Stanford group has been to apply different flow solvers and turbulence modelling approaches to different components, for example (U)RANS for compressor and turbine, but LES for the combustor.

This highlights a third approach to turbulence modelling of complex flows – using hybrid RANS/LES. The development of such a hybrid approach raises many questions which require detailed research, such as the best technique for interfacing two different turbulence modelling methods, and perhaps also how to couple different flow solvers used for different components. For more details on application of hybrid methods to compute an entire gas turbine jet engine, see Medic et al. [26].

The topic of coupling different components of an engine via a hybrid turbulence
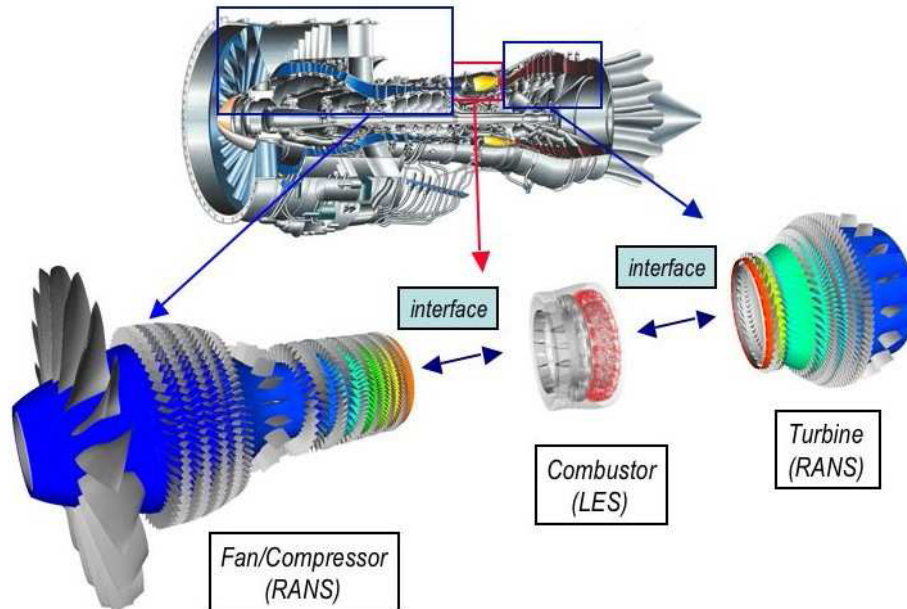
Figure 1.2: Decomposition of the engine for flow simulation. Compressor and turbine with (U)RANS; Combustor with LES.(Taken from[2])

modelling approach has also found application in other areas of CFD and engineering (e.g. Hamba[27] applied hybrid RANS/LES method to channel flow, and Georgiadis et al.[28] used it to predict supersonic turbulent mixing). In the gas turbine application, as seen in Figure 1.2, the compressor/combustor interface is the first and most obvious choice for studying and developing improvements in the hybrid approach. The research to be described in this thesis is thus focused directly on the hybrid approach to turbulence modelling and its application to one particular aspect of the compressor/combustor interface. The following two sections are included to provide relevant information and previous work in the two areas of: (i) the compressor/combustor interface flow physics and (ii) approaches to turbulence modelling, before stating the specific aims and objectives of the present work.

1.2 Review of Compressor/Combustor Interface Flow Characteristics

1.2.1 General Background

In a gas turbine, the combustor is where fuel is injected into the high pressure, high temperature air ($\approx 900K$) provided by the compressor, and burns to produce hot products ($\approx 1800K$) at combustor exit to feed the turbine to provide thrust. In the conventional 'rich-burn' combustor design which dominates current gas turbine technology, the combustor geometry must manage the airflow to create a flow pattern that is conducive to maintain stable combustion despite very high air flow rates. Hence, combustors are carefully designed to mix and burn the fuel with part of the compressor efflux, and then mix in more air to complete the combustion process and dilute the hot gases to produce an exit temperature profile acceptable to the turbine design. Some of the compressor air is also used to cool the combustor walls. Figure 1.3 shows a cross-section through a typical fully-annular rich-burn combustor. This can be divided into four regions: the diffuser system (which represents the 'heart' of the compressor/combustor interface), the inner and outer feed annuli, and the liner (or flametube) flow region (including fuel injector, primary/dilution ports and wall cooling devices).

Modern aircraft gas turbine design requires that the compressor produces a high pressure rise ($\approx 40{:}1$) in a minimum number of stages. As a consequence, the air leaves the compressor at a reasonably high Mach number ($\approx 0.3\text{-}0.4$) and with a high degree of swirl ($\approx 45^o$). Efficient stable combustion with small total pressure losses can, however, only be achieved if the air velocity is significantly reduced by flow diffusion. Moreover, the compressor efflux, which feeds the fuel injector and also enters the combustor via several other locations, must be supplied to all the entry ports into the combustor in a controlled manner. This ensures favourable conditions to achieve the design values of flow split, port discharge coefficients, and primary/dilution jet momentum ratios/jet trajectory angles for appropriate depth of jet penetration at minimised pressure loss. Thus, the design of the diffuser and external aerodynamics aspects of the compressor/combustor interface
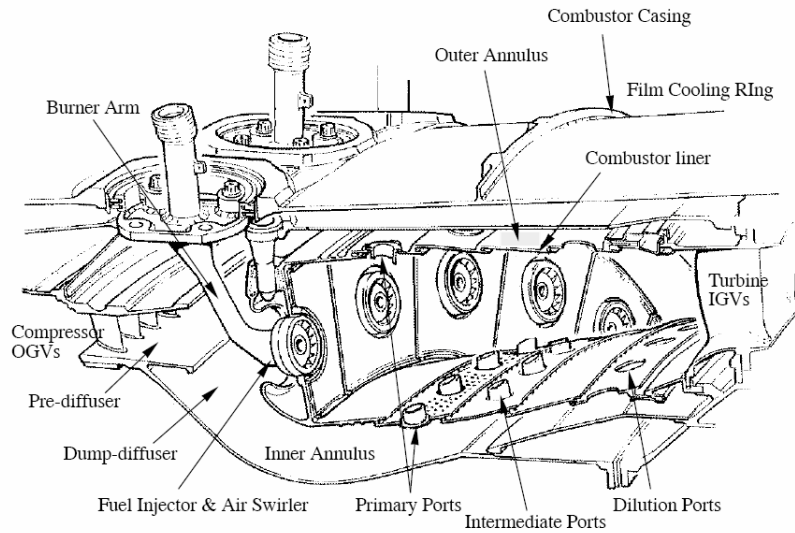
Figure 1.3: Section through a rich burn fully annular combustor

is a challenging task.

The need to decrease the velocity magnitude in order to avoid high total pressure losses in the combustor has led to the use of several types of diffusers, including so-called 'faired' and 'dump' diffusers [29] [3] or a combination of these in the so-called 'prediffuser/dump diffuser' configuration, which has become the standard design during the last 20 years.

Figure 1.4(a) shows a typical 'faired diffuser' common in early 1960's engines. The advantage of the faired diffuser is low pressure loss in the outer and inner passages. Despite this, the configuration also has disadvantages. First, the design can lead to small annulus heights in the inner and outer annuli, and manufacturing tolerance and differential thermal expansion/distortion give rise to significant variations in diffuser geometry with detrimental effects on performance [29]. A second disadvantage of the faired design is its strong sensitivity to the non-uniformities in the compressor outlet velocity profile. Finally, the requirement for considerable length is also a drawback. For area ratios approaching those typically required to achieve low pressure loss designs, the axial length of a faired

(a) Faired diffuser

(b) Dump diffuser
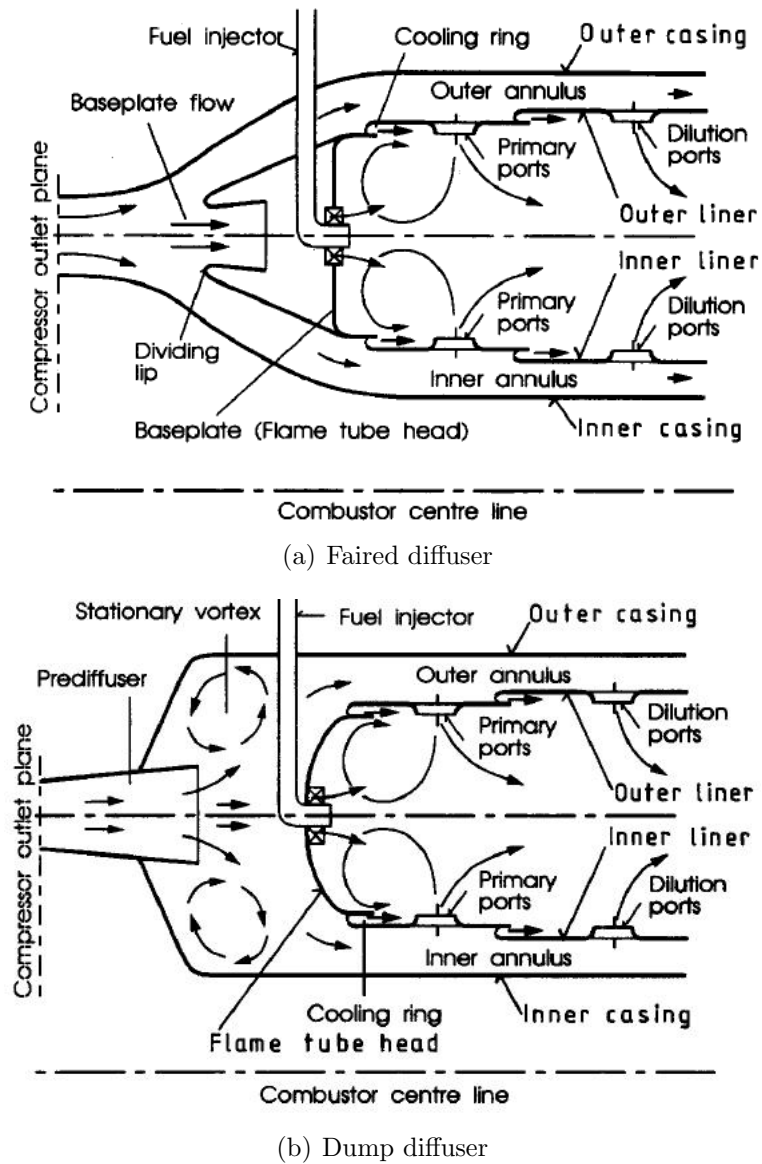
Figure 1.4: Two types of combustor diffusers (taken from [3])

diffuser (to avoid flow separation) becomes unacceptably large. Consequently, these severe drawbacks make this configuration unsuitable for modern engines [3]. In an attempt to overcome these problems, modern engines have adopted the prediffuser/dump diffuser arrangement, as shown in Figure 1.4(b). The combination of an annular prediffuser immediately behind the compressor outlet guide vane (OGV) row, followed by a sudden expansion dump diffuser has been found to provide an attractive combination of stability for a relatively wide range of inlet conditions, short length and reasonably low pressure loss. This design has thus become universally adopted by all engine manufacturers and for all thrust levels. Nevertheless, there are aspects of the design of this type of diffuser system that are still challenging and fluid mechanically complex, and these are discussed next.

1.2.2 Prediffuser/Dump Diffuser System Aerodynamics

In a diffuser system consisting of a combination of a short faired prediffuser and a dump diffuser, the flow downstream of the last compressor rotor first has to pass through the last row of stator vanes in the compression system (the Outlet Guide Vanes – OGVs) in order to reduce the significant swirl velocity component created by the rotor and turn the flow into the axial direction. This means that the first stage of flow diffusion – in the annular faired prediffuser – has to be designed taking the presence of the strong 3D OGV wakes and associated turbulence structure into account, as well as the end-wall boundary layers on the inner/outer walls of the annular gas path. It is the low momentum regions of these wakes and boundary layers which effectively constrain the maximum area ratio achievable in a given length of prediffuser. Separation has to be avoided and this will occur when the low momentum flow passing into the prediffuser is unable to sustain forward motion against the adverse pressure gradient created by the increasing prediffuser area. The design target for the prediffuser is therefore to achieve the lowest dynamic head possible at prediffuser exit in a given length without the flow separating, whilst still representing a "robust" design capable of coping with various inlet conditions provided by the compressor over its operating range. The pressure loss in the downstream dump diffuser is essentially

one prediffuser exit dynamic head. It is also found that there is some benefit in optimising the 'dump gap' – the axial distance between prediffuser exit and the head region (cowl) of the combustor. The impingement of the prediffuser exit flow on the combustor cowl creates a high static pressure region, which has an upstream influence in subsonic flow. Thus, choosing an appropriate dump gap ($\approx$ 1 prediffuser exit height in a typical rich burn design) can help to keep the prediffuser flow attached since the higher pressure in the central portion of prediffuser exit (generated from the upstream influence of cowl impingement) will drive flow towards the inner/outer walls and hence "re-energise" the decelerating wall boundary layers to enable a higher area ratio whilst still avoiding separation.

In the dump region, the flow divides into three streamtubes which feed fuel injector and inner/outer annuli. The annulus feed streams consist essentially of annular jets whose curvature is set by the dump gap, the combustor height and the cowl head radius, undergoing free surface diffusion before entering the annuli. Because of the sudden expansion dump loss, this system has a higher total pressure loss than an equivalent faired diffuser but is much shorter (a factor of $\approx$ 3) and is a design found to be much more robust to changes in engine operating conditions which lead to prediffuser inlet condition variations (although see below for a more detailed discussion of this inlet condition issue). In a well designed system, experimental investigations have shown [29] that most of the loss occurs in the dump region, while most of the static pressure recovery occurs in the prediffuser.

The above brief description of the important fluid mechanical aspects that influence prediffuser/dump diffuser systems has shown that even this sub-component of the engine offers significant modelling challenges for CFD. In particular the control of the OGV/diffuser interaction is key to achieving a good design. This is no simple task, since the flow includes 3D wakes, turbulence, boundary layers, adverse pressure gradients and the possibility of the flow approaching separation. Further, the OGV/prediffuser combination corresponds to an element of a turbomachinery flow (OGV) in which RANS CFD may well be the best choice, and a close to separating duct flow (prediffuser) in which LES CFD may offer an

opportunity for increased accuracy of predictions. It is therefore argued here that the OGV/prediffuser combination is a good test problem for the study of hybrid RANS/LES and hence previous work on this flow combination is reviewed next.

1.2.3   Previous Work on OGV/prediffuser flows

Immediately downstream of the compressor OGV row, large variations of the flow properties exist in both circumferential and radial directions and rapid mixing out take place in the axial direction. This strong 3D flow is due to (i) the wakes created by the merged boundary layers that develop on the OGV blade surfaces, (ii) the end wall boundary layers and (iii) the secondary flows caused by the radial and azimuthal forces exerted on the flow by the (often spanwise varying) OGV blade cross-section. These secondary flows are often largest near the hub and the casing. Thus, compressor OGV/diffuser/combustor flow interaction has been of great interest in both experimental (Fishenden and Stevens [29]) and CFD studies of combustor external aerodynamics (Karki et al. [30]; Koutmos and McGuirk [31]; Shyy[32]). Emphasis has focussed on developing an understanding and predictive capability for the flow associated with a prescribed OGV/prediffuser/combustor geometry in terms of the resulting pressure loss, and the quality of air feed to injector, flame tube ports, etc. Klein [3] has reviewed numerous diffuser investigations that are relevant to the aero gas turbine combustor application, which show that the prediffuser flow in particular can be very sensitive to inlet conditions.

A basic OGV/prediffuser combination is shown schematically in Figure 1.5; for convenience it is useful to consider the performance of this sub-system, subject to specified inlet conditions at OGV inlet (created by the upstream compressor design chosen), and specified outlet conditions at prediffuser exit (created by the combustor geometry and dump diffuser chosen). Significant previous work with diffusers located behind axial compressors has been reported. For example, Stevens et al. [33; 34] investigated the performance of a diffuser operating downstream of a multi-stage axial compressor and also with fully developed ax-
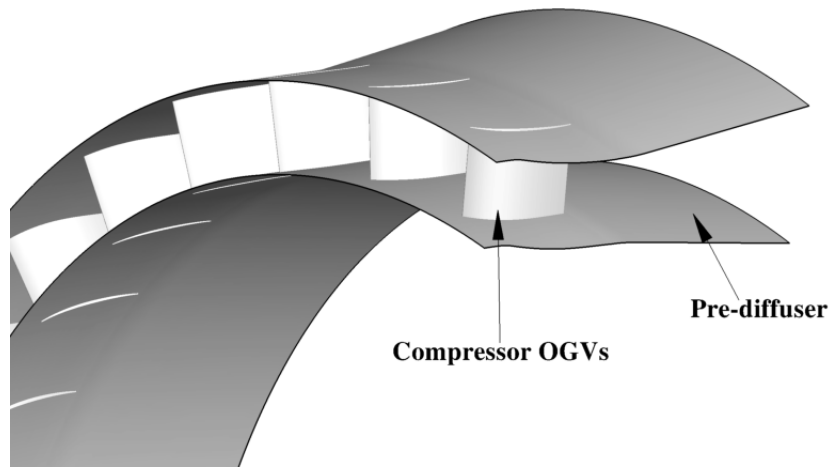
Figure 1.5: Geometry of the OGV/prediffuser assembly

isymmetric annulus inlet conditions. Overall diffuser performance was assessed, in addition to providing some indication of the mean blade wake profiles and their decay within the diffuser. In his summary of the Stevens et al work [33; 34], Klein [3] states that the turbulence associated with the flow field downstream of an axial compressor can exert a <u>beneficial</u> effect on diffuser performance. The onset of separation is delayed thus allowing larger area ratios than those suggested by classical (i.e. simple inlet condition) diffuser performance charts. In a following study, work by Stevens et al. [35] utilised a single-stage compressor whose location, relative to diffuser inlet, could be varied. Thus, the impact on performance of including a short parallel passage between OGV exit and diffuser inlet could be assessed. Such a passage was thought necessary to permit the compressor blade wakes to mix out partially prior to entering the diffuser. The authors observed, however, that the wakes had grown rather than decayed due to upstream pressure gradient effects from the prediffuser and this would clearly lead to an increased overall loss. The above authors all conclude that the condition of the inlet flow greatly effects the performance of the prediffuser. The main conclusion from this work was that for all studies of aeroengine gas turbine prediffuser systems it is important that diffuser inlet conditions are representative of those found in aircraft engines, i.e. containing the effects of residual swirl and outlet guide vane wakes.

The ever increasing demand for engines of shorter length means that within modern engines prediffusers are usually located immediately downstream of the OGV row. This enhances the interaction between the prediffuser and compressor-generated flow fields. More recent experimental work by Zierer[36] has shown how changing the compressor operating point affected the boundary layer flow regions and hence the pressure rise within the diffuser, noting again that, in general, greater pressure rise was in fact achieved with a compressor present for a given diffuser area ratio. Once again the general conclusion supported by this investigation was that, in addition to the mean flow profiles at the prediffuser entrance plane, the enhanced and 3D turbulence field associated with the compressor-generated flow field can improve spanwise mixing and thereby reduce boundary layer growth and the onset of separation.

This realisation has lead to several investigations of the interaction between the wakes shed by an upstream OGV row and a prediffuser flow field. Experimental studies by Barker and Carrotte [4], [37], [38] have quantified the beneficial impact that the blade wakes, the associated higher turbulence levels, and the secondary flow structures typically produced by an upstream axial compressor, can have on the performance of a prediffuser and the quality of the air supply to the fuel injector. Figure 1.6 shows the overall static pressure rise C_p and stagnation pressure loss λ coefficients (see Table 1) (based on five-hole probe area traverses at prediffuser inlet and exit) and the static pressure distribution along the centerline of diffusers with different area ratios and fixed length. The values of the overall static pressure rise are noted in [4] to be significantly greater than those predicted using design charts obtained using conventional axisymmetric inlet conditions. This demonstrates clearly that wake mixing (produced by the OGV blade row) can enhance diffuser performance.

Similarly Walker et al. [39] have shown how, by adopting an integrated approach (as first suggested in [9]), the design of the OGV and prediffuser may be considered simultaneously, with the OGV blade geometry specifically chosen to manipulate the wake flow structure to advantage in achieving improved prediffuser

performance. Finally, work on automatic CFD-based optimisation of aero-engine OGV/prediffuser systems [40], following the suggestions of [39] and [9], has paid specific attention to diffuser inlet conditions, and shown these must be taken into account to gain maximum benefit in reducing total pressure loss in combustor external aerodynamics. The results of the work indicate that the CFD predictions need to be treated with some caution in terms of absolute predictive accuracy, particularly for the OGV loss aspects, but they are good trend predictors.

$\mathcal{R}$	λ	Cp	α_2	α_{2r}	$\triangle Cp$	$\triangle Cp_r$
1.00	0.020	0.130	1.037	1.026	0.030	0.020
1.45	0.045	0.520	1.098	1.062	0.040	0.025
1.60	0.060	0.565	1.134	1.089	0.045	0.030

Table 1   Diffuser overall performance data[a]

(a) Diffuser Overall performance
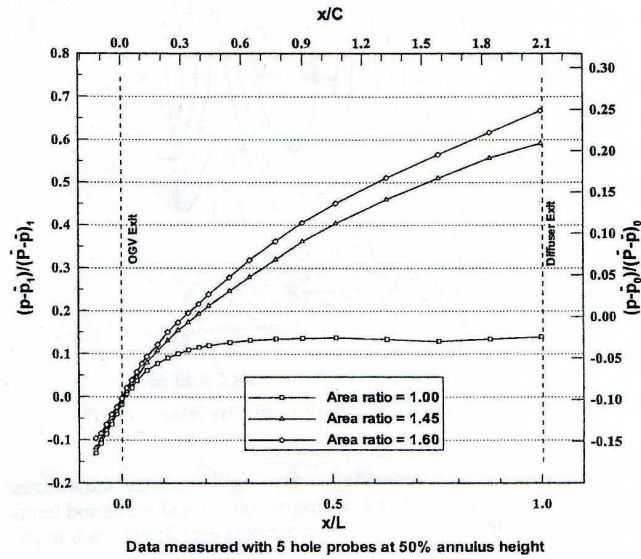
(b) Static pressure distribution along diffuser centerlines

Figure 1.6: Diffuser performance (taken from [4])

The idea of an integrated design/optimisation approach for components in gas-turbine turbomachinery is currently receiving much attention. Shahpar [41], for example, has outlined the development and application of a high fidelity design optimisation framework (called SOPHY) that is used within Rolls-Royce to

provide parametric geometry, automatic meshing, advanced design-space search algorithms, as well as accurate and robust CFD capabilities. He has provided application examples to aero-engine components such as an industrial engine exhaust diffuser and bypass exhaust nozzle optimisation. Schlüter et al. [22] have recently proposed a method for simultaneous solution of a complete compressor/combustor/turbine flow, including both RANS and LES CFD flow solvers. It is, however, currently difficult to imagine such an approach being used for optimisation purposes. The overall compute resource requirement of this method is very large and compute times are extremely long, and optimisation methods typically involve tens or hundreds of CFD solutions. However, the optimisation of strongly coupled components such as compressor OGV and downstream prediffuser certainly merit further study. To this end, Barker et al.[9], as part of the EU project "LOPOCOTEP" (LOw POllutant COmbustor TEchnology Programme) conducted a detailed experimental and computational study comparing the performance of a conventional OGV/prediffuser design (essentially designed on an isolated component basis with the OGV design ignoring the flow field within the prediffuser, and vice versa), with an integrated optimised OGV design (IOGV) obtained from numerical predictions which took account of the strong interaction between the components. This work demonstrated how the OGV geometry could be modified (via vane lean, sweep, etc.) to manipulate the secondary flow emerging from the OGV passage such as to create beneficial effects in the prediffuser flow and allow an increased area ratio (from 1.6 to 1.8 or even 2.0 at fixed length and only slightly increased loss) and thus a gain in overall system performance. The experimental part of this work provided OGV inlet condition data (both mean and turbulence components) and also downstream performance data at OGV exit and prediffuser exit which form excellent validation data for CFD studies.

In CFD-based optimisation, the accuracy of the optimised solution can of course only be as good as the accuracy of the turbulence modelling used. Since the optimum pressure rise design of diffusers is known to be close to incipient separation, and Reynolds-Averaged Navier Stokes (RANS) statistical turbulence models are known to find accurate prediction of strong adverse pressure gradient

induced separation difficult, it would certainly be worthwhile to study and compare the performance of different RANS turbulence model approaches for OGV wake/prediffuser aerodynamic interactions. Equally, it may be that the Large Eddy Simulation (LES) approach may give more accurate predictions. It seems, however, that a comprehensive study of different turbulence model approaches to OGV/prediffuser flows has not been reported to date. This observation has motivated the principle work reported in the thesis. The next step should therefore be to review the various approaches to turbulence modelling, and this is the topic of the next section.

1.3 Review of RANS, LES and Hybrid Methodology for Turbulence Modelling

1.3.1 General

In Computational Fluid Dynamics, turbulence modelling is one of the three key elements alongside grid generation and numerical algorithm (flow-solver) development. Whilst the subject of turbulence modelling for general CFD application has been actively studied for almost 40 years, there is still no generally accepted understanding of precisely what turbulence modelling approach is best for what flow circumstance, due to the extremely complex nature of turbulence.

Most fluid flows occurring in nature as well as in engineering applications are turbulent due to the high values of flow Reynolds number typically found. Even though turbulent flows can be easily observed, it is still difficult to give a simple definition of turbulence. However, researchers and engineers generally agree that 3 important characteristics of turbulence are:

1. Chaotic: The irregular, nearly random and non-linear nature of turbulent flows makes a deterministic description of turbulent motion as a function of time and space extremely challenging and (for high Reynolds number flows) extremely computationally expensive. The strong 3D and non-linearity re-

sults in vortex stretching, a key process by which three-dimensional turbulent flows manipulate their kinetic energy content;

2. Mixing: due to the macroscopic mixing of fluid elements, turbulent flows are characterised by an enhanced rate of mixing of momentum and heat. This is one of the most important properties as far as engineering applications are concerned;

3. Vortical dissipative flow: Turbulence is characterised by high levels of fluctuating vorticity. At high Re turbulence may be easily identified by the existence of a wide range of eddy sizes. The large eddies have length scales of order of the region of turbulent flow. The large eddies contain most of the fluctuating energy. The vortex stretching mechanism transfers energy to increasingly smaller scales, until velocity gradients become so large that kinetic energy is dissipated into internal energy by molecular viscosity[42].

Turbulent fluctuations thus occur over a wide range of length and time scales, leading to broadband spectra. Hinze[43] observed at an early stage in the study of turbulence that turbulence is a multi-scale problem with highly non-linear coupling between these scales [44]. The various modelling strategies that have evolved to capture turbulence in CFD are now briefly reviewed.

1.3.2 RANS and LES Methods

Despite the ever growing capability of modern supercomputers, a direct solution of turbulence by solving the exact (for a Newtonian fluid) time-dependent Navier-Stokes equations for all length and time scales present – called Direct Numerical Simulation (DNS) – is still possible only for rather simple flow cases and at low overall Reynolds numbers. This restriction for DNS becomes obvious when, as Pope [12] shows, the number of grid points needed for adequate spatial resolution scales as $Re^{9/4}$ and the CPU-time as Re^3. DNS is an important tool for understanding turbulent structures and laminar-turbulent transition; DNS can also play an important role in the calibration of turbulence models. However, in engineering applications, the effects of turbulence can be taken into account only

approximately, using models of various levels of complexities [45].

The most commonly used turbulence modelling approach in current practical applications is Reynolds-Averaged Navier-Stokes (RANS). The RANS approach is a statistical approach, in which the instantaneous flow variables are decomposed into a mean and a fluctuating part, Reynolds [46]. RANS models all details of turbulence, as shown in figure 1.7 (In URANS it is assumed that any low frequency unsteadiness which does not interact with turbulence directly has been resolved in the transient term in the equations). A large variety of RANS mod-
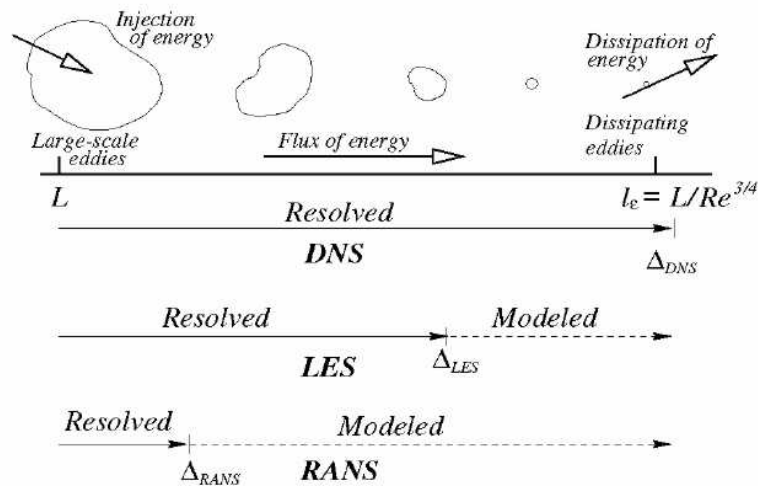
Figure 1.7: Extent of modelling for various types of turbulence model [5]

els has been derived over the years, basically divided into two categories. The first adopts the turbulent viscosity assumption Boussinesq [47], while the second category is referred to as Reynolds-Stress Transport modelling. Mixing length models (Prandtl, [48]), one-equation models (Prandtl, [49]), and two-equation models (Kolmogorov, [50]; Jones and Launder, [51]) belong to the first category. Reynolds stress models (Donaldson and Rosenbaum, [52]; Launder, Reece and Rodi, [53]) and algebraic stress models (Lakshminarayana, [54] Pope [12]) belong to the second category. Most of these models have been described in full by Wilcox [5] and Pope[12], and details of individual model are reviewed in these and other references. Reynolds-Averaged Navier-Stokes (RANS) calculations are able to deliver reliable results for a wide range of flows encountered in applications of

engineering interest, providing results for mean quantities with engineering accuracy at moderate cost. One significant drawback of RANS models is that the constants appearing in the modelled equations have to be calibrated. This calibration was carried out predominantly by tuning the models in flows for which detailed flow and turbulence data were available. Such flows are typically 2D shear flows close to equilibrium. The consequence is that in flows which are very strongly 3D, RANS models sometimes do not perform well. For example, in simulations dominated by large-scale, 3D anisotropic vortical structures (e.g. 3D wakes) time-averaged quantities are predicted less satisfactorily by a RANS model. Similarly, flows with strong transient effects are not well predicted (Unless these have a clear periodic nature, when URANS can provide an adequate extension to steady state RANS). It can be commented right away that the calculation of the mixing out of wakes from an OGV row inside a prediffuser thus probably presents a flow that will be challenging to RANS turbulence models. OGV/prediffuser flow contains most of the "difficult for RANS" turbulence elements: possible laminar/turbulent transition on the OGV aerofoil, strong 3D wake flow, and the possibility of adverse pressure gradient induced separation in the prediffuser.

Thus, for situations where RANS models are not sufficient, the Large Eddy Simulation (LES) approach has become popular in the last 10-15 years. For LES, the dynamics of the large-scale motion is computed directly (see Figure 1.7) and only the small-scale motion is modelled; hence information on large structures can be gained directly from the numerical solution and less strict modelling assumptions need to hold. Furthermore, LES automatically provides unsteady data that are often indispensable: determination of unsteady forces, fluid-structure coupling, identification of aerodynamic sources of sound, to name but a few examples.

However, the Large Eddy Simulation method still involves very fine mesh resolution and long run times, leading to a high computational cost, because of:

1. the requirement to resolve numerically accurately in space and time all the scales of motion which contain a significant fraction ($\approx 80\%$) of the turbulence energy,

2. the observed inability of most simple Sub-Grid Scale(SGS) models to account correctly for anisotropy and strong non-equilibrium effects.

To avoid these two weaknesses leads to the need to adopt very fine mesh resolution, which can be a limiting problem, particularly at high Re. The well-known illustrative example of this problem is the inner region of wall boundary layers, whose intrinsic scale is based on so called "wall units", involving the wall shear stress, which is inevitably a decaying function of Re [6].

For boundary-layer flows, in the near wall region, the Re-dependence of the mesh size needed to achieve a well resolved LES is very strong, since the near-wall energy-containing eddies that need to be resolved scale with wall units and hence decrease in size rapidly as Re increases. As the Reynolds number increases, the dimensions of these eddies decrease more rapidly than the boundary-layer thickness, resulting in yet more stringent grid requirements. According to Chapman[55]'s estimate, the number of points required to resolve the inner layer is

$$(N_x N_y N_z)_{il} \propto Re_L^{1.8} \tag{1.1}$$

Where, Re_L is the Reynolds number based on the integral scale. In the outer layer, the turbulent boundary layer thickness $\delta \propto Re_L^{-0.2}$; Chapman shows that this implies that the number of grid points required to resolve the outer layer is:

$$(N_x N_y N_z)_{ol} \propto Re_L^{0.4} \tag{1.2}$$

The number of time-steps required to perform a simulation is proportional to the number of grid points in one direction [6]. Reynolds[56] estimated that the total cost of a calculation scales like $Re_L^{0.6}$ for the outer layer, but $Re_L^{2.4}$ for the inner layer. Using these estimates for a boundary-layer, Figure 1.8 (taken from [6]) shows that even at moderate Reynolds numbers ($Re_L = O(10^4)$) over 50% of the points are used to resolve the inner layer, which is only 10% of the spatial extent of the flow. This means that for the flow/geometry of current interest (OGV/prediffuser flow) for a $Re_L \cong 1.6 \times 10^5$ (based on the OGV vane chord length and shown as the red lines in Figure 1.8), over 90% of the points and $Re_L^{2.4}$
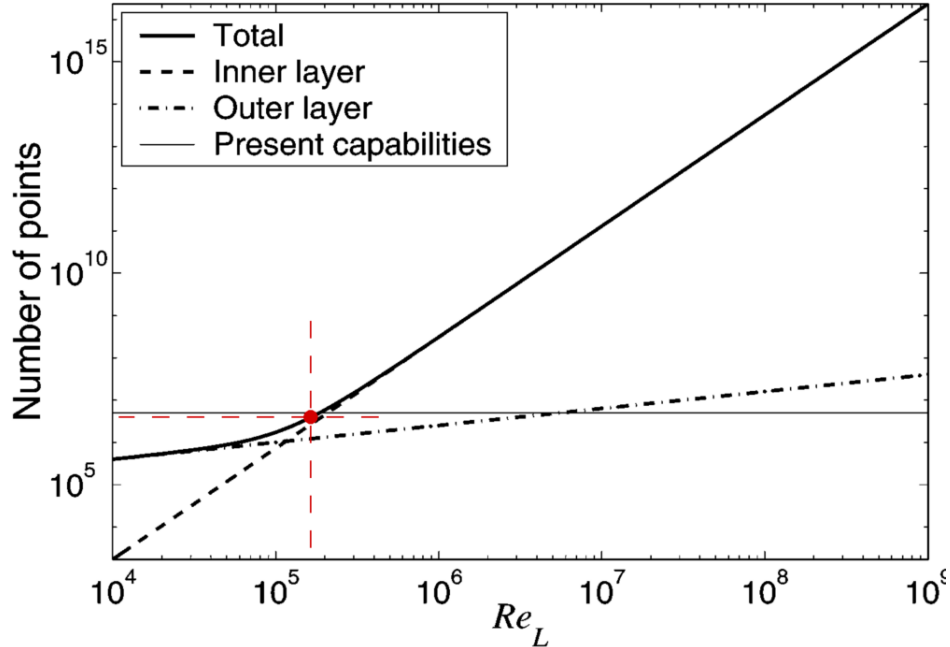
Figure 1.8: Number of grid points required to resolve a boundary layer. The "present capabilities" line represents calculations performed on a Pentium III 933 MHz workstation with 1Gbyte of memory [6]

time-steps will be required if the inner layer is to be well resolved by the LES grid.

As a consequence of this unfavourable scaling, well-resolved near wall LES is still limited to moderate Reynolds numbers. Only if massive computational resources are available (clusters with thousands of processors), are calculations at the high Reynolds numbers of engineering interest ($Re > 10^5$) possible. In fact, compared with RANS computations, the computational cost for LES may be so high that LES is not affordable for a very complex high-Reynolds number flow in any study that requires an extensive parameter investigation.

In order to alleviate this problem, one possible solution suggested recently is to blend Large Eddy Simulation with RANS to provide solutions at much lower cost. Such a hybrid method encourages the use of the more expensive LES only in regions of the flow field where RANS predictions are likely to be inadequate, e.g. in regions where the effects of large coherent structures are of interest [57].

Previous work on the hybrid LES/RANS approach is thus reviewed next.

1.3.3   Hybrid (or Coupled) RANS/LES Methods

Within the class of hybrid RANS/LES methods, two families of approach, as defined by Sagaut et al [44], have evolved in recent years. In one approach, defined as 'Global RANS/LES methods', a single CFD methodology is used throughout the solution domain, which is able to switch "automatically" (i.e. in a user defined manner) between RANS and LES turbulence model in different parts of the solution domain, resulting in a change in terms of local temporal frequency and spatial wave number resolution. In the other approach, defined as 'Zonal RANS/LES methods', a RANS CFD methodology is employed in one (usually pre-defined) part of the computational domain, while an LES CFD methodology is used in the remainder. With zonal methods, the definition of the dependent variables resolved by CFD are clearly no longer continuous at RANS/LES zone interfaces (it is arguable that this also occurs in global methods, since RANS dealts with time-averaged quantities and LES with volume-averaged variables). Instead, RANS and LES computations are essentially performed in their respective subdomains, which are then coupled via appropriate interface treatment, which converts RANS data into LES data (and vice-versa if necessary) [44].

(a) Global RANS/LES Methods

As defined above, non-zonal approaches – currently also referred to as 'universal methods' – are constructed so that they switch automatically from one turbulence modelling method to the other, based on locally determined parameters. The global RANS/LES methods described below may also be interpreted for convenience as a 'blend' between a RANS-type eddy-viscosity model and an LES-type SGS viscosity model.

- **Limited Numerical Scales(LNS) Method**

The Limited Numerical Scales (LNS) method outlined by Batten et al. [58] was inspired by the earlier contribution of Speziale [59], who proposed a hybrid framework in which the Reynolds stress tensor $\overline{u_i' u_j'}^M$ computed from a conventional RANS turbulence model (e.g. a $k - \epsilon$ eddy viscosity model) would be reduced in magnitude before it is used in a set of URANS-based conventional equations via a so-called latency parameter α.

$$\overline{u_i' u_j'} = \alpha \overline{u_i' u_j'}^M \tag{1.3}$$

It was argued that the factor α is used to 'shield' the mean flow predicted from a URANS formulation from the portion of the turbulence which the spatial and temporal discretisation in the CFD code were capable of numerically resolving via the unsteady term in the governing equations (thus avoiding the 'double-accounting' problem). The key ingredient of the LNS approach of Batten et al. [58] was a definition of α based on the ratio of the product of turbulence length and velocity scales defined in two different ways:

$$\alpha = min[(L.V.)_{LES}, (L.V.)_{RANS}]/(L.V.)_{RANS} \tag{1.4}$$

in which $(L.V)_{LES}$ is the product of the turbulence length and velocity scales calculated from a chosen LES SGS model (e.g. a Smagorinsky eddy viscosity model) and $(L.V)_{RANS}$ is the product of turbulence length and velocity scales calculated from a chosen RANS model (e.g. $k^{3/2}/\epsilon$ and $k^{1/2}$). Using this definition of α in conjunction with eq.1.3, the governing equations behave as a URANS set if $\alpha = 1$, or an LES set for $\alpha < 1$. When $\alpha < 1$ (usually in a fine-grid region since L_{LES} is usually proportional to the cube root of cell volume), the scaling of the RANS predicted Reynolds-stress tensor by α causes the local effective viscosity in the discretised convection equations to be reduced to a level implied by the chosen LES SGS model. The energy fraction αk is then interpreted as unresolvable SGS turbulence kinetic energy, which has to be modelled, the remaining $(1 - \alpha)k$ is resolvable turbulence kinetic energy, which is captured directly via transient term on the local mesh (see Figure 1.9).
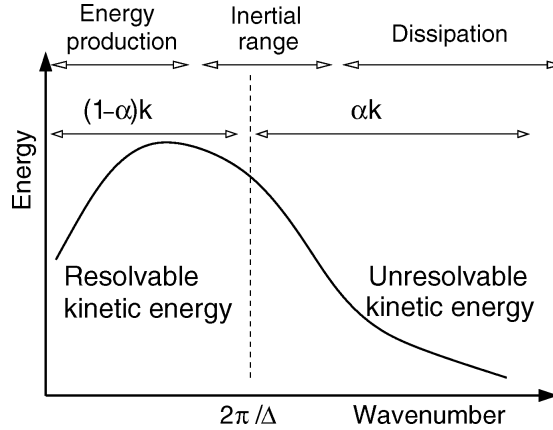
Figure 1.9: Turbulence energy spectrum partitioned into resolvable and unresolvable wavelengths.Taken from Batten et al [7]

The switch between LES and RANS is achieved by an automatic transfer of statistically represented kinetic energy data into directly resolved fluctuations, in a manner consistent with the length and timescales of the statistical turbulence, the second moments, and the resolvable fraction of the turbulence energy. Batten et al. [7] have implemented their hybrid method for arbitrary meshes, which can include embedded fine-grid regions. Preliminary applications (such as to two-dimensional square cylinder wake, hill flow and fully developed channel flow) showed improvement compared with conventional RANS and URANS predictions. However, it should be acknowledged that these test cases were relatively simple with rather modest Reynolds numbers ($\approx 10^3$ or 10^4).

- **Blending Methods**

Schumann [60] in 1975 proposed the idea of using RANS as a near-wall model embedded within or blended with an LES simulation. This concept of a blending method has more recently been extended by Baggett [61], who expressed the unclosed stress terms in the governing equations (either RANS or LES) as a function of <u>both</u> an LES SGS viscosity ν_t^{LES} and a RANS eddy viscosity ν_t^{RANS}:

$$\tau_{ij} - \frac{1}{3}\tau_{kk}\delta_{ij} = -[(1 - \Gamma(y))\nu_t^{LES} + \Gamma(y)\nu_t^{RANS})]\overline{S}_{ij} \qquad (1.5)$$

Where $\Gamma(y)$ (y here represents distance from a wall) is a blending function between RANS and LES turbulence models for the unclosed stress. When the blending function equals unity, the model acts in RANS mode whereas LES modelling is recovered when $\Gamma(y)$ is zero. Although $\Gamma(y)$ depends on the distance to the wall y, Bagget indicated that the blending function should perhaps better be viewed as a function of the ratio Δ/L_ϵ, where L_ϵ is an estimate of the local turbulent length scale and Δ is a measure of the LES spatial filter width (i.e. proportionate to locale grid size).

Further development of this blending function approach has been made by Fan et al. [62], [63]. Following the ideas of Menter [64], Fan et al. suggested using a blending function to shift a RANS model used in a region near a solid wall to a subgrid LES model further away by adopting equations for the turbulence energy and the turbulent viscosity which were a blend of RANS and LES versions of these equations:

$$\begin{aligned}[\texttt{hybrid RANS/LES k equation}] = {} & \Gamma \cdot [\texttt{RANS k equation}] \\ & + (1-\Gamma)[\texttt{LES k equation}]\end{aligned} \tag{1.6}$$

$$\begin{aligned}[\texttt{RANS/LES hybrid turbulent viscosity}] = {} & \Gamma \cdot [\texttt{RANS eddy viscosity}] \\ & + (1-\Gamma)[\texttt{LES SGS viscosity}]\end{aligned} \tag{1.7}$$

Where Γ is a user specified [63] flow-dependent blending function designed to yield a value of 1 within the attached boundary layer and to transition rapidly to zero further away from the wall.

It is implied in equation 1.7 that any RANS model can be blended with any LES SGS model. Xiao et al.[65] implemented the RANS $k - \zeta$ model with an LES one equation (k^{sgs}) SGS model to simulate the flow over a compression ramp. Fan et al.[66] combined a RANS-SST $k - \omega$ model and a one-equation LES SGS model for k^{sgs} to conduct a simulation of shock wave/boundary layer interaction in a

Mach number 3 flow over a 20 degree compression corner. In general, the performance of these models is encouraging. Nevertheless, all authors comment that a significant amount of work has still to be conducted to evaluate and quantify the effect of the precise form of the blending function and the selected turbulence models. In principle, there is no reason why only models containing equations for k and k^{sgs} must be used to construct hybrid blended models. The hybrid blended approach can be presented in a general form independent of the types of RANS and LES models employed.

- **Detached Eddy Simulation Method**

Detached Eddy Simulation(DES), perhaps the oldest global method and certainly the most used approach, is still under development and being applied to an increasing variety of flows (Spalart [67]). The DES idea was first proposed in Spalart et al. [68] (referred to below as DES97) by modifying the Spalart-Allmaras [69; 70] model, which solves a transport equation for a RANS eddy viscosity (v_t), into an LES SGS model; the RANS equation for v_t is:

$$\frac{D\nu_t}{Dt} = c_1 S \nu_t - c_2 f_w (\frac{\nu_t}{L_{DES}})^2 + diffusion \tag{1.8}$$

As explained in [71], the DES version of this model is obtained by an appropriate modification of the length scale L. L can be extracted from any RANS model (L_{RANS}) and also from any LES SGS model, which relates length scale to local mesh size. The DES length scale L_{DES} is thus defined as:

$$L_{DES} = min\left(L_{RANS}, C_{DES}\Delta\right) \tag{1.9}$$

where C_{DES} is a modelling parameter to be determined and the LES filter width Δ was based on the largest local cell dimension:

$$\Delta = max(\Delta_x, \Delta_y, \Delta_z) \tag{1.10}$$

DES as originally proposed was designed to treat attached boundary layer regions using a RANS model and to apply LES only in separated flow regions. The

simulation switched between RANS and LES by comparing the distance from the wall d (assumed to be a good estimate of the RANS length scale) with $C_{DES}\Delta$ in eq.1.9. Close to the wall ($d < C_{DES}\Delta$) RANS is employed, away from the wall ($d > C_{DES}\Delta$) the model turns into an LES SGS model. The transition in ν_t is continuous and smooth since the switch is only evident in the source term in eq.1.8

DES has been successfully applied to a range of problems spanning complex engineering applications to simple flow studies[67]. One potential disadvantage of this approach is that the transition between LES and RANS depends entirely on geometry (wall distance) and grid spacing and thus may not correlate well with the physics of boundary-layer development. The RANS/LES transition may occur deep within the boundary layer or well outside depending on the grid, which has to be chosen before the flow solution is available. Most calculations with the DES method have used grids which guaranteed that wall boundary layers were entirely contained within the RANS region. Thus, the technique is most appropriate for flows that exhibit a clear delineation between attached boundary layers at surfaces (treated as RANS) and free-shear layers or regions of massive flow separation (treated as LES).

A correction for this inherent flaw of DES has been recently proposed in a new version of this model – referred to as DDES for Delayed DES (Spalart et al. [72]). In DDES, the length scale depends not only on the grid but also on parameters derived from the flow. Although tested on boundary layers, single and multi-element airfoils, a cylinder flow, and a backward-facing step flow have demonstrated that the DDES concept is generally viable, this still remains to be fully explored, since all the above studies correspond to attached/separated boundary layer flows.

Calculations from a number of research groups, Refs. [68] [71] [7] and [73], have shown that global methods can produce good results for massively separated boundary layer flows. In these flows unsteadiness is strongly self-sustaining but the unsteady effects can be considered not to feed back strongly into the separating boundary layer. Existing global models have, however, not been shown to be well suited to impinging flows, thin separation regions, or strongly 3D wake

flows, which are all important elements of the OGV/prediffuser problem. The global RANS/LES strategies mentioned above rely on a single set of equations that are "adjusted" by the algorithm into RANS or LES models. In the transition zone, between RANS and LES zones, it is not clear how quickly the unsteady turbulent eddies develop. This concern is of particular relevance to the prediction of flow fields dominated by free shear layers (e.g. wakes) since any delay in the appearance and growth of resolved eddy structure will adversely affect the ability to capture mixing processing. Further, global hybrid RANS/LES methods are based on a continuous treatment of the flow variables (the velocity field) at the RANS/LES interface. This introduces a 'grey area', since the switch from RANS to LES variables is effected instantaneously, with no attempt to recognise that RANS variables (even URANS) are averaged over time, whereas LES variables are averaged over space. Global methods are therefore labelled by Sagaut et al.[44] as 'weak RANS/LES coupling methods', since there is no rational, explicitly identified mechanism included to transfer the modelled turbulence energy in the RANS zone into resolved fluctuating turbulence energy in the LES zone. Thus, global methods may not be adequate in situations where upstream turbulence plays a significant role in the downstream flow development (as in OGV/prediffuser flow). For the above reasons, it is considered that the global approach may not be ideally suited for application to OGV/prediffuser flow.

(b) Zonal RANS/LES Methods

In zonal methods, the use of pre-defined 'pure' RANS and 'pure' LES zones avoids the 'grey area' problem. Zonal hybrid RANS/LES methods are based on a discontinuous change in the solution methodology across any RANS/LES interface. The main difficulty which therefore has to be addressed is that information must be exchanged at any RANS/LES domain interface between two solution algorithms with very different spectral content. This highlights that in zonal methods the quality of the results is strongly influenced by the treatment at RANS/LES interfaces. Another benefit of the zonal modelling approach is that all the turbulence models suited best for a given flow type or complexity can be chosen for each of the sub-domains without fear of inconsistencies in their use. The price to pay is

the construction of appropriate coupling conditions at interfaces. Coupling can occur in several different ways, as illustrated in Figure 1.10 [8], where a local LES zone is surrounded by RANS zones. The types of interface shown are: (1) Upstream RANS domain to downstream LES domain, (2) Upstream LES domain to downstream RANS domain, (3) near wall RANS domain to an outer flow LES domain, and (4) outer flow LES domain to an external RANS domain.
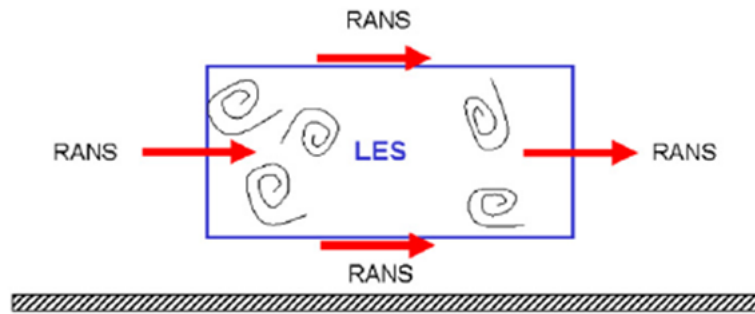
Figure 1.10: Possible types of interfaces with zonal modelling (from [8])

The most challenging interface treatment is the first one. This is also the one of most relevance to the OGV/prediffuser application, as illustrated in the practice adopted by Schlüter et al. [22] where the upstream turbomachinery component (OGV) was modelled via RANS and the downstream component (prediffuser) via LES. Hence this is the interface considered in detail here and relevant prior work is discussed below. Literature references relevant to other interface treatments in hybrid zonal methods could be found in: (2) [24], [57], [74], (3) [8], [44] [75] (4) [8], [44], [76].

LES Inflow Conditions at a RANS/LES Interface

In all cases with an LES zone downstream of a RANS zone, the LES inlet plane requires as realistic as possible specification of a correlated, turbulent fluctuating velocity field at the interface in order to avoid any artificial (i.e. unphysical) transition zone within the first part of the LES subdomain. Hence, using the RANS

predicted mean flow field merely complemented by addition of white noise fluc-
tuations to generate unsteady inflow data for the LES domain will definitely not
be sufficient. Additional treatment of the RANS solution, which includes further
assumptions on local eddy length scales (correlation lengths), time scales and en-
ergy distribution is required to create an accurate inlet condition for LES. In this
context, RANS/LES coupling has many similarities with the well-known prob-
lem seen in 'pure' LES predictions of providing physically accurate, time-resolved
and correlated inlet conditions. This topic has received considerable attention in
recent years and since this work is directly related to the present coupling issue,
it is reviewed below.

Several approaches have been proposed for LES inflow boundary condition gen-
eration: (i) addition of random fluctuations (e.g. white noise), (ii) use of in-
stantaneous velocity fields saved from a precursor LES simulation, (iii) various
approaches based on what is referred to here as synthetic turbulence generation.
The first is the simplest but is not a serious candidate, since the random nature
of white noise means this decays rapidly and a long transitional zone/length is
needed to generate realistic correlations. Work on the other two approaches is
thus discussed next.

- **Precursor Simulation Approach**

The precursor method as used to generate LES inflow conditions requires a sep-
arate (precursor) calculation of a flow which corresponds as closely as possible
to the geometry and conditions in the region immediately upstream of the LES
inlet plane, to generate a 'database' of unsteady velocity data which is then in-
troduced into the LES computation. The most obvious example of this method
is the case where the flow conditions upstream of the LES inlet plane can be
assumed to correspond to a fully-developed flow in a duct whose cross-section
is fixed by the shape of the (2D) LES inlet plane. In this case a separate LES
calculation can be made using periodic boundary conditions between inflow and
outflow planes of a duct segment sufficiently long that the large scale turbulent
eddies are not constrained by the periodic boundaries. If the LES inflow is not
fully developed but has a known boundary layer thickness on the duct walls,

then the precursor calculation is carried out in a long length of duct and, once the precursor LES solution has become statistically stationary, the axial location in the precursor simulation which matches the known boundary layer thickness can be found and unsteady time-history data extracted from this location for a sufficiently long time period that the first and last time 'slices' are statistically independent of each other. The unsteady time history of the velocity field in the selected plane normal to the streamwise direction is then stored for a series of time steps long enough for the last data to be uncorrelated with the first. This time-history sequence of unsteady data is then read in as inflow conditions for the main LES calculation of the flow of interest. Note that for convenience the interface cross-section spatial grid and time-step in the precursor simulation are the same as in the main LES calculation. Akselvoll and Moin [77] used this method to generate inflow boundary conditions for an LES of a coaxial jet fuel cylindrical combustor, using 2D velocity fields extracted from a separate LES calculation of a coaxial annular pipe flow with periodic boundary conditions in the streamwise direction. Similarly, Kaltenbach [78] used a periodic simulation of a channel flow to generate inflow conditions for LES of a plane asymmetric diffuser.

More recent simulations of spatially developing turbulent duct flows have suggested modifications to manipulate precursor data. One modification has been proposed by Schlüter et al. ([2; 22; 24]) for use in hybrid RANS/LES computations where an LES domain is located downstream of a RANS domain. The particular target application involved RANS calculations in a multi-stage compressor followed by LES calculations in a diffuser. They used a precursor database, created from an auxiliary LES computation of a fully-developed turbulent pipe flow at a suitable Reynolds number, to provide LES inlet flow turbulent fluctuations for use at the RANS/LES interface. However, since the flow at the exit of the RANS compressor calculation did not possess the same mean velocity profile, or turbulence intensity profile as in the precursor pipe flow LES database, rescaling was needed. This made use of a RANS solution obtained in the annular duct at compressor exit and just upstream of the diffuser LES inlet plane. The LES inflow boundary condition at any point in its inlet plane was then prescribed as:

$$u_{i,LES}(t) = \underbrace{\overline{u}_{i,RANS}}_{I} + \underbrace{(u_{i,DB}(t) - \overline{u}_{i,DB})}_{II} \cdot \underbrace{\frac{\sqrt{\overline{u'^2_{i,RANS}}}}{\sqrt{\overline{u'^2_{i,DB}}}}}_{III} \qquad (1.11)$$

where the subscript RANS denotes the solution obtained from the RANS compu-
tation, and quantities with subscript DB are provided from the database. Here,
t is time, u_i stands for the Cartesian velocity component in direction i, and an
overbar indicates a long time average.

It was not made clear in Refs ([2; 22; 24]) how the velocity field from the pipe flow
database was scaled to suit the mean velocity provided by the RANS calculation.
Nevertheless, the authors claimed that scaling the velocity fluctuations extracted
from (some points in) the database (Term II), when scaled by term III, produced a
qualitatively correct level of velocity fluctuations. It is plausible that this process
would work where the LES inlet flow was close to a pipeflow configuration, but not
at all clear how this would function in any other circumstance. Further, since the
RANS flow solver used a two-equation turbulence model which cannot accurately
provide the individual Reynolds normal stresses, these were approximated by:

$$\overline{u'^2_{(i)RANS}} = \frac{2}{3}k \ with \ i = 1, 2, 3 \qquad (1.12)$$

with (i) denoting that no summation of components is made.

Simulations of (axisymmetric) confined swirling and non-swirling jets using this
method yielded results in good agreement with experiments. Schlüter et al. [2]
also applied their method as part of a very large computation of an entire gas
turbine. This is a much larger (but much less convincing as noted above) appli-
cation of the precursor approach. For example, since the RANS/LES interface
was between compressor and combustor prediffuser, this is an annular duct flow
with developing blade wakes. It is by no means clear why the turbulence struc-
ture saved from a fully-developed turbulent pipe flow should be applicable in this
case, even when scaled according to eq. 1.12. Further, scaling locally only on
the turbulence intensity does not take any recognition of the different turbulent

length scales between a pipeflow and a 3D wake flow with endwall boundary layers. For these reasons, the precursor approach does not seem the most promising avenue for developing a RANS/LES interface technique.

- **Synthetic Turbulence Generation**

(i) Controlled Forcing

Spille-Kohoff and Kaltenbach [79] have proposed an inflow generation method based on the introduction of a forcing term into the LES equations. In this method, random turbulence generation is applied at the inlet plane but a number of "control" planes are then used to manipulate the stress distribution for a short distance downstream of the inlet. At each of these planes, body force terms are introduced that amplify the wall-normal velocity fluctuations to match a "target" Reynolds shear stress provided by experiments or from a RANS model. Keating et al. [80] successfully applied controlled forcing to the task of generating synthetic turbulence inflow profiles for a developing channel flow. The same authors [81] also used the method in a hybrid RANS/LES simulation with the RANS statistical results (mean velocity profile and Reynolds shear stress) used to supply the 'target' information required. Various flows were examined such as a zero-pressure-gradient boundary layer and flat-plate boundary layers in strong favourable and adverse pressure-gradients (including separation). The hybrid calculations were compared to well-resolved LES solutions of the entire domain. Introducing controlled forcing was found to give good results, although a considerable development length was still necessary before physically self-sustaining turbulence was established. The length of this was shortened compared to no forcing, but the correct friction coefficient and turbulent kinetic energy values still took an appreciable length to stabilise to correct levels, so the method does not perform adequately at least in this sense.

The use of forcing terms to generate synthetic turbulence for swirling turbulent inflow conditions has been investigated by Pierce and Moin [82]. Swirling flows occur extensively in gas turbine applications, in particular for flame stabilisation in the combustor, so LES of swirling flow is of significant interest. Pierce and

Moin [82] presented a methodology for generating swirl by introducing a constant tangential body force into the LES momentum equations. Various radial profile shapes of the forcing term were explored for both circular and annular ducts, Simulations in an axially spatially periodic domain were shown to correctly generate fully developed swirling flow.

Pierce [83] extended the 'forcing' technique to the controlled generation of turbulent inflow conditions having specified mean statistical properties for all velocity components, not just swirl. This was achieved by simulating a spatially periodic, parallel duct flow but constraining it by using "forcing" in all LES momentum equations (by repeated re-scaling of the LES solutions), so that the resulting flow has a desired set of statistical properties, but still provided realistic turbulent fluctuations that are in "equilibrium" with the specified mean statistics.

The forcing technique was implemented as follows: at each time step, the streamwise (x)-time-averaged velocity, $\overline{u}(y, z, t)$, and variance, $\overline{u'^2}(y, z, t)$, are computed from the 'forced' LES solution by spatially averaging over grid cells in the x-direction (indicated by $<>_x$):

$$\overline{u}(y, z, t) = \langle u(x, y, z, t)\rangle_x, \quad \overline{u'^2}(y, z, t) = \langle u(x, y, z, t)^2\rangle_x - \overline{u}(y, z, t)^2 \quad (1.13)$$

Then, the instantaneous velocity field is rescaled and shifted so that it has specified mean and fluctuating velocity profiles:

$$u(x, y, z, t) = \overline{u}_{target}(y, z) + \frac{u'_{target}(y, z)}{\sqrt{\overline{u'^2}(y, z, t)}}[u(x, y, z, t) - \overline{u}(y, z, t)] \quad (1.14)$$

Where x is the streamwise coordinate direction, y and z are cross-stream directions, $u(x, y, z, t)$ is the instantaneous streamwise velocity component, $\overline{u}_{target}(y, z)$ and $u'_{target}(y, z)$ are the desired mean and fluctuation intensity profiles. This expression is similar to eq.1.11, the difference is in eq.1.11 the turbulent fluctuation is scaled from a separate data base, but in eq.1.14 it is scaled from a relevant LES simulation. It was argued that this practice is equivalent to adding an appropriately defined body force to the u-component momentum equation.

(ii) Digital Filtering

A general and simple approach to generate synthetic turbulent inflow conditions is to superimpose manipulated unsteady fluctuations (based on user-supplied additional information) onto the mean velocity (provided by RANS or experiments). These methods are based on the assumption that sufficient information on turbulence characteristics can be specified by using only low oder statistics (e.g. mean velocity, 2nd moments) or spectral information.

Batten et al. [84] proposed to generate synthetic turbulence based on selected Fourier modes. Similarly Druault et al. [85] applied POD (Principal Orthogonal Decomposition) information to generate inlet conditions for both DNS and LES from experimental data acquired using hot wire measurements. The most popular method of this type, however, is the so called "digital filtering" approach. Veloudis et al. [86] followed the original suggestion of Klein et al. [87] to construct inflow data using digital filtering and showed how the time taken to generate the filter coefficient could be reduced. However, digital filtering methods are still observed to suffer from some decay of structures imposed at the LES inflow plane and hence still require a transitional zone at the start of the LES zone (although much reduced compared to white noise). This transitional region is inevitable because digital filtering methods do not allow natural, consistent development of spatial/temporal correlations, since they usually assume a (normally Gaussian) correlation shape as part of the method used to find the digital filtering coefficients. Hence a region will always exist (when using digital filtering) beyond the inlet plane where the unsteady field adjusts to develop 2-point spatial correlations that are consistent with the mean and 2nd moment statistics imposed.

(iii)Recycling-Rescaling

The recycling-rescaling method avoids the need to pre-specify any spatial/temporal correlations, and allows these to develop naturally. The approach is a derivation of a method developed by Spalart [88; 89] for a flat plate boundary layer using a variant of the controlled forcing approach. This was further developed by Lund et al. [90]. As applied to a boundary layer flow, the method consisted of taking a

plane of data from an LES calculation of the boundary layer at a location several boundary-layer thicknesses (δ) downstream of the inflow plane, rescaling the inner and outer layers of the extracted data separately (to account for the different similarity laws that are observed in these regions) in order to achieve a boundary layer with a user-presented thickness and reintroduce the rescaled velocity field at the LES inlet plane.

Compared to the forcing approach, the essential advantage of the recycling/rescaling method of Lund et al. [90] (here after referred to as R^{2}M) is that it allows better control of the desired turbulent boundary layer properties (e.g. displacement and momentum thickness) at the required LES inlet plane, and reduces the subsequent transition region to a consistent self-sustaining LES resolved boundary layer compared with other approaches. Stolz and Adams [91] have proposed a version of the method for compressible flow. The recycling and rescaling approach has been successfully used in both Direct and Large Eddy Simulation CFD but not yet in hybrid RANS/LES.

The most thorough study of variants of R^{2}M has been published by Baba-Ahmadi and Tabor [92]. Four different variants were discussed and compared:

1. Method A represents the most basic recycling methodology with only a simple feedback method providing control over a minimum number of flow parameters (basically just the inlet mass flux).

2. Method B introduced a constant axial body force to aid convergence towards the desired mass flow rate.

3. Method C introduced a mean velocity correction (rescaling) algorithm which updates the velocity field within the recycling section based on the error between the sampled profile and a desired mean flow profile. This enables control of a desired mean velocity profile.

4. Method D combined elements of both controlled forcing and velocity correction (re-scaling) to generate both a desired mean velocity profile and a desired turbulence profile.

All four methods were applied to plane channel flow and pipe flow.(NB these are not demanding test cases)

Results showed that methods B-D, all produced good results for the parameters controlled; mean and turbulent statistics were well reproduced, and the turbulent energy spectrum was unaffected by the methodology used. Furthermore, there was no evidence of significant change in flow properties between the recycling section and the main part of the flow domain, or across the recycling surface, despite any manipulations being applied to the LES equations being solved within the recycling domain (e.g. forcing source term). However, it was noticed that Method C seemed to enhance the fidelity of turbulence achieved in the main flow domain more than the other methods (reduced transitional effects), due to the explicit velocity correction used.

A recent study of the R^2M approach by Xiao el al [93] (a method D style) has clearly demonstrated the ability of R^2M to generate an unsteady turbulence field within the recycling section, which is a distinct improvement over the Digital Filtering approach. When applied to a boundary layer, the 2-point spatial correlations that were developed within the recycling domain produced integral length scales that agreed very well with measured values using multiple hot-wires in a fully turbulent boundary layer. This "internal consistency" between the "forced" target mean velocity and turbulent statistics and spatial turbulence correlations is an important element in eliminating any physically spurious transition region in the early part of the overall LES domain.

The R^2M approach certainly seems the most plausible for generating LES inlet conditions where appropriate experimental data is available (e.g. mean and turbulent statistics). The methodology could therefore be eminently suitable to a Hybrid RANS/LES approach where the time-averaged flow statistics delivered by the RANS flow solver are used to guide the inflow conditions for the LES flow solver. However, this does not seem to have been explored to date, and will therefore form an important element of the research reported here.

1.4 Thesis Aims and Objectives

Section 1.2.3, has reviewed previous work (both experimental and computational) on the interaction between the wakes shed by upstream OGVs and a downstream prediffuser flow field. Whilst useful specific experimental data are available for testing CFD predictions in this flow application (e.g. the LOPOCOTEP investigation [9]), only $k - \epsilon$ high-Re eddy viscosity calculations are currently available[9]. This restricted view of turbulence model performance in CFD analysis of OGV/prediffuser flow makes it difficult to decide the best turbulence approach to be used. It would therefore be valuable to have comparisons between various turbulence modelling approaches for the OGV/prediffuser flow problem. High-Re and low-Re RANS statistical models, LES, and also hybrid RANS/LES solutions as reviewed in section 1.3 are needed, in order to understand the optimum approach for modelling turbulence effects in this practically important sub-component of compressor/combustor interaction. To deliver and analyse such a turbulence modelling approach comparison, validated against the benchmark experimental data available, is the prime objective of the work reported in this thesis. As the review in section 1.3 has shown, for application of the hybrid RANS/LES approach, a significant element of the work will have to focus on an improved method of constructing an unsteady, physically correctly correlated turbulent velocity field for inlet conditions to the LES domain (for the prediffuser) from the available RANS solutions (for the OGV flow). The main steps required are therefore as follows:

- Carry out and analyse numerical predictions of OGV/prediffuser flows, using a "pure" RANS approach — both high Reynolds [94] and Launder-Sharma low Reynolds $k - \epsilon$ models [95] should be investigated, using the test geometry and experimentally determined inlet conditions from [9].

- Develop further the Recycling and Rescaling Method (R^{2}M) reported in [93] for generation of LES inflow conditions from pre-specified RANS turbulence statistics, so that it is applicable to a compressor rotor exit/OGV inlet plane.

- Carry out and analyse numerical predictions of OGV/prediffuser flows, us-

ing a "pure" LES approach, testing sensitivety to various modes of inlet condition specification including R²M.

- Carry out and analyse numerical predictions of OGV/prediffuser flow using a Hybrid RANS/LES approach, with the interface located at OGV exit, and explore use of R²M as a RANS/LES interface technique.

- Validate predictions via detailed comparison with the LOPOCOTEP [9] experimental data for: (a) a datum (conventional) OGV design, (b) an advanced (integrated) OGV design incorporating vane sweep and trailing edge recamber.

- Provide recommendations for the optimum turbulence modelling approach for OGV/prediffuser prediction and suggest useful future work.

1.5   Structure of Thesis

The following chapters of the thesis describe the research carried out to achieve the aims of this study and meet the objectives set above.

In the second Chapter, a description of the Loughborough University in-house CFD code DELTA (which has been used throughout this project) is provided. This will cover the mathematical basis of the flow solutions presented in the present study, namely the High-Re and Low-Re turbulence $k - \epsilon$ models for RANS flow solvers, and the Smagorinsky SGS model for the LES flow solver. Sufficient details are also provided of the numerical algorithm used to solve the equations governing the flow. An outline of the chosen experimental test case geometry and associated mesh generation practices is also given. Chapter 3 presents the implementation of an unsteady LES inlet condition generation method developed following the Lund et al. R²M concept reported in [90] and recent work reported in [93]. A comparative study of numerical predictions of the OGV/prediffuser flow using both "pure" RANS and "pure" LES approaches is then presented. Chapter 4 describes in detail the development and implementation of the methodology required for the application of a Hybrid RANS/LES

approach to the OGV/prediffuser configuration. Chapter 5 then presents results allowing assessment of the performance of the Hybrid RANS/LES approach as applied to both a datum OGV design and an advanced integrated OGV design, and the validation of the Hybrid RANS/LES predictions against experimental data. Finally, the conclusions drawn from the present work as well as suggestions for future studies are given in Chapter 6.

Chapter 2

Numerical Methodology

2.1 Introduction

In order to achieve the aims and objectives described above, a computational fluid dynamics (CFD) code had to be chosen. For the current study, the in-house code, DELTA, was selected. DELTA has been under development in the Department of Aero and Auto Engineering at Loughborough University since 1994 [96]. DELTA is based on a finite-volume, structured grid, pressure-based approach for the solution of the governing equations. It uses a collocated variables arrangement based on a multiblock structured curvilinear grid, solving for Cartesian velocity components, in combination with Rhie-Chow smoothing [97] to avoid pressure-velocity decoupling. DELTA adopts a version of the SIMPLE pressure correction method, modified to handle both incompressible and compressible flow.

In its original form, DELTA was an inviscid Euler code but a version was later developed to allow solution of compressible and incompressible laminar and turbulent flows, using a two-equation high Re k-ϵ turbulence model in conjunction with wall functions. It has been extended further to include an LES capability. DELTA has been employed in the past for the calculation of a wide range of flows: compressible [98], incompressible [99], external [100], internal [99], free [101] or wall-bounded [99]. In all cases it has performed well and it was therefore considered a flexible and optimum choice for the current project.

2.2 Flow Solvers

The in-house code, DELTA, provides users with alternative flow solvers, allowing both RANS and LES solutions. The RANS version has been applied to various aerospace applications such as Hot Gas Ingestion (Page et al. [100]) and propulsion installation applications ([102]); the LES version has been used for jet noise reduction [101], high-frequency noise prediction improvement [103], and also in a study of LES inlet condition generation [86].

In the current project, both of these flow solvers have been applied to investigate the OGV/prediffuser flowfield. This particular flow problem has a low-Mach-number (Mach No. ≈ 0.13 at OGV inlet and ≈ 0.08 at diffuser exit in the LOPOCOTEP experiment [9]) and no chemical reaction, thus density, temperature or energy variations play a minor role. The fluid density can be assumed constant over the flow region to a good approximation. The effects of compressibility on the performance of the OGV/prediffuser flow is very small. Therefore, in all the CFD predictions presented in this thesis, the flow is assumed to be incompressible and the pressure-correction scheme used in DELTA is selected accordingly. A description of the flow solvers used is presented in the following sections.

2.2.1 RANS Flow Solver

The RANS flow solver of DELTA was initially written to simulate turbulent flows using a high Reynolds number, two-equation k-ϵ turbulence model together with wall functions. In order to capture viscous-dominated near wall behaviour the Launder-Sharma [95] low Reynolds number model was introduced later by Trumper [104]. The incompressible RANS version solves constant density time-averaged conservation equations for mass and momentum. The Reynolds-Averaged Navier-Stokes equations can therefore be written as (density is retained in the equation formulation for convenience):

$$\frac{\partial(\rho\overline{u_i})}{\partial x_i} = 0 \tag{2.1}$$

$$\frac{\partial(\rho\overline{u}_i\overline{u}_j)}{\partial x_j} = -\frac{\partial\overline{P}}{\partial x_i} + \frac{\partial(\overline{\tau_{ij}} - \rho\overline{u_i'u_j'})}{\partial x_j} \tag{2.2}$$

where

$$\overline{\tau_{ij}} = \mu_L\left(\frac{\partial\overline{u_i}}{\partial x_j} + \frac{\partial\overline{u_j}}{\partial x_i}\right) \tag{2.3}$$

Note that statistically stationary mean flow has been assumed as well as constant density ρ so that eq. 2.1 and 2.2 contain no time dependent terms. Here an overbar indicates a long time-averaged (mean flow) quantity and the fluctuation about the mean is represented by a dashed quantity, μ_L is the molecular (laminar) fluid viscosity (assumed constant) and a Newtonian viscous stress/strain rate constitutive equation has been adopted.

The application of time-averaging to the exact Navier-Stokes equations has resulted in the appearance of additional unknown correlation terms, the turbulent Reynolds stresses $\rho\overline{u_i'u_j'}$. In order to arrive at a closed set of equations, modelling of the Reynolds stresses is required. According to Boussinesq's Hypothesis [47], which assumes that the turbulent stresses are related linearly to the mean strain rate of a fluid element as in a laminar flow (the Eddy Viscosity Hypothesis), the Reynolds stress can be represented as:

$$-\rho\overline{u_i'u_j'} = 2\mu_t\overline{S_{ij}} - \frac{2}{3}\rho k\delta_{ij} \tag{2.4}$$

where $\overline{S_{ij}} = 1/2\left[\partial\overline{u}_i/\partial x_j + \partial\overline{u}_j/\partial x_i\right]$ denotes the mean strain-rate tensor, k is the turbulent kinetic energy $\frac{1}{2}\overline{u_i'u_i'}$ and μ_t stands for the turbulent or eddy viscosity.

Turbulence models based on the eddy viscosity approach can be written at varying levels of complexity. The $k - \epsilon$ turbulence model is the most widely employed two-equation eddy-viscosity turbulence model [45]. It is based on the solution of modelled equations for the turbulent kinetic energy and the turbulent dissipation rate. In the current work both the standard high Reynolds number $k - \epsilon$ two-equation turbulence model and the Launder-Sharma low Reynolds number version have been applied, and these are addressed next.

2.2.1.1 High Reynolds Number $k - \epsilon$ Turbulence Model

The high Reynolds number turbulence model employed in this thesis is the standard $k - \epsilon$ model as reported by Launder and Spalding [94]. The eddy viscosity is written as:

$$\mu_t = c_\mu \rho \frac{k^2}{\epsilon} \tag{2.5}$$

Two additional modelled transport equations are thus required to be solved in order to determine the μ_t distribution throughout the flowfield:

$$\frac{\partial(\rho \overline{u_j} k)}{\partial x_j} = \frac{\partial}{\partial x_j}\left[\left(\mu_L + \frac{\mu_t}{\sigma_k}\right)\frac{\partial k}{\partial x_j}\right] + P_k - \rho \epsilon \tag{2.6}$$

$$\frac{\partial(\rho \overline{u_j} \epsilon)}{\partial x_j} = \frac{\partial}{\partial x_j}\left[\left(\mu_L + \frac{\mu_t}{\sigma_\epsilon}\right)\frac{\partial \epsilon}{\partial x_j}\right] + \frac{\epsilon}{k}(C_{\epsilon 1}P_k - C_{\epsilon 2}\rho \epsilon) \tag{2.7}$$

Where the production of turbulent kinetic energy is given by:

$$P_k = -\rho \overline{u_i' u_j'} \frac{\partial \overline{u_i}}{\partial x_j} \tag{2.8}$$

and $C_\mu, C_{\epsilon 1}, C_{\epsilon 2}, \sigma_k, \sigma_\epsilon$ are empirical constants as defined by Launder and Spalding [94] and given as $C_\mu = 0.09, C_{\epsilon 1} = 1.44, C_{\epsilon 2} = 1.92, \sigma_k = 1.0, \sigma_\epsilon = 1.3$.

2.2.1.2 Launder-Sharma Low Reynolds Number $k - \epsilon$ Turbulence Model

Any low Re model requires additional terms for near-wall viscous diffusion, damping functions (which are functions of the <u>turbulent</u> Reynolds number (see below)) and possibly additional terms to improve the model's ability to capture the low Reynolds number effects which dominate near-wall behaviour. Some of the most widely used low Re model formulations of the damping functions have been proposed by Jones and Launder [105][51], and Launder and Sharma (LS) [95], with the latter selected here since it was found to perform well for highly accelerated, relaminarising boundary layer flows (see Trumper [104]) which are possibly to be found on the forward part of OGVs.

The LS low Reynolds number $k - \epsilon$ turbulence model can be written as:

$$\frac{\partial(\rho\overline{u_j}k)}{\partial x_j} = \frac{\partial}{\partial x_j}\left[\left(\mu_L + \frac{\mu_t}{\sigma_k}\right)\frac{\partial k}{\partial x_j}\right] + P_k - \rho(\epsilon^* + D) \tag{2.9}$$

$$\frac{\partial(\rho\overline{u_j}\epsilon^*)}{\partial x_j} = \frac{\partial}{\partial x_j}\left[\left(\mu_L + \frac{\mu_t}{\sigma_\epsilon}\right)\frac{\partial \epsilon^*}{\partial x_j}\right] + \frac{\epsilon^*}{k}(C_{\epsilon1}f_1 P_k - C_{\epsilon2}f_2\rho\epsilon^*) + E \tag{2.10}$$

The turbulent eddy viscosity in Eq. 2.9 and 2.10 results from:

$$\mu_t = c_\mu \rho f_\mu \frac{k^2}{\epsilon^*} \tag{2.11}$$

The quantity ϵ^* (the isotropic dissipation rate) is related to the total turbulent dissipation rate ϵ by:

$$\epsilon = \epsilon^* + D \tag{2.12}$$

where the function D is defined as:

$$D = 2\mu_L \left(\frac{\partial(k)^{\frac{1}{2}}}{\partial x_j}\right)^2 \tag{2.13}$$

Note that the turbulent dissipation rate ϵ has been replaced with the isotropic dissipation rate ϵ^*. This concept was first introduced by Jones and Launder [51][105] as a numerical simplification, allowing (because of the definition eq. 2.12) a value of ϵ^* equal to zero to be specified as a wall boundary condition. However, this introduces the term D, which is equal to the wall dissipation rate, and is required to balance the turbulent kinetic energy equation at the wall, but tends asymptotically to zero in the fully turbulent region where the isotropic dissipation rate must equal the total dissipation rate.

The function E in the transport equation for ϵ^* is defined as:

$$E = 2\mu_L \nu_t \left(\frac{\partial^2 \overline{u_i}}{\partial x_j \partial x_k}\right)^2 \tag{2.14}$$

and acts to increase the dissipation rate in the buffer region of the boundary layer to improve the performance of predicted peak turbulent levels.

Furthermore, the near-wall damping functions in the transport equations are defined as:

$$f_\mu = exp \left[\frac{-3.4}{(1 + \frac{Re_t}{50})^2} \right] \tag{2.15}$$

$$f_2 = 1 - 0.3exp(-Re_t^2) \tag{2.16}$$

$$f_1 = 1 \tag{2.17}$$

where Re_t is the turbulent Reynolds number and can be written as:

$$Re_t = \rho \frac{k^2}{\mu_L \epsilon^*} \propto \frac{\mu_t}{\mu_L} \tag{2.18}$$

The damping function f_μ is the most important since it features in both of the additional transport equations. Its purpose is to simulate the influence of molecular viscosity on the Reynolds shear stresses near the wall. The damping function f_2 is used to include low Reynolds number effects in the destruction term of the ϵ^* transport equation. Its effects are limited to the viscous sublayer, asymptoting to unity at $Re_t = 15$. The production term in the ϵ^* transport equation remains unchanged from the high Reynolds number counterpart so f_1 is equal to unity. The model coefficients $C_{\epsilon 1}, C_{\epsilon 2}$ and C_μ remain unchanged from the high Reynolds number form at the values as given above.

The system of Eqs. (2.1) - (2.4), together with the turbulence model equations, comprise a closed set of equations for RANS turbulence modelling at high or low Re level.

2.2.2 LES Flow Solver

The LES flow solver version of the DELTA code used in the present work solves the spatially filtered Navier-Stokes equations for constant density incompressible

flow, given by Eqs. (2.21) and (2.22) below. The general form of the spatial filter (Pope [12]) is written (an overbar now indicates a filtered variable):

$$\overline{u_i}(x_i, t) = \int G(r_i, x_i) u_i(x_i - r_i, t) dr_i \tag{2.19}$$

where, G is the filter kernel, a local function with a filter width Δ. Motions of scale $> \Delta$ are represented in the numerically resolved flow, smaller motions are filtered out. The most commonly used filter (adopted in DELTA) is the grid-cell-based top hat filter; which in 1D can be written:

$$G(x) = \begin{cases} \frac{1}{\Delta} & \text{if} (x - \frac{\Delta}{2}) < x < (x + \frac{\Delta}{2}) \\ 0 & \text{otherwise} \end{cases} \tag{2.20}$$

The resulting equations are in the same form as used for RANS:

$$\frac{\partial \rho \overline{u_i}}{\partial x_i} = 0 \tag{2.21}$$

$$\frac{\partial \rho \overline{u_i}}{\partial t} + \frac{\partial \rho \left(\overline{u_i} \overline{u_j} \right)}{\partial x_j} = -\frac{\partial P}{\partial x_i} + \frac{\partial}{\partial x_j} (\mu_L (\frac{\partial \overline{u_i}}{\partial x_j} + \frac{\partial \overline{u_j}}{\partial x_i})) - \frac{\partial \tau_{ij}^{Sr}}{\partial x_j} \tag{2.22}$$

Where P is given by:

$$P = \overline{P} + \frac{1}{3} \tau_{kk}^S \tag{2.23}$$

and τ_{ij}^{Sr} is the deviatoric part of the SGS stress tensor, given by:

$$\tau_{ij}^{Sr} = \tau_{ij}^S - \frac{1}{3} \tau_{kk}^S \delta_{ij} \tag{2.24}$$

where

$$\tau_{ij}^S = \rho \overline{u_i u_j} - \rho \overline{u_i} \overline{u_j} \tag{2.25}$$

The Smagorinsky[106] sub-grid-scale (SGS) model, which uses the Boussinesq assumption, is introduced to calculate τ_{ij}^{Sr}. The Smagorinsky model is based on an equilibrium hypothesis which implies that the small scales dissipate entirely and instantaneously all the energy they receive from the large scales. The algebraic

model takes the form:

$$\mu_{SGS} = \rho l^2 \overline{S} = \rho(C_s \overline{\Delta})^2 \overline{S} \qquad (2.26)$$

and the deviatoric part of the SGS stress tensor is given as:

$$\tau_{ij}^{Sr} = -2\mu_{SGS} \overline{S_{ij}} \qquad (2.27)$$

where $\overline{S_{ij}} = 1/2 \left(\partial \overline{u_i}/\partial x_j + \partial \overline{u_j}/\partial x_i \right)$ is the filtered strain rate tensor, $\overline{\Delta} = (\Delta x \Delta y \Delta z)^{1/3}$ is the filter length, $\overline{S} = (2(\overline{S_{ij}})(\overline{S_{ij}}))^{1/2}$ is the magnitude of the strain rate tensor and C_s denotes the Smagorinsky constant. Δx, Δy and Δz are grid sizes in the relevant directions.

In order to account for the reduced growth of the small scales near walls, the value of the SGS viscosity has to be reduced. Thus, the Smagorinsky model is modified according to Van Driest [107] near wall damping as:

$$\mu_{SGS} = \rho(C_s \overline{\Delta})^2 \overline{S} = \rho \left[C_{so}(1 - exp(-y^+/A^+))\overline{\Delta} \right]^2 \overline{S} \qquad (2.28)$$

where $C_{so} = 0.1$, $y^+ = y u_\tau / \nu$ and $A^+ = 25.0$. u_τ is the skin friction velocity, y is the wall normal distance and ν is the molecular kinematic viscosity.

2.3 Boundary conditions

A range of boundary conditions is available in DELTA; these include (among others), fixed velocity inlet, fixed inflow total conditions (total pressure and temperature), Euler (inviscid, slip) or viscous wall, symmetry, zero gradient or linear extrapolation outflow and fixed static pressure. These make the use of DELTA flexible for a very wide variety of flow types.

For the RANS predictions made in the current investigation, specified velocity and zero gradient outflow boundary conditions were applied respectively at the inlet and outlet planes. In previous CFD predictions of the OGV/prediffuser sys-

tem carried out during the LOPOCOTEP project [9], specified total pressure and flow angles at inlet and (measured) static pressure at outlet were used, since these were the 'natural' choice for the compressible CFD code used. In the present case, the switch from a measured static pressure at outlet to a zero gradient condition needs to be assessed as the upstream potential effect of the combustor pressure field is allowed for in the former condition but not in the latter. This was checked and will be presented as part of the CFD results reported in Chapter 3. Since for the current study, the computational domain consists of repetitive section azimuthally, a periodic boundary condition was utilised on opposite circumferential boundary planes to reduce the computational effort. Specified inlet conditions involve specification at each grid node in the inlet plane of values of all 3 mean velocity components, together with data for turbulent kinetic energy k and dissipation rate ϵ. If possible these should be taken from measurements and hence the experimental data provided in the LOPOCOTEP [9] study at rotor exit (OGV inlet), using both a pneumatic probe for velocity and a hot-wire for estimates of k and the integral length scale (and hence ϵ) are invaluable. The specified inlet condition treatment option existing within DELTA at the start of the project was restricted to simple uniform values (flat inlet profiles). This had to be modified to allow the user to apply specific 1D (e.g. radial) profiles or 2D (radial and azimuthal) data at the inlet. This then allowed the available experimental data to be used. Measured inlet data were interpolated based on cubic splines [108] method to determine values at cell centres.

As stated above, a zero gradient outflow boundary condition was employed at prediffuser exit. The outflow condition assumes a zero normal gradient for all flow variables such that:

$$\frac{\partial \phi}{\partial n} = 0$$

where n denotes the normal direction. The solver extrapolates the required information from the interior. Furthermore, an overall mass balance correction is applied as is normal with incompressible pressure-correction algorithms.

When using the high Reynolds turbulence model, the turbulence model equations

are not solved at the wall itself. The standard high Reynolds wall function approach, based on the logarithmic wall-law, was applied to provide the calculation of the wall shear stress needed in the momentum equations and deliver the values of k and ϵ at the node adjacent to a no-slip wall. Details of this approach are available in the published literature, for example [12] [5].

For the low Reynolds model, boundary conditions for all variables except at walls were described above. At no-slip surfaces low Re boundary conditions are easier to specify due to the practice of integrating the turbulence model equations all the way to the wall (although this places demands for a fine grid near the wall, see below). A simple zero velocity condition for all components is used together with the turbulence variable boundary conditions:

$$k = 0 \quad and \quad \epsilon^* = 0 \tag{2.29}$$

In the LES simulation, the same specified inlet velocity condition for all three components of velocity (as employed in the RANS) was applied. Of course, unlike in a RANS code, the LES velocity variables are a function of time as well as location in the inlet plane. As mentioned in Chapter 1, the issue of how to pre-specify a physically meaningful unsteady velocity field at an inlet plane is still a significant challenge, with the simple addition of periodic fluctuations (e.g. white noise) usually inadequate. In order to make more realistic unsteady perturbation for the LES inflow, a modified R^{2}M technique was introduced and details of this implementation will be described in Chapter 3. A zero gradient outflow condition and side boundary periodic conditions were set, and a wall-function approach was again used near no-slip walls, as in [103].

2.4 DELTA Code Discretisation and Solution Algorithm Features

The DELTA code adopts a finite-volume (FV) method to convert the governing partial differential equations into algebraic equations, which are then solved by linearised implicit matrix inversion.

For RANS solution, the spatial discretisation of all 2nd derivative diffusion term is carried out using central differencing. 1st derivative convective fluxes are discretised using a flexible method which may be summarised as a family of schemes ranging from central differencing to 1st order and higher order upwind via user-set parameters. The normal component of velocity at each cell face is computed by central differencing; the value of any dependent variable ϕ being convected through the cell face is found using a MUSCL-Type scheme (Monotone Upstream-Centred Schemes for Conservation Laws [109]); for example, for positive cell face velocity (with f indicating face and I a grid node)

$$\phi_f = \phi_{I-1} + \frac{1}{4}[(1-\kappa)\widetilde{\Delta}_- + (1+\kappa)\widetilde{\Delta}_+]\phi_{I+1} \tag{2.30}$$

where

$$\begin{aligned}
\widetilde{\Delta}_- &= minmod(\Delta_-, \beta\Delta_+) \quad \widetilde{\Delta}_+ = minmod(\Delta_+, \beta\Delta_-) \\
\Delta_-(\phi_I) &= \phi_I - \phi_{I-1} \quad \Delta_+(\phi_I) = \phi_{I+1} - \phi_I
\end{aligned} \tag{2.31}$$

and

$$minmod(x,y) = sgn(x) \times max[0, min[|x|, y \times sgn(x)]]$$

The parameter κ determines the discretisation scheme: $\kappa = -1$ is a second-order upwind scheme, $\kappa = 1/3$ a third order scheme, $\kappa = 1/2$ a low truncation error second order upwind scheme, and $\kappa = 1$ central differencing; β is a parameter controlling the strength of limiting. $\kappa = 1/2$ and $\beta = 0$ were chosen for the current RANS study, more validation cases of these two parameters have been reported by Veloudis in his thesis [86].

The simultaneous solution of the continuity and momentum equations in a pressure-correction approach involves the usual 'guess and correct' concept for pressure as described in detail in Ferziger and Perić [110]. A Gauss-Seidel line solver is used to solve the pressure-correction equation. For more details on the methodology, see Page et al [98], [99], [100], [101].

For LES solution, modifications were introduced to increase the spatial and temporal accuracy of DELTA when in LES mode. In the numerical scheme, for convection a higher-order discretisation using a total variation diminishing (TVD) principle was implemented as an explicit correlation to the basic upwind scheme. All diffusive terms were discretised using central differencing. An explicit time-stepping formulation employing a 3rd order accurate low storage Runge-Kutta[111] method was also introduced. Correct scaling of the Rhie and Chow smoothing terms was adopted to take account of the very small time steps needed in LES calculations, combined with very significant variations in cell volume size across the solution domain.

The introduction of the LES module in DELTA highlighted the need for parallelisation since the computational requirements of LES are significantly higher than the requirements imposed by RANS. Hence, the development of the code also involved the generation of a 'parallel' version that makes use of OpenMP (or Message Passing Interface,(MPI)) libraries to enable parallel processing based on flow domain decomposition.

2.5   Code Modification

To satisfy the requirements of the present study, a number of new features had to be introduced into the DELTA code. These were related to an improved method for grid generation, the implementation of new boundary conditions for RANS, realistic turbulent inflow generation for LES, and a new technique for zonal hybrid RANS/LES treatment.

1. A suitable mesh generator for geometries which include turbomachinery components was required for this project – the Rolls-Royce parametric blade meshing software PADRAM [112] was made available. It was then necessary to write a mesh filter program that could convert the output from the PADRAM software into a formatted mesh file that was compatible with the DELTA code (a plot3d file). Such a mesh filter program was written to provide all the mesh co-ordinates, connectivity and boundary information

for multi-block meshes required by DELTA. Examples of grids generated using this methodology are shown in Section 2.6.2 below.

2. A new 2D (contour map) specified velocity inlet boundary condition had to be implemented for the DELTA code. A separate module was written, according to which DELTA could read pre-specified two-dimensional input data for all required variables, and impose appropriate values at all necessary grid nodes on the boundary plane of interest. Development of this module will be described in section 3.2.1.

3. A modified Recycling and Rescaling method (R^2M) based on Lund et al's [90] and Pierce & Moin's [82][83] proposals and using the ideas described in Xiao et al. [93] was introduced. The developed method was applied to generation of realistic turbulent inlet condition for LES. Details and validation of the developed R^2M approach will be presented in section 3.3.2.

4. A novel 'adapter' methodology developed for zonal hybrid RANS/LES method was implemented. The 'adapter' methodology was based on use of an Algebraic Reynolds Stress Model (ASM) to carry out the evaluation of a set of <u>individual</u> normal stress components from a set of $k - \epsilon$ predicted mean velocity and turbulence fields. This set of normal stress components, together with the upstream RANS-predicted mean velocity field, were then treated as the 'target' data required by the R^2M approach to generate the time-dependent flow needed at inlet to the downstream LES zone. Details of this methodology will be described in Chapter 4.

2.6 Grid Generation

A test case with comprehensive experimental data was chosen from the review described in Chapter 1. The computational domain corresponded to a datum OGV/prediffuser assembly, which was part of the experimental study by Barker et al., in the EU project 'LOPOCOTEP' [9]. The 'LOPOCOTEP' project also developed an Integrated OGV/prediffuser (IOGV) design methodology, which allowed for vane shape variations (lean, sweep , trailing edge recamber), together

with simple axi-symmetric prediffuser area ratio changes, to be investigated, subject to fixed upstream and downstream boundary conditions taken from experiment, in order to produce an 'optimised' configuration. Essentially, changes in the OGV geometry were used to alter the resulting wake structure and secondary flows, encouraging transport of higher momentum fluid into the boundary layers. Thus, these 'energised' boundary layers were able to tolerate a higher adverse pressure gradient allowing the prediffuser flow to remain attached at an increased area ratio. Both "datum" and "IOGV" geometries were selected for use in the present study. In order to carry out the grid generation, an outline and explanation of the chosen testing case will be reported first in the following section.

2.6.1 Outline of Chosen Geometries

The primary chosen geometry details for this study are taken from the OGV/prediffuser part of a large annular gas turbine combustor aerodynamic test rig. The experimental test rig was introduced into a low speed isothermal test facility operating at nominally atmospheric conditions. Atmospheric air is drawn into a large inlet plenum, above the vertically mounted facility, then passed through an entry flare and honeycomb flow straightener, before entering the working section after a long straight annular duct (see Figure 2.1 (left)). The working section consists of an Inlet Guide Vane (IGV) row, rotor, OGV/prediffuser assembly and a representative downstream combustion system. Particular emphasis has been placed on establishing engine representative inlet conditions to the OGV/prediffuser/combustor external aerodynamics being investigated. Thus, a single-stage axial compressor rotor is located immediately upstream of the working section (Figure 2.1 (right)). This provides a reasonable compromise between capturing the main compressor/combustor interface flow features present within an engine environment, whilst avoiding the high cost associated with running a multistage compressor facility.

The compressor has an 80 blade Inlet Guide Vane (IGV) row in front of the rotor which is operated at a fixed non-dimensional condition $\dot{m}\sqrt{T}/p$ which at design corresponds to a flow coefficient ($\phi = Va/U$) of 0.403 and a non-dimensional
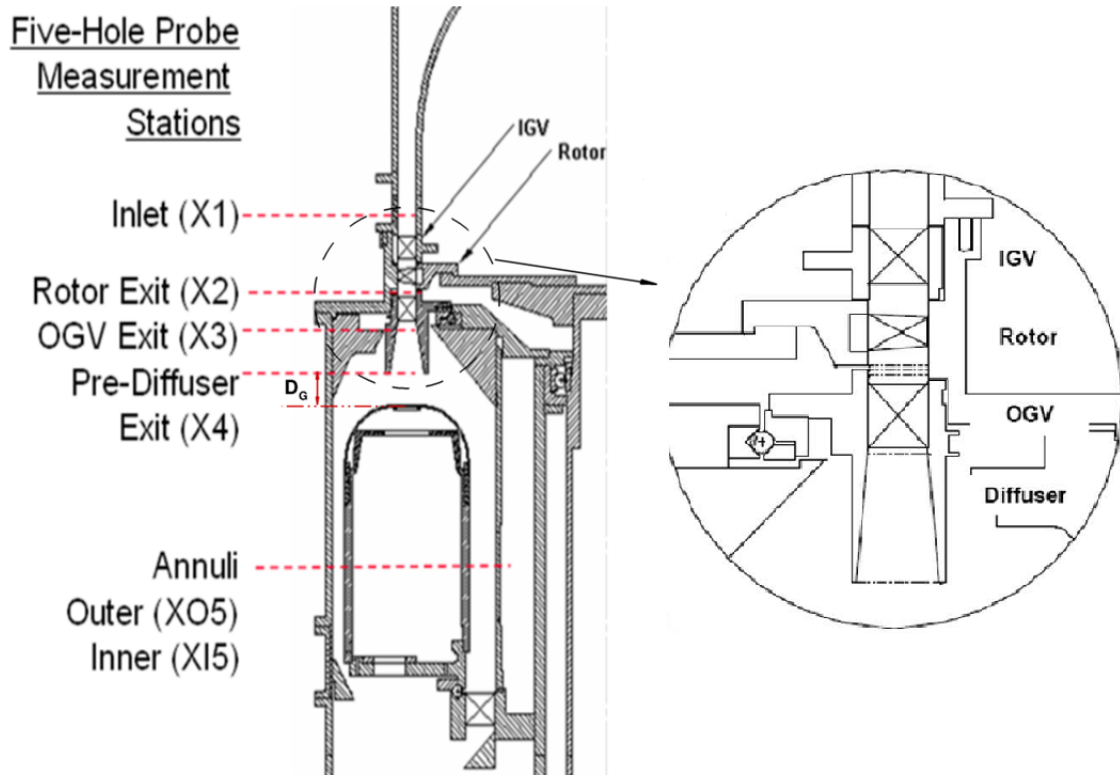
Figure 2.1: Working section of the test facility, indicating damp gap D_G
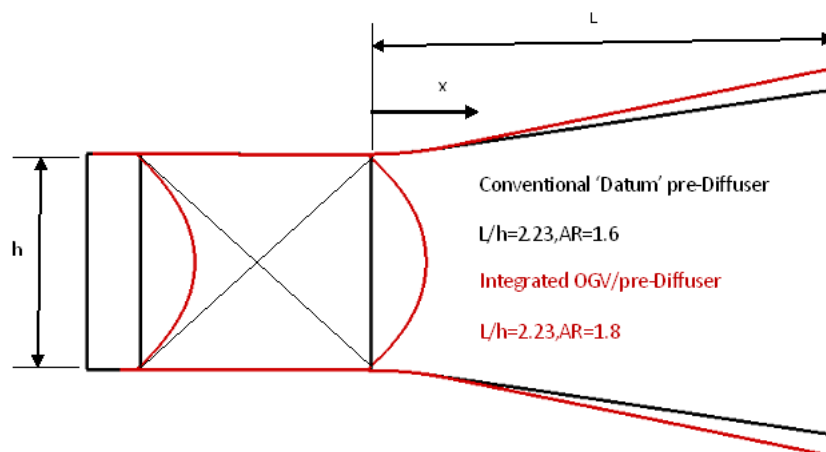
Figure 2.2: OGV/prediffuser geometries

speed ($N/\sqrt{T}$) of 168.7. At this condition the rotor provides approximately 45 deg of inlet swirl to the compressor OGV mid-passage height with a mass flow rate of approximately 4.6kg/s. This corresponds to a mean axial velocity through the blade rows of approximately 45m/s (Mach No.≈0.13). With these flow conditions, the OGV Reynolds number, based on inlet velocity and vane chord length, is approximately $Re = 1.6 \times 10^5$. The OGV row for this configuration consisted of 160 vanes (2 per IGV) each of 39mm chord length and with a thickness/chord ratio of 6 percent. The mean radius of the OGV blade row is 375mm with a passage height of 36.6mm. At OGV exit the blade row is connected to an annular diffuser of area ratio 1.6 (Conventional or datum OGV/prediffuser) or 1.8 (Integrated OGV/prediffuser), having an axial length (L) of 2.23 times OGV inlet passage height (h) (Figure 2.2). At the diffuser exit the flow enters a dump cavity where it divides to pass either directly into the combustor cowl of an annular flame tube or into the surrounding inner/outer feed annuli. The damp gap D_G was 1.4 OGV inlet passage heights. The flow splits between cowl/inner/outer annuli for the tests of interest was 30%, 35%, 35%. This configuration and flow specification establishes typical aerodynamic flow conditions for the OGV/prediffuser assembly.

As noticed above two types of OGV/prediffuser geometry have been chosen for study here. The first is a conventional OGV/prediffuser with datum blades (i.e. simple spanwise straight and fixed blade shape) and a prediffuser with area ratio of 1.6. The second case is the Integrated OGV/prediffuser geometry which has a diffuser ratio of 1.8 (increased area ratio compared to the datum 1.60), and a significant amount of blade sweep, with a small amount of trailing edge recamber but retaining the same aerofoil cross-section and chord length as in the datum OGV. (see Figure 2.2 for a schematic of the two geometries)

2.6.2 Grid Generation

DELTA can read a variety of grid file formats including PLOT3D files and mesh files produced by ICEM. Input grids have to be curvilinear structured and single or multi-block. As far as the application of boundary conditions and the exchange of information between blocks is concerned, DELTA uses two extra rows

of hallo-cells, generated automatically along each face of every block.

The computational domain for the numerical predictions extended from OGV
inlet (or rotor exit – station X2 in Figure 2.1 where experimental data were
available) to prediffuser exit (station X4 in Figure 2.1), and covered azimuthally a
2 OGV sector (an azimuthal segment of 4.5°) using periodic boundary conditions
at the corresponding side azimuthal planes. A 2OGV sector is required due
to the ratio of IGV to OGV blades, in order to capture IGV wake effects –
one OGV blade has an IGV in front of it (the right hand OGV looking from
downstream towards upstream) and one does not – as is shown in Figure 2.3.
As mentioned above, mesh generation was carried out using the Rolls-Royce
parametric blade meshing software PADRAM[112]. This provides a structured
multi-block grid designed specifically for meshing blades within annular or linear
cascades. In PADRAM, the distribution of cells can be tightly controlled by
specifying a number of parameters in an input file, for example to control the
clustering of cells around the blade leading and trailing edges. Further (design)
parameters can be specified to modify the blade geometry (for example to sweep
the blade or recamber the trailing edge).
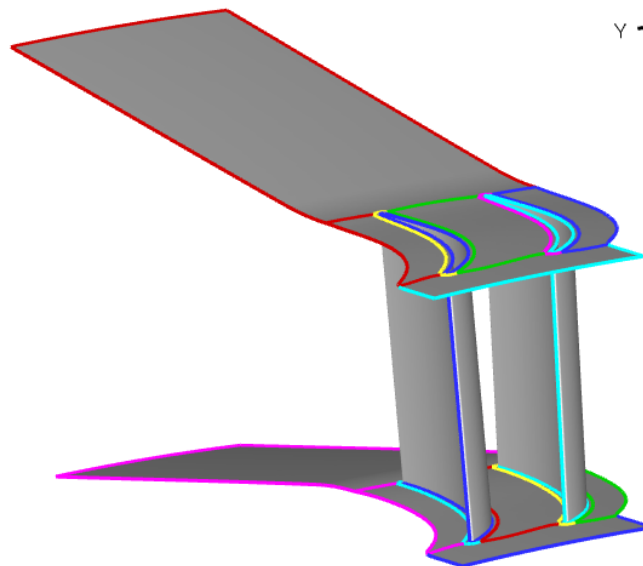
Figure 2.3: Computational domain

As noted earlier, the low Reynolds number turbulence model requires fine grids as the wall is approached. The standard requirement usually quoted is that the first node (or cell centroid) should be located at a distance $y^+ \leq 1$ from the wall, following the recommendation of Bardina et al. [113] who used the same low Re model as in the present work. In order to ensure accurate solutions near the wall, a mesh with $y^+ \leq 0.3$ for the first node was used for the low Reynolds number models predictions presented below. Typical nodal distribution near the vane surface is illustrated in Figure 2.4, which clearly demonstrates the more finer mesh needed near the wall for low Re calculation compared to high Re wall-function predictions.
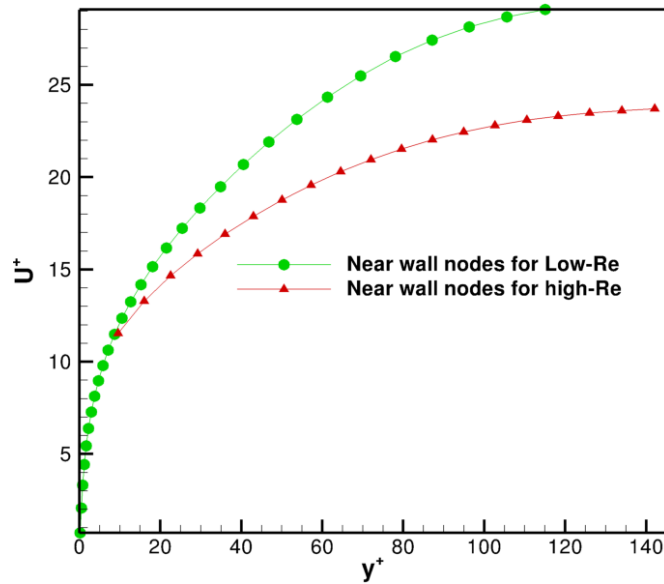
Figure 2.4: Near wall nodes distribution

Figure 2.5 shows the overall computational domain for the datum OGV and a low Re mesh, consisting of approximately 10 million hexahedral finite volumes. As shown in Figure 2.5, a 7 block topology(5 H-type for the OGV passage and prediffuser and 2 O-type grid for the vanes) was chosen, with 450 nodes axially around the OGV surface, 120 nodes azimuthally between the vanes, 120 nodes axially along the prediffuser length, and 120 nodes radially across the annular passage between end walls. Due to the meshing limitation of PADRAM, same

block topology and number of mesh nodes was retained for LES simulation (this may need further study for future LES simulation), but with different nodes distribution near the wall.

For the high Reynolds number turbulence model, the grid can be coarser near the wall with the first node distance corresponding to $\approx 300 \geq y^+ \geq 30$. The mesh applied for the high Re model calculations consists of approximately 8 million hexahedral finite volumes, in the same 7 block topology as in Figure 2.5, 450 nodes were again distributed axially around the OGV surface, but only 100 nodes azimuthally between the vanes.
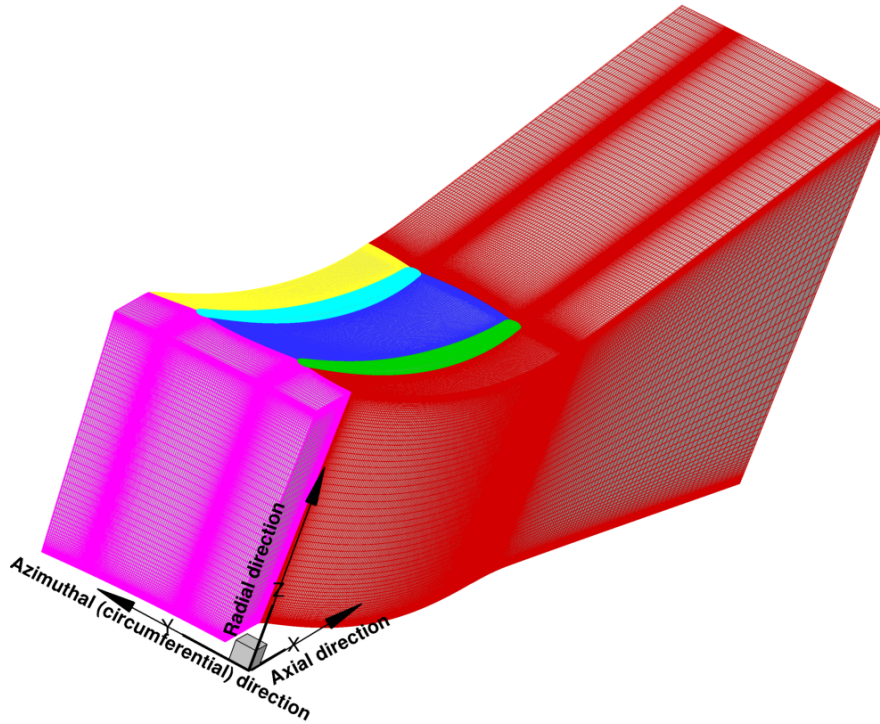
Figure 2.5: Datum OGV/diffuser mesh

Initially for RANS and LES predictions of the <u>whole</u> OGV/prediffuser geometry, attention was focused on the conventional OGV/prediffuser geometry. The geometry and mesh in the OGV region for the datum blade is shown in Figure 2.6 (High Re). For the hybrid RANS/LES study, both the conventional OGV/prediffuser

and the Integrated OGV/prediffuser were investigated. Figure 2.7 shows the geometry and mesh in the OGV region for the IOGV geometry.
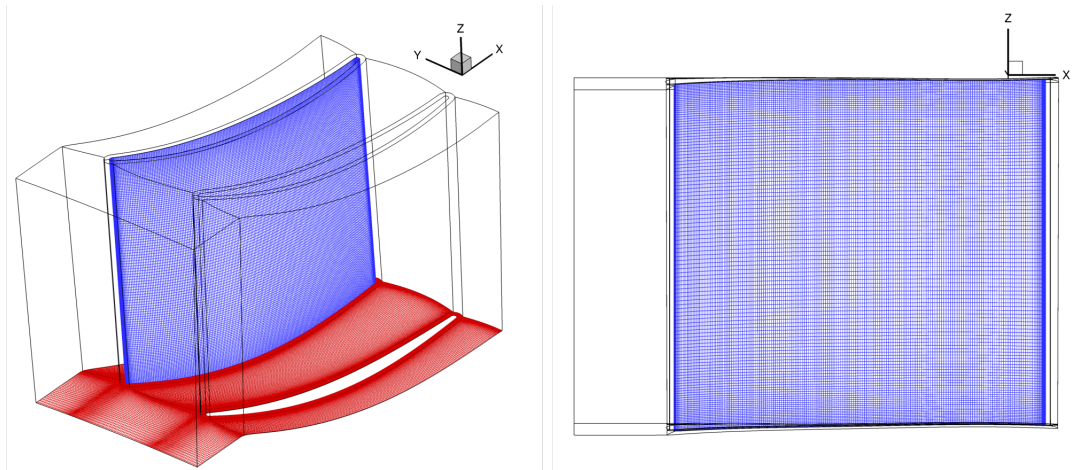
Figure 2.6: Datum blade geometry and mesh
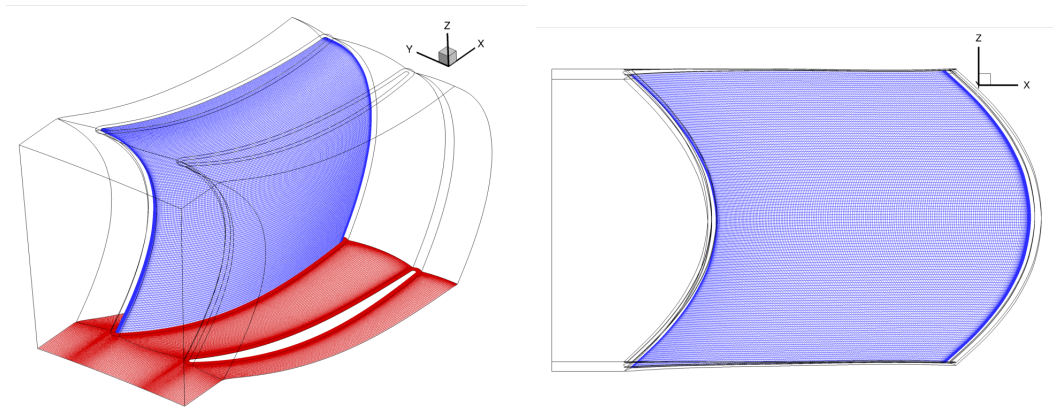
Figure 2.7: IOGV blade geometry and mesh

Chapter 3

RANS and LES Results

3.1 Introduction

In this chapter different flow solvers based on (i) time-averaged Reynolds-Averaged
Navier-Stokes equations (RANS) and (ii) spatially filtered LES equations are used
to predict the interaction between the wakes created by the flow over compressor
OGVs and the flow development in an annular prediffuser. In the first instance,
these two approaches to turbulence modelling will be used separately, in isolation,
i.e. a "pure" RANS and a "pure" LES formulation will be applied in turn. In the
RANS calculations, the classic high Reynolds number $k-\varepsilon$ turbulence model [94]
and the Launder-Sharma low Reynolds number $k-\varepsilon$ model [95] were used; ex-
perimentally determined [9] inlet conditions were applied. The Smagorinsky [106]
Sub-Grid-Scale (SGS) model was adopted in the LES simulation with simple Van
Driest damping [107] near walls, as described in the previous chapter. Many as-
pects of the computational set up are similar between the two approaches; the
RANS predictions are explained first, followed by the LES solution, outlining the
major differences in grid, boundary conditions, and of course results.

3.2 RANS Results

3.2.1 Inlet Boundary Conditions

Since the experimental measurements being modelled were taken in an essentially atmospheric pressure and temperature rig test, fluid properties such as density and molecular viscosity were set in all calculations corresponding to a pressure of 1 atmosphere and a temperature of 285K. Regarding flow conditions, a new specified velocity input routine was introduced. This allowed pre-specified 1D (radial) or 2D (radial/azimuthal) profiles to be input, since these had been measured in the experimental study [9]. An interpolation routine was established such that DELTA could read an input file with the required data, and impose appropriately all variable values on the inlet boundary grid plane at an arbitrary (user-set) number of grid nodes.

Since the number of entries in the data input file will usually be different from the number of boundary cells, and the co-ordinates of data locations will inevitably differ from finite volume (FV) cell-centre co-ordinates, an interpolation procedure is required. The procedure was developed for both 1D and 2D data input as noted above. In a similar exercise reported in Veloudis [114], a cubic spline interpolation had lead to numerical instabilities, and thus a bi-linear interpolation method was chosen. First the four input data (measurement) locations surrounding any particular FV cell location are identified, as shown in Figure 3.1. Then, a bi-linear interpolation (Eq. 3.1) is used to generate the appropriate value at the cell centre, where x, y here indicate spatial co-ordinates in the inlet grid plane. ϕ is any dependent variable of interest, subscript int indicates the interpolated value, i, j the input data neighbour values.

$$
\begin{aligned}
\phi_{int} = & \frac{\vec{x}_{i+1,j} - \vec{x}_{int}}{\vec{x}_{i+1,j} - \vec{x}_{i,j}} \left(\frac{\vec{y}_{i,j+1} - \vec{y}_{int}}{\vec{y}_{i,j+1} - \vec{y}_{i,j}} \phi_{i,j} + \frac{\vec{y}_{int} - \vec{y}_{i,j}}{\vec{y}_{i,j+1} - \vec{y}_{i,j}} \phi_{i,j+1} \right) \\
& + \frac{\vec{x}_{int} - \vec{x}_{i,j}}{\vec{x}_{i+1,j} - \vec{x}_{i,j}} \left(\frac{\vec{y}_{i+1,j+1} - \vec{y}_{int}}{\vec{y}_{i+1,j+1} - \vec{y}_{i+1,j}} \phi_{i+1,j} + \frac{\vec{y}_{int} - \vec{y}_{i+1,j}}{\vec{y}_{i+1,j+1} - \vec{y}_{i+1,j}} \phi_{i+1,j+1} \right)
\end{aligned}
\tag{3.1}
$$

For the currently selected experiment, the OGV inlet conditions are generated
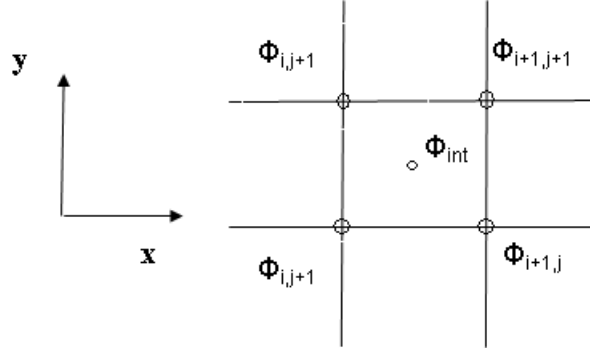
Figure 3.1: Neighbour input data values and the interpolated point

by a single stage axial compressor, and are characterised by high swirl, both radial and circumferential variations in axial velocity, as well as high turbulence. The measurements in the LOPOCOTEP study [9] were carried out with a 5-hole pressure probe (for mean velocity) over a 2 OGV sector at a plane between rotor exit and OGV inlet and defined here as the solution domain inlet plane. For turbulence measurement it was only possible to traverse a single hot-wire probe over a radial line at the same location, so only a radial profile was available. From the single radial hot wire traverse, after filtering out the periodic blade-passing contribution from the measured spectra, the data were processed (see [9] for detail) to provide estimated profiles of turbulence kinetic energy and integral length scale. By using the conventional relationship between energy, dissipation rate and length scale, the measured data could also be used to provide an estimate of the radial profile of turbulence energy dissipation rate ϵ. In order to provide a complete set of 1D (radial profile data), the 2D mean velocity data were also pitch-averaged in the circumferential direction to provide 1D radial profiles of the 3 velocity components, k and ϵ.

Figure 3.2 presents the radially and circumferentially resolved 2D map of all three velocity components as measured for the datum OGV. Note that the azimuthal distribution shows clear evidence of the influence of the IGV which is located on the right of the 2 OGV passage width. The axial velocity contours show the presence of end-wall boundary layers; the swirl distribution (v velocity) indicates

a nominal flow angle of approximately 45º within the central portion of the passage, and the radial velocity indicates the location of a tip vortex. Note that these contours are all non-dimensionalised using the bulk average axial velocity defined by the mass flow rate, density and the sector area.
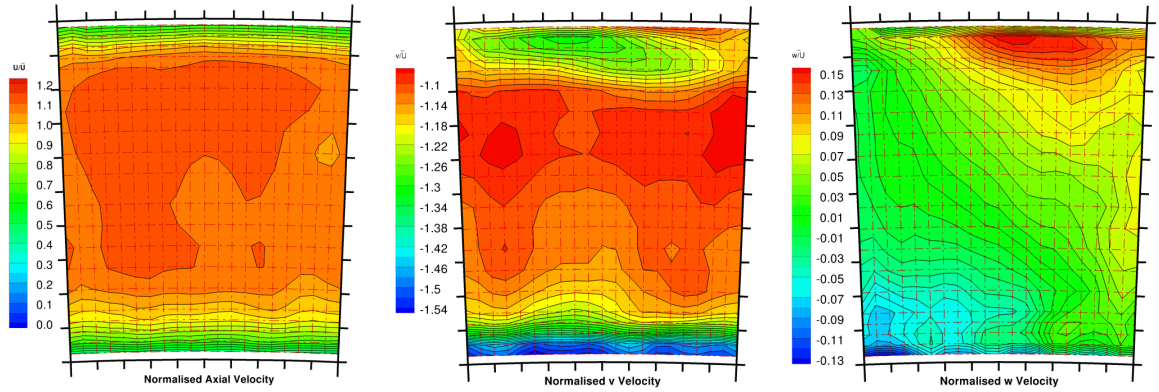
Figure 3.2: OGV inlet velocity contours from experimental data [9]
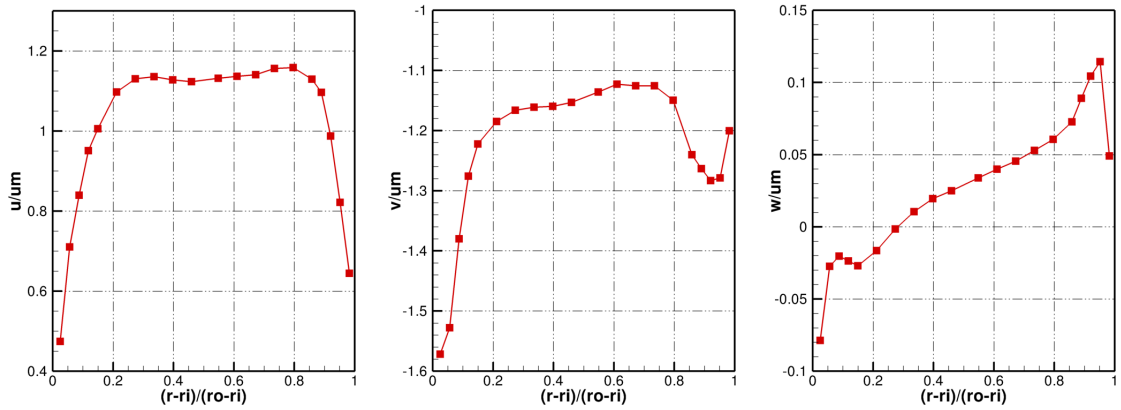
Figure 3.3: OGV inlet pitch-averaged velocity profiles from experimental data [9]

Circumferentially (pitch) averaged profiles (i.e. radially varying only) of all three velocity components derived from Figure 3.2 at rotor exit are presented in Figure 3.3. This form of presentation clearly identifies the thick boundary layers on the inner and outer end walls each amounting to approximately 20% of the passage

height. Note also that axial velocity and swirl velocity (u,v) are of similar magnitude but radial velocity (w) is $\approx$ one order of magnitude smaller.
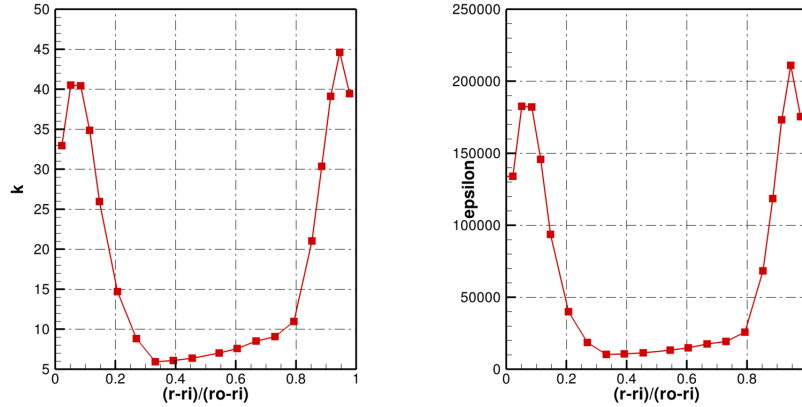
Figure 3.4: OGV inlet kinetic energy and dissipation rate profiles extracted from experimental data [9]

To complete the input data, the (dimensional) radial profiles of turbulent kinetic energy k and dissipation rate ϵ derived from the turbulence measurements are presented in Figure 3.4. High turbulence near the end walls and low levels of turbulence in the core are typical characteristic features of flows generated by an axial compressor rotor.

3.2.2 Grid Details

A grid refinement exercise was performed to identify the influence of grid resolution. Eight simulations were performed using the high-Re $k - \epsilon$ model. The grid resolutions used and the influence of the grid refinement on the pitch-averaged axial velocity profile at prediffuser exit are presented in Figure 3.5. Mesh resolution is characterised by Imax,Jmax,Kmax, which indicate axial, circumferential and radial directions respectively. These were set to give a total grid node number of $\approx$ 1 million cells to represent the mesh applied in the CFD work carried out during the LOPOCOTEP project [9]. This was then first refined in the I, J, K directions separately by factors of 2 and 4 respectively, then in both I,J and I,J,K directions

(2 times in each direction). Figure 3.5a shows that there is less than 1% difference between the 2 times and 4 times refined resolutions, but more evident differences between (2*Imax, Jmax, Kmax) and (2*Imax,2*Jmax,2*Kmax) resolutions (Figure 3.5b). Therefore, the mesh resolution with (2*Imax,2*Jmax,2*Kmax) was chosen as fine enough for the current flow field study for high Re RANS calculations.

(a)   (b)
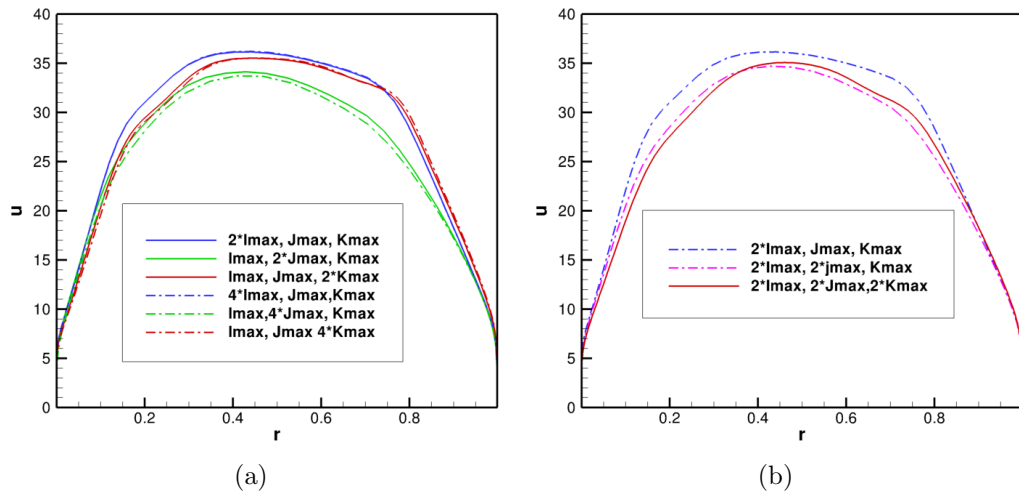
Figure 3.5: Pitch-averaged velocity profiles at prediffuser exit with different grid resolutions
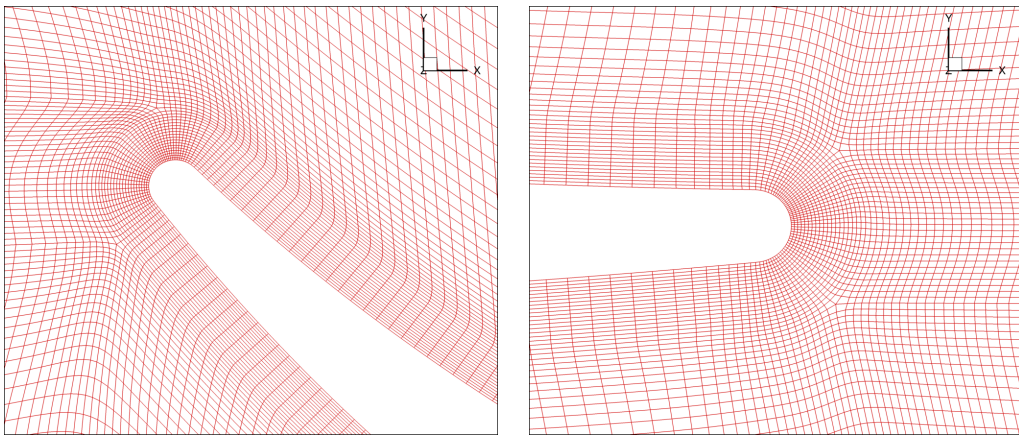
Figure 3.6: Mesh distribution in the vane leading and trailing edge (high-Re)

The final chosen grid resolution for high Re $k - \epsilon$ calculation consists of approx-

imately 8 million hexahedral finite volumes. Figure 3.6 shows the mesh distribution in the vane leading and trailing edge to demonstrate the quality of the mesh. Figure 3.7 shows the radial and axial direction grid distribution in the prediffuser. The prediffuser mesh in isolation contains 2.1 million mesh points with mesh points concentrated near the blade trailing edge in the axial direction and azimuthal mesh points concentrated in the wake mixing regions.
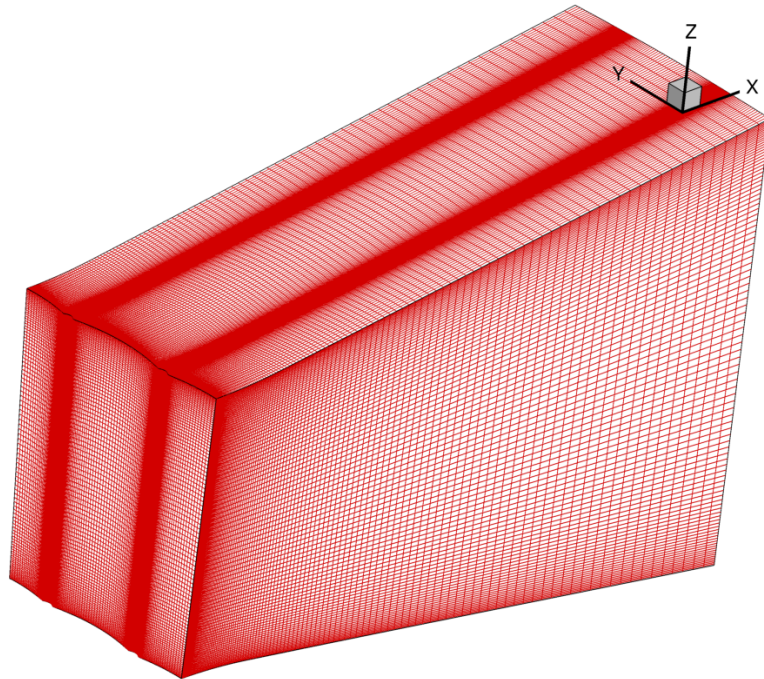
Figure 3.7: Mesh distribution in the prediffuser (high-Re)

In order to capture near wall behaviour, a more refined wall-layer resolving mesh was required for low Re $k - \epsilon$ calculation. The high Re grid resolution was therefore increased to 10 million cells. Figures 3.8 and 3.9 show the mesh resolution around the blade (leading and trailing edge) and in prediffuser respectively. By comparing Figures 3.8 with 3.6 and 3.9 with 3.7, it can be seen clearly that the mesh resolution close to the vane surface and prediffuser inner/outer walls is considerably finer for the low Re RANS calculation, 30% more nodes have been introduced near the vane surface and 20% more nodes towards inner/outer end walls compared with the high-Re mesh, although the same number of axial and
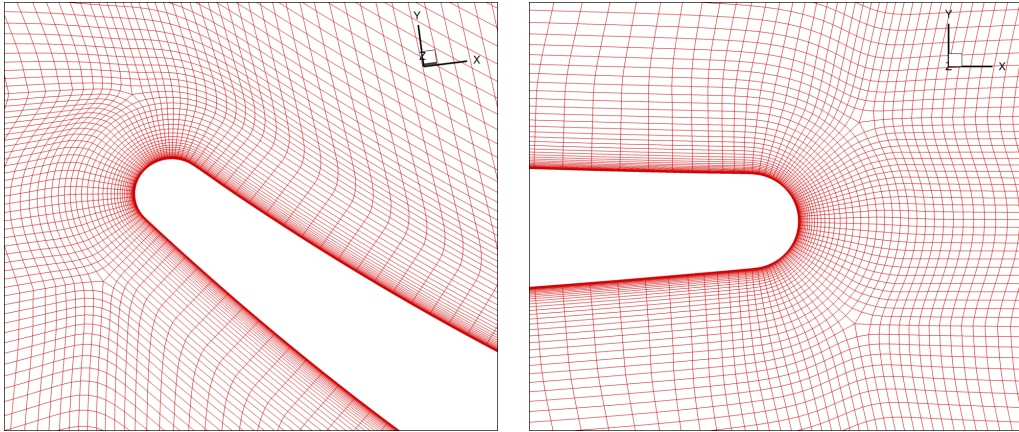
Figure 3.8: Mesh distribution in the vane leading and trailing edge (low-Re)
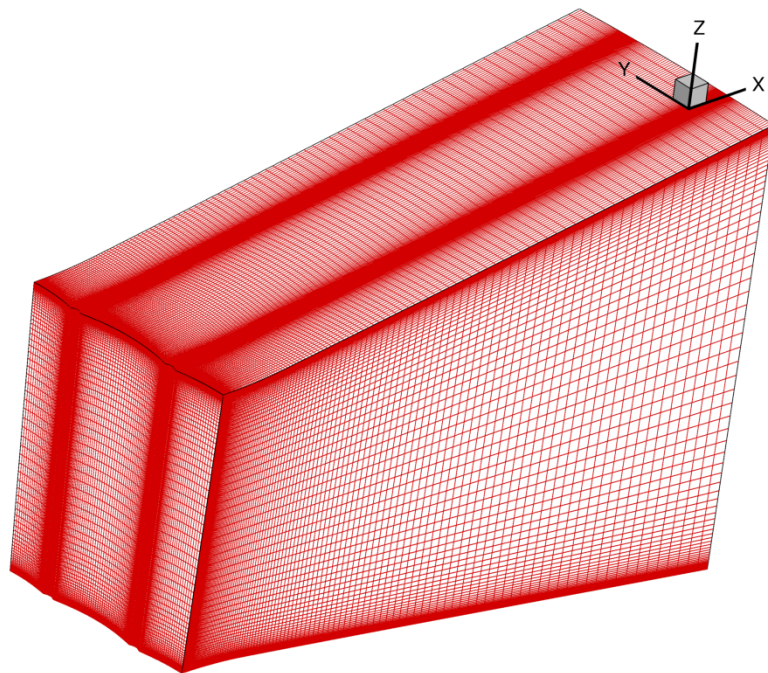
Figure 3.9: Mesh distribution in the prediffuser (low-Re)

spanwise direction nodes resolution has been used for both calculations as it was felt that the internal free shear layers were adequately resolved by the high Re mesh.

Typical predicted wall-normal U^+($U^+ = \bar{u}/u_\tau$, $y^+ = y u_\tau/\upsilon$) distributions near

the vane suction and pressure surface walls from both high Re and low Re calculations is presented in Figure 3.10 (located at the mid-chord on the vane, y is the distance from the wall). It can be noted that in the low-Re grid resolution the first grid point off the wall is at $y^+ \approx 0.3$ which is recommended for low Re calculations[113], whereas $y^+ \approx 10$ for the high Re mesh resolution which is smaller than recommended $y^+ \approx 30$.

(a) suction surface (b) pressure surface
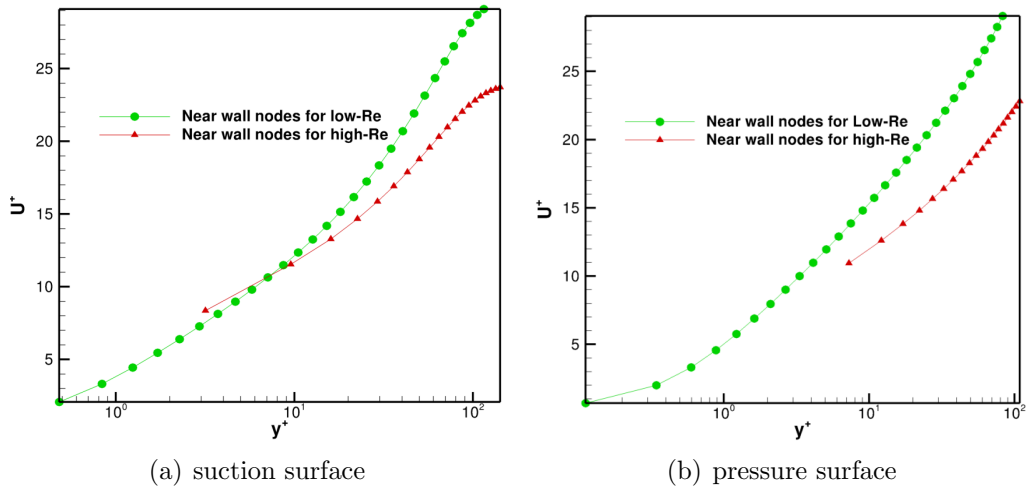
Figure 3.10: Mesh distribution on the vane suction and pressure surface

3.2.3 Illustration and Interpretation of Flow Development

In order to introduce the main features of the flow development through the OGV/prediffuser assembly, this section presents results (from the high Re model only) which illustrate the important aerodynamic characteristics. This is done in two parts. First the flow over the OGV surface is examined, and secondly the development of the OGV wake flows through the prediffuser is highlighted.

Figures 3.11 and 3.12 show the flow development from the vane leading edge to the trailing edge via axial velocity and turbulent kinetic energy contours close to the vane walls (at location dy/s=6% from the vane, dy indicates distance from the vane wall and s indicates spanwise distance between the vanes) for both 1D (radial profiles only) and 2D (velocity contour input + 1D k, ϵ profiles) inlet

(a) 1D   (b) 2D
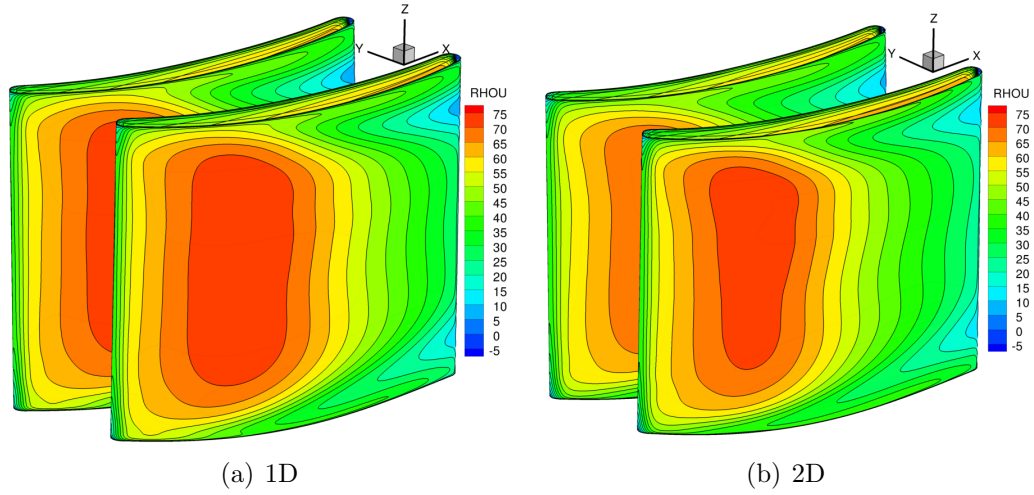
Figure 3.11: Axial velocity contours on the OGV suction surface (dy/s=6%)

(a) 1D   (b) 2D
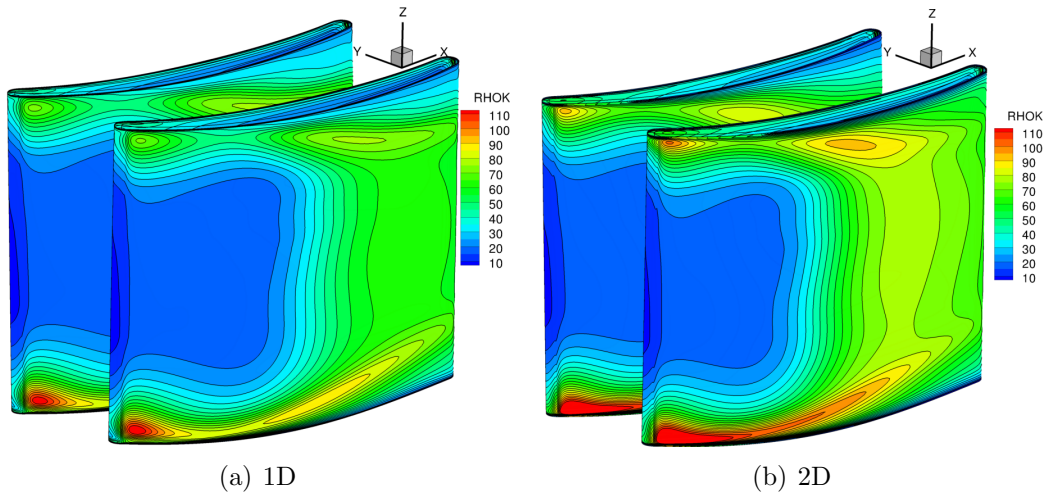
Figure 3.12: Kinetic energy contours on the OGV suction surface (dy/s=6%)

conditions. The flow over the leading edge is seen to be 2D over much of the span, but the interaction of the end-wall boundary layers and the acceleration over the leading edge creates 3D secondary flows that give rise to two regions of low momentum near the vane hub and tip endwalls. These features can be identified with the two peaks in the inlet swirl velocity profile associated with the rotor characteristics (see Figure 3.3). Both inlet boundary condition options predict similar flow development, but the 2D inlet condition predicts greater ac-

celeration around the blade leading edge, more spanwise non-uniform flow and stronger secondary flows shown via the higher turbulent kinetic energy near the hub and tip endwalls (Figure 3.12). The larger 'streak' of higher turbulence near the hub is particularly noticable with 2D inlet conditions. Note the patch of very low turbulence emanating from the leading edge, which is slightly smaller with 2D inlet conditions. The turbulence level begins to grow very rapidly on the vane surface when the region of rapid flow deceleration (adverse pressure gradient region) begins. Near the trailing edge there are two zones of very low velocity, close to predicted separation, associated with the low momentum flow in the two secondary flow regions near hub and tip.

Attention is now moved to the development of the OGV-created velocity field as this passes through the annular prediffuser (axial velocity component only). Figure 3.13 indicates how the wakes generated by the upstream vane row develop as influenced by the superimposed effects of turbulent mixing due to turbulent shear stresses and the adverse pressure gradient generated by the prediffuser area ratio. The OGV wakes which initially are fairly thin (although showing effects of wake/end wall boundary layer merging near hub and tip) grow in thickness in the central part due to mixing. The growth in the low momentum regions leads to two clearly identifiable "islands" of high velocity, whose extent and shape is determined by the mixing process and also the secondary flow velocities; The secondary velocity field, particularly as it interacts with the end wall flows, leads to curved distortions of the axial velocity contours (principally in the hub/tip regions). The maximum velocity in the core of these islands decreases due to adverse pressure gradient effects. One noticeable feature of the 2D inlet predictions is the different shape and contour levels of the 2 high velocity regions due to IGV effects, which are of course absent in the 1D inlet predictions.

The secondary velocity field created by the OGV is shown in Figure 3.14. There is some evidence that the circumferential flows are predicted to be stronger in the 1D inlet profile approach. The flow contains very little swirl compared to OGV inlet, although there is evidence of some predicted overturning at the OGV trailing edge (the azimuthal velocity on the right side of the trailing edge is in the
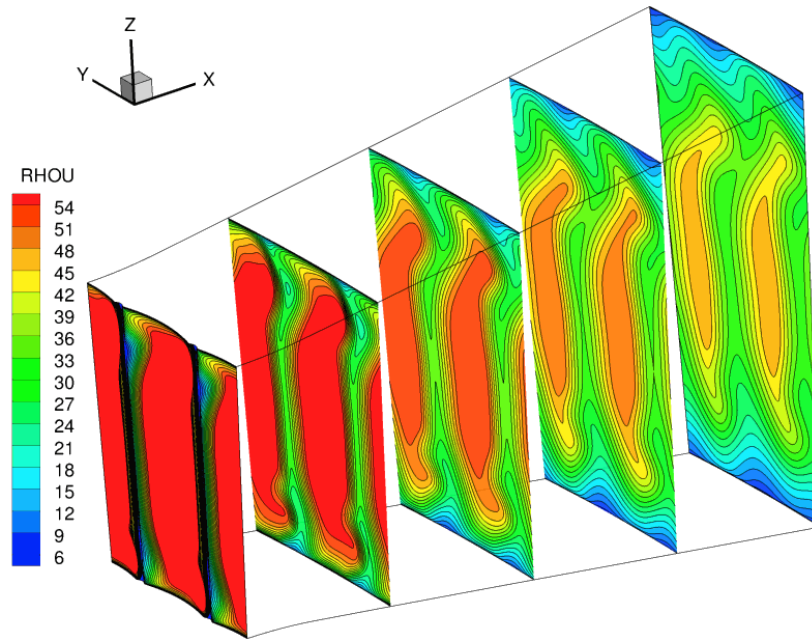
(a) 1D inlet
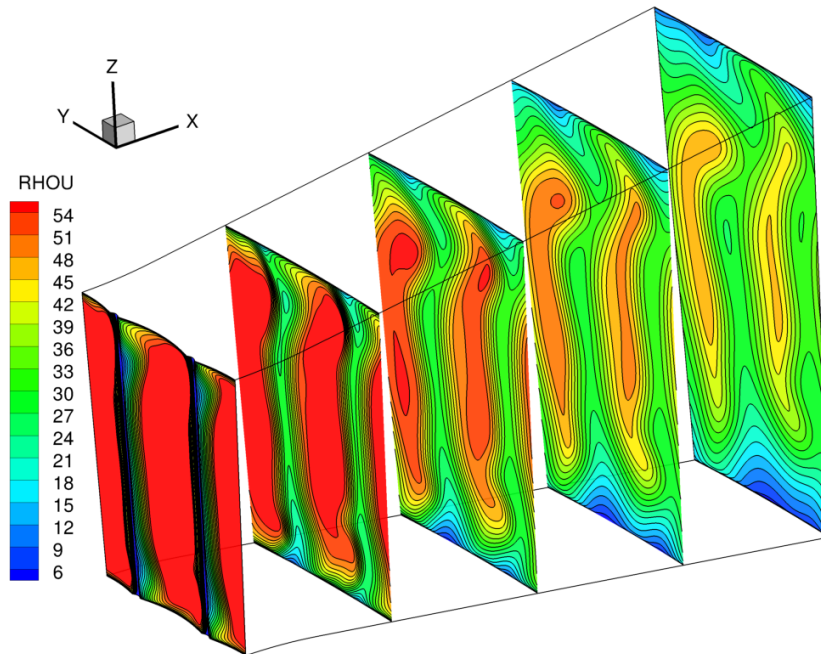
(b) 2D inlet

Figure 3.13: Axial velocity contours through the diffuser.

opposite direction to the inlet swirl, as viewed upstream). The 1D/2D inlet differences are most noticeable in the vortex in the upper corner of the end-wall/vane suction surface; for 1D conditions it is of course the same on both vanes, for 2D it is noticeably stronger and larger on the right hand vane. Note that there is little radial velocity in the secondary field.

The secondary flows are also responsible for the accumulation of low momentum fluid in the two thickened wake regions which combine with the end-wall boundary layers to form the two distinct low momentum regions seen in the vane surface plot (Figure 3.11). As noticed above, these regions are where separation would take place first, but for the diffuser length/area ratio present in the datum design no negative velocities are predicted by the high Re model.

(a) 1D inlet   (b) 2D inlet
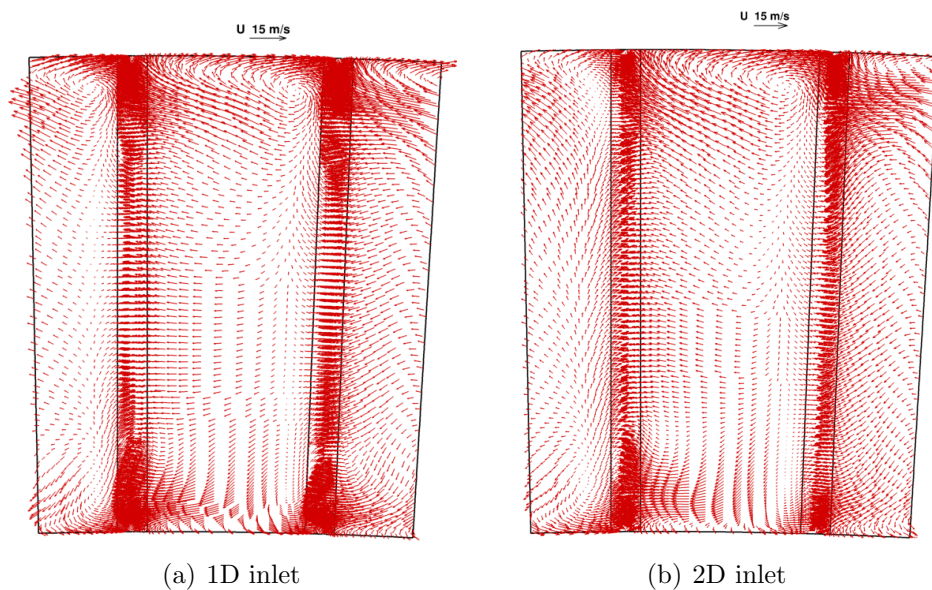
Figure 3.14: Secondary vector at OGV exit.

The IGV is located upstream of the <u>left</u> OGV in the view shown in Figure 3.13, (which looks downstream) and shows the stronger velocity flow associated with the left OGV and a larger island of high velocity compared to the right OGV. A close-up view (now looking upstream) of the predicted axial velocity contours at prediffuser exit is provided in Figure 3.15. The 2D inlet boundary conditions have a noticeable effect, not just on the shape and velocity magnitude in the high

(a) 1D inlet   (b) 2D inlet with zero gradient   (c) 2D inlet with static pres-
                outlet BC   sure outlet BC
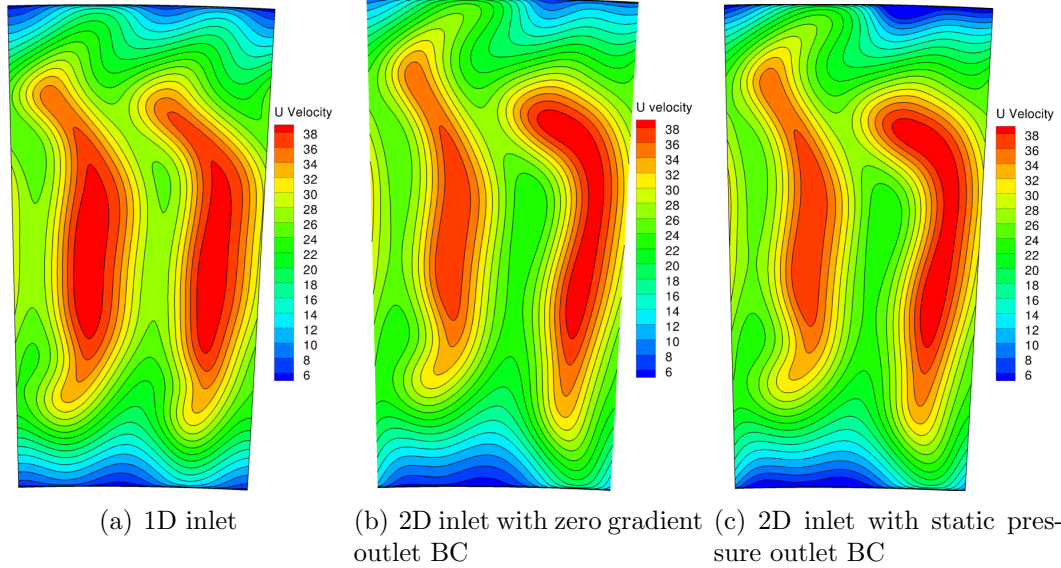
Figure 3.15: Axial velocity contours at diffuser exit.

momentum islands, but also the regions close to separation near the end walls. The region predicted to be the closest to separation is in the bottom left hand corner for both inlet conditions, but is clearly radially larger when the details of the inlet flow are provided more accurately by 2D inlet conditions. The different development of the adjacent OGV wakes, due to the existence of an upstream IGV wake persisting through the rotor, is clearly visible in the 2D inlet prediction.

Comparisons between RANS solutions with zero gradient outflow condition and measured static pressure outlet condition are also presented in Figure 3.15. The axial velocity contours at prediffuser exit, resulting from calculations with these two outlet boundary conditions, show only slight differences with the largest difference (less than 1%) near the right side of the outer end wall. This shows that the potential upstream effects of the combustor pressure field are negligible in this particular configuration. Therefore, in order to keep comparisons consistent between RANS and LES simulations, the use of zero gradient outflow boundary condition for all RANS and LES calculations is reasonable.

In experimental and design considerations, circumferentially pitch-averaged pro-

(a) dx/L=0.01

(b) dx/L=0.22

(c) dx/L=0.44

(d) dx/L=1.0
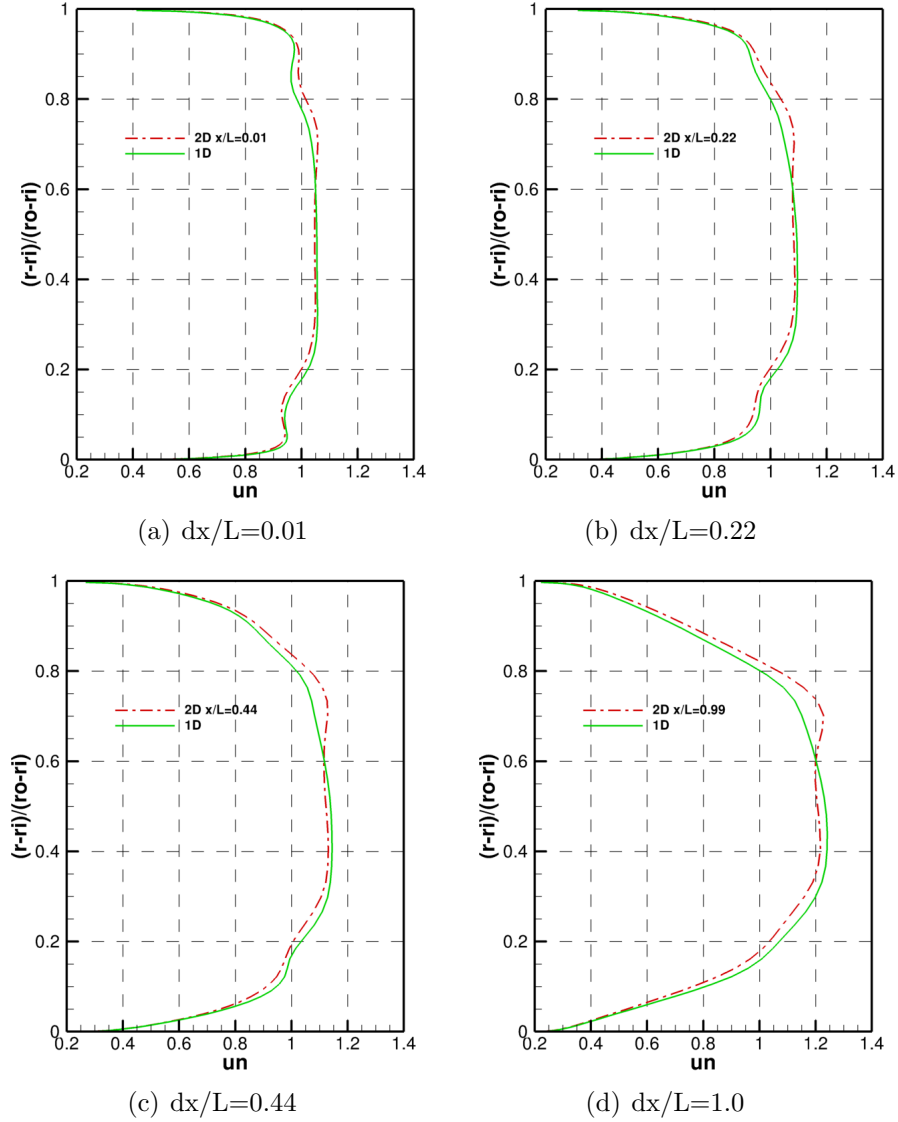
Figure 3.16: Circumferentially-averaged axial velocity profiles through the prediffuser

files are often used for performance assessment and these are shown for both sets of inlet conditions in Figure 3.16 plotted against radial height, at x/L=0.01 (OGV exit), 0.22, 0.44 and 1.0 (prediffuser exit). Due to the adverse pressure gradient, strong deceleration of the boundary layer regions occurs throughout the prediffuser, although, as noted above, the flow is predicted to remain attached on both endwalls. At prediffuser entry both 1D and 2D solutions show very similar

shape (profile normalised by bulk inlet velocity) with an essentially flat profile, boundary layers of $\approx 5\%$ thickness and profile distortion due to the hub/tip secondary flow. As the flow passes down the prediffuser the boundary layers grow, the profile shape becomes peakier, with this predicted to be smoother in the solution from 1D inlet profiles.

Flow development can also be viewed in terms of axial velocity contours on various planes. Figure 3.17 shows a radial plane mid-way between OGVs and Figures 3.18 and 3.19 an azimuthal plane at mid-annulus height. The acceleration of the flow and axial momentum field development can be seen clearest in Figure 3.17. The lower end wall boundary layer can also be seen to come closer to separation towards prediffuser exit. Figures 3.18 and Figure 3.19 present pictures of OGV wake flow development as represented by axial velocity and static pressure. The stagnation region at the vane leading edge is evident, as is the very high acceleration over the OGV suction surface with the velocity more than trebling in $\approx$ 1/3rd chord length. The boundary layer growth on pressure/suction surface and their merging to form the OGV wake is particularly clear in Figure 3.18. Note also how quickly the high spatial gradients in static pressure caused by the OGV are smoothed out, so that the prediffuser pressure field becomes circumferentially flat very quickly.
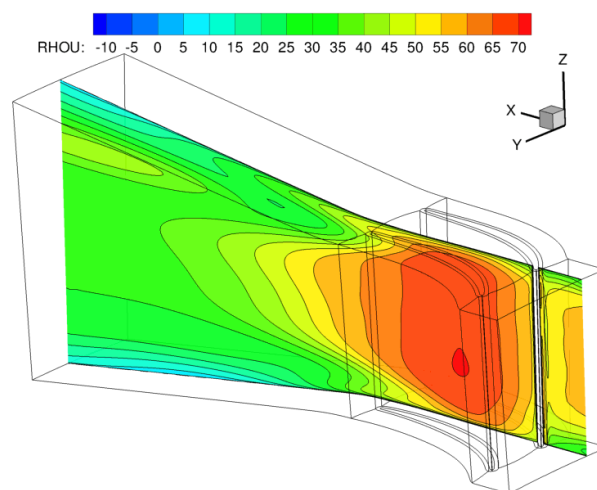
Figure 3.17: Axial velocity contours (high-Re, 2D inlet, mid OGV passage plane)
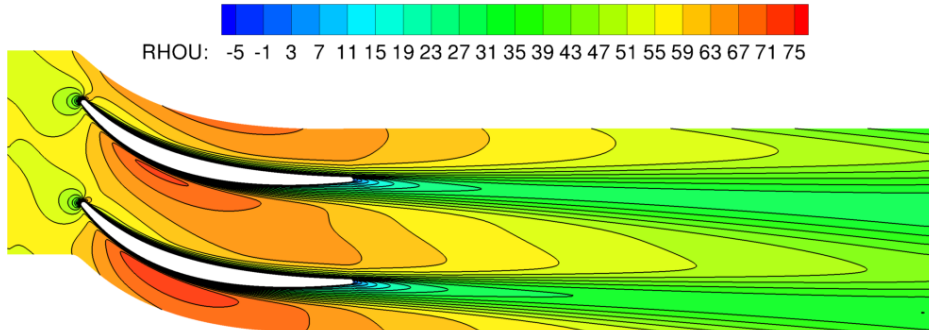
Figure 3.18: Axial velocity contours (high-Re, 2D inlet, mid annular height)
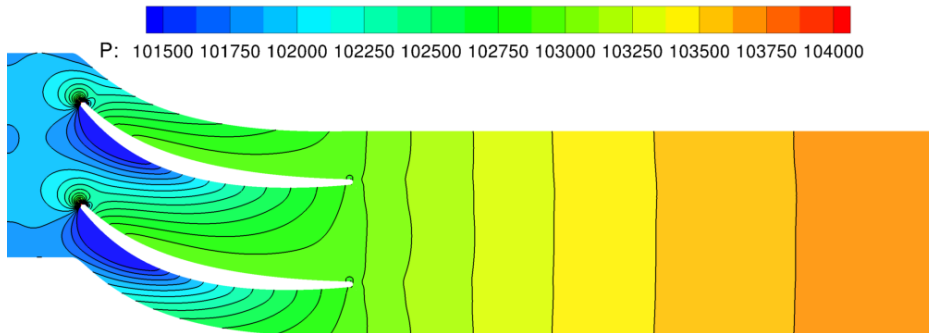
Figure 3.19: Pressure contours (high-Re, 2D inlet, mid annular height)

Within the prediffuser, the steep velocity gradients in the wake generate large turbulent shear stresses, which reduce as the wake mixes out; the pressure forces associated with the increasing area duct then start to dominate flow development. The pressure rise occurring in the downstream prediffuser is enhanced by this mixing out of vane wakes, which contributes to the rapidity with which the pressure field becomes spanwise uniform.

3.2.4 High Re and Low Re $k - \epsilon$ Results and Comparison to Expts.

The results from both classic high Re and low Re (Launder-Sharma) $k - \epsilon$ models are discussed in this section, initially focusing on the major differences caused

by changing model and then by comparing with experimental data. Considering the differences in the predicted flow field brought about by the use of the more detailed 2D inlet conditions, all predictions in this section are taken from calculations using the 2D inlet data.

(a) High-Re
(b) Low-Re
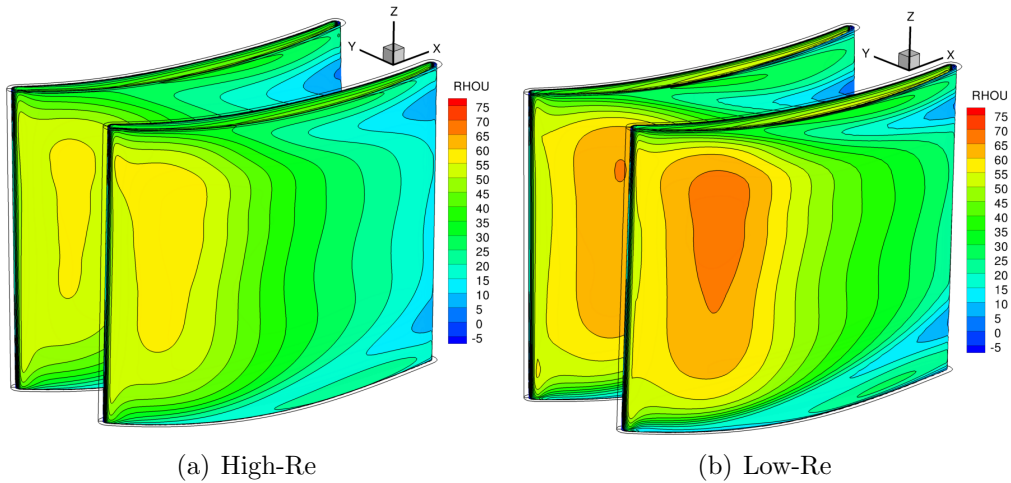
Figure 3.20: Axial velocity contours on the OGV suction surface (dy/s=2%)

(a) High-Re
(b) Low-Re
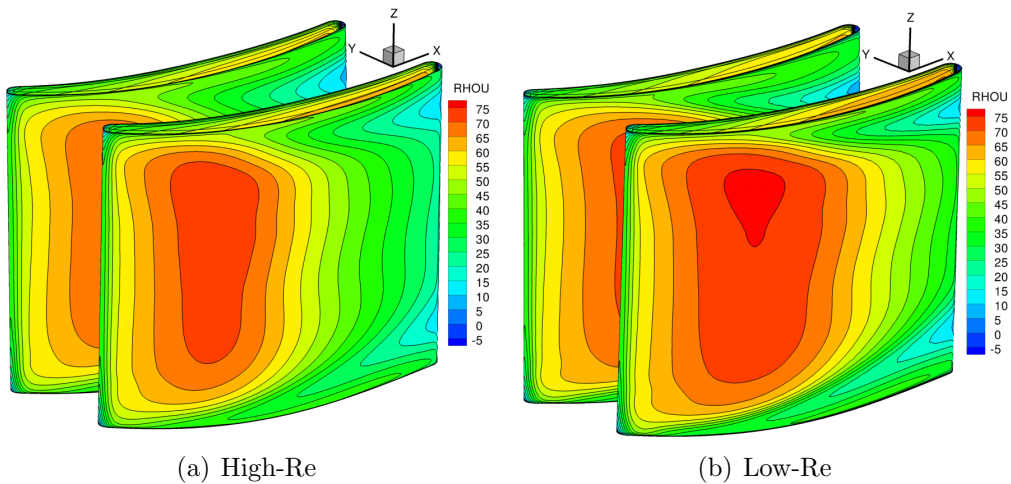
Figure 3.21: Axial velocity contours on the OGV suction surface (dy/s=6%)

Figures 3.20 and 3.21 present axial velocity contours close to the vane suction side surface (normal distance dy/s=2% and dy/s=6% from the vane wall respectively,

s indicates spanwise distance between vanes) for both high Re and low Re models. Both turbulence models predict rather similar flow development, but the low Re model produces greater and a larger region of flow acceleration around the leading edge particularly outboard near the vane tip, and hence stronger secondary flows as will be shown later (Figure 3.26). The low momentum region close to the hub end wall appears earlier in the low Re prediction, but the velocities are in fact smaller in the region near the tip end wall, which is close to separation near the trailing edge, although no separation is observed in the suction surface boundary layer with either model. On the plane close to the vane surface, the low Re model shows two distinct trailing edge regions of slow flow, but the high Re model indicates some merging of these. The very thin nature of these low momentum regions may be judged from the low values of dy/s needed to visualise these.

Predicted contours of axial, radial and circumferential velocity components at OGV exit are illustrated in Figure 3.22. The two low momentum regions on the OGV identified above can be seen to form two zones of thicker wake in the axial velocity contours and two 'bulges' in the lowest (blue coloured) contours in the otherwise thin wakes. The wakes are noticeably thicker on the OGV suction surface side as expected due to adverse pressure gradients, but the difference between high and low Re models is relatively small. In comparison with the measured axial velocity field, the overall patten is well represented, the measured wake is certainly thinner than predicted, with the low Re model perhaps providing a marginally better level of agreement. Both predicted solutions indicate a deeper wake than measured with small negative velocities in both high and low Re solutions; the measured data, taken with pneumatic probes, would in any case not be able to capture any small recirculation zones present.

The secondary flows generated by the upstream vane are represented in Figure 3.22 via the radial and circumferential velocity contours and in Figure 3.23 via secondary flow vectors. Only a small amount of residual swirl remains, predominantly associated with the low momentum regions identified in the axial velocity field. The regions where the vane has not removed all the rotor swirl velocity are

(a) high-Reynolds

(b) low-Reynolds

(c) measured data
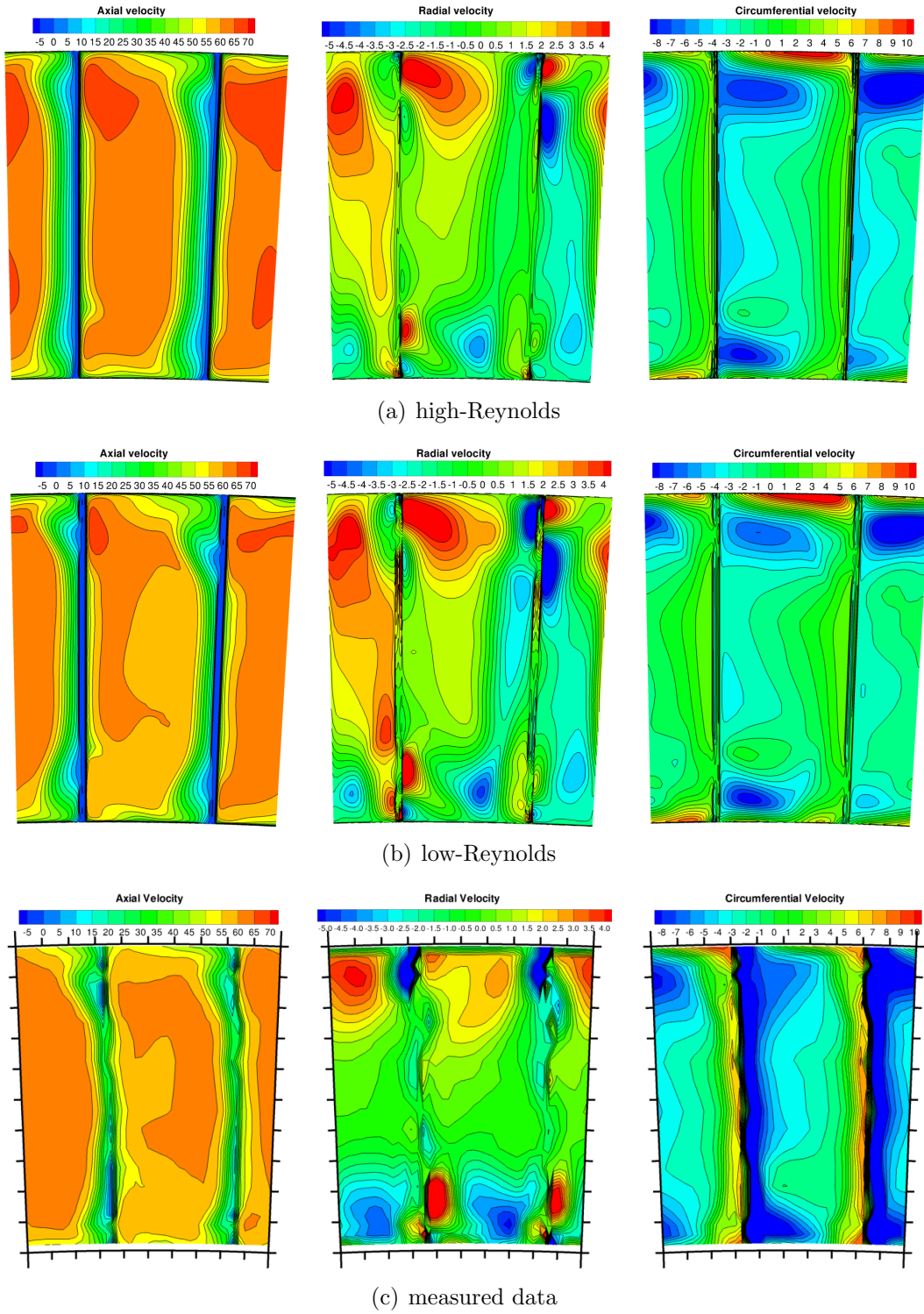
Figure 3.22: Predicted OGV exit velocity contours

smaller in the high Re model. In general, comparison with the measured velocity components shown in the bottom part of Figure 3.22 shows good agreement in terms of the pattern of velocity distribution in all components, and good agreement in terms of magnitude.

In the secondary flow vector field (Figure 3.23), compared with the measured data both high Re and low Re models predict the same main secondary flow trends and the underturning in the central part of the vane, whilst the high Re model prediction is perhaps closer to the measured data but the low Re model shows more detailed flow information near the outer and inner end walls which are not covered in the measurments. On the basis of this first comparison with measured data at least, it has to be concluded that the low Re model does not seem to have brought large improvements.

(a) High-Re   (b) Low-Re   (c) Measured data
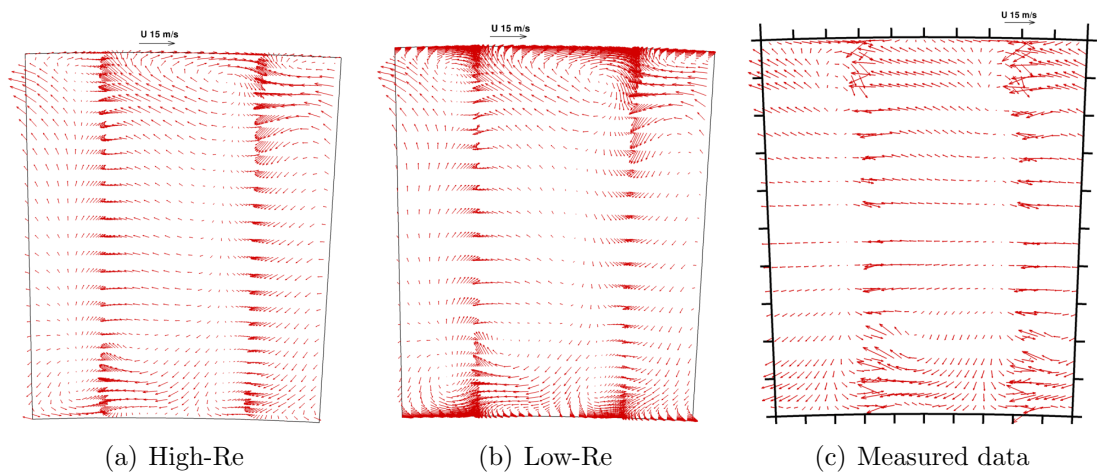
Figure 3.23: Secondary flow vectors at OGV exit

Figure 3.24 uses the axial velocity contour development in several radial/azimuthal planes over two OGV sectors to capture the wake mixing out process over the prediffuser length. The small difference between the two wakes at OGV exit resulting from the propagation of the IGV wake through the rotor seems to be magnified as the flow passes down the prediffuser so that the contour pattern associated with each OGV passage flow is easily distinguished at prediffuser exit.
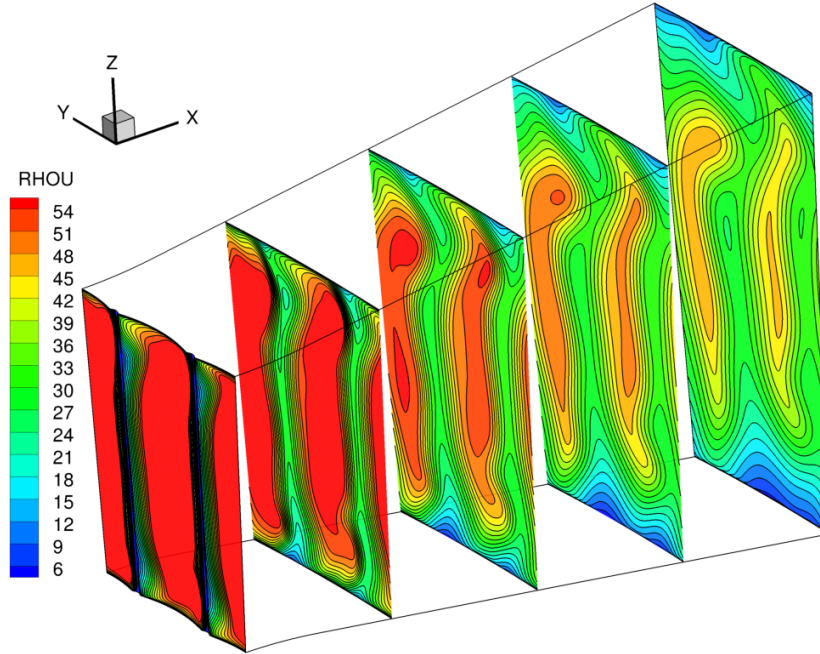
(a) High-Re
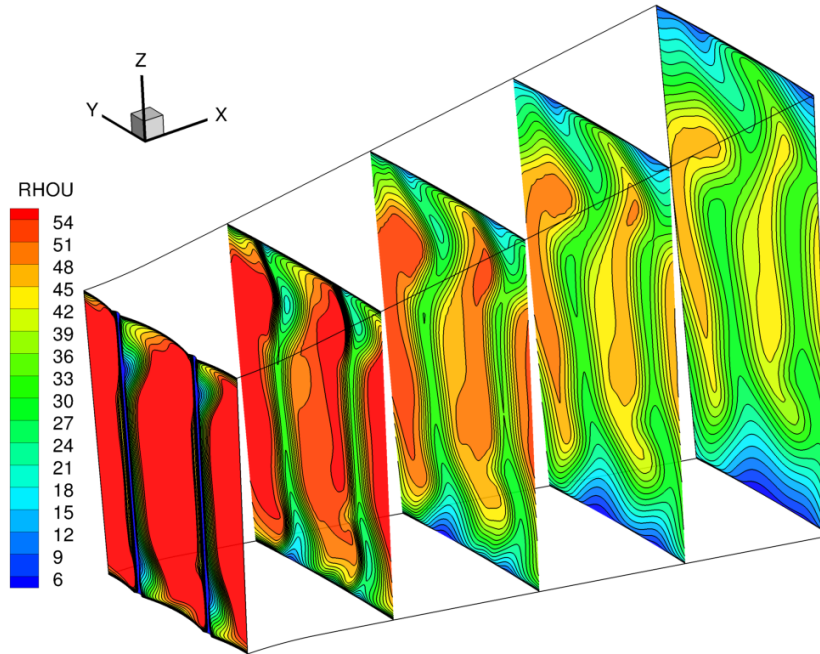
(b) low-Re

Figure 3.24: Axial velocity contours through the prediffuser.

Both high-Re and low-Re models show essentially the same characteristics of the wake development. The stronger secondary flows noted above for the low-Re model produce more curved contours and a larger difference between the two OGVs. The right hand OGV passage (in Figure 3.24) has mixed out more quickly in the low Re model predictions.

(a) High-Reynolds

(b) Low-Reynolds
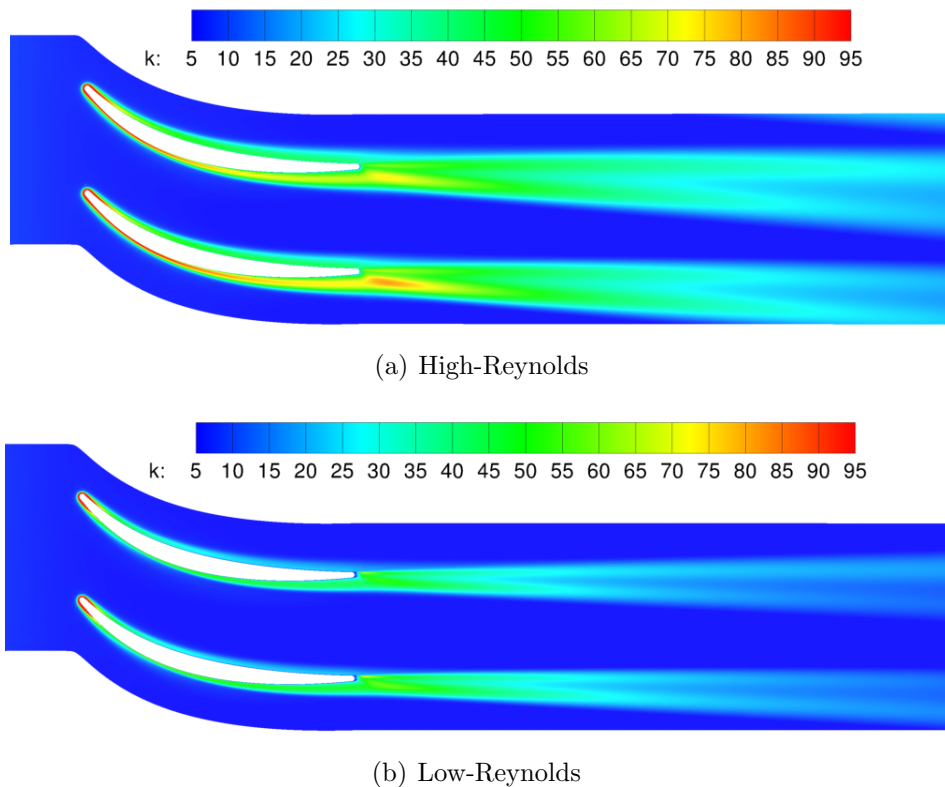
Figure 3.25: Contours of turbulent kinetic energy at the mid-height plane

Figure 3.25 presents an overall picture of the flow turbulence development over the vanes and the prediffuser via contours of turbulence energy, again for both high-Re and low-Re models. High turbulence is visible in the leading edge. Some of this will be due to 'false' generation of turbulence at impingement, which is not surprised in the eddy viscosity models used here. This subsequently grows in the OGV surface boundary layer particularly with the high Re turbulence closure, but much less so with the low Re model. There is a noticeable difference visible between the two OGVs due to the IGV effect, although in the turbulence field

this is much more noticeable with the high Re model. For the low Re model prediction, the high turbulence disappears very quickly on the vane leading edge, presumably because of high acceleration, relaminarising effects which the low Re model can pick up, unlike the high Re model. The turbulent OGV wakes are noticeably weaker and thiner with the low Re model; unfortunately no experimental data are available to indicate whether the low Re model changes are truly accurate. The pressure/suction surface boundary layers merge to form the OGV wake, which can perhaps be seen best in the turbulence energy field. A double-peaked contour shape in the near wake develops due to the turbulence generation at each edge of the wake/passage flow shear layer. This is stronger and occurs father downstream in the high Re prediction.

(a) High-Re   (b) Low-Re   (c) Measured data
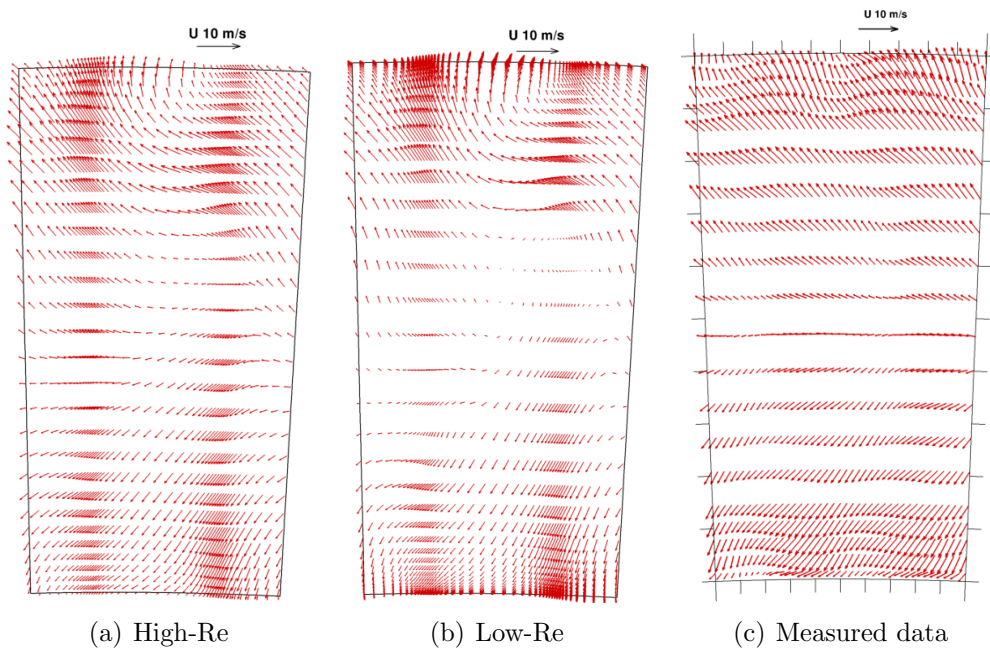
Figure 3.26: Secondary flow vectors at prediffuser exit

In the experiments of [9] the velocity field was measured in detail at pre-diffuser exit and this is compared to high Re and low Re RANS predictions in Figures 3.26, 3.27 and 3.28. Agreement is in general good although by no means perfect. Secondary velocity vectors at prediffuser exit illustrate the continued development through the prediffuser of the OGV created secondary velocity, and also

84

the effect of the divergence angle in the prediffuser which encourages the flow to divert outboard near the upper wall and inboard near the lower wall as exit is approached. The velocity vectors indicate that both turbulence models predict distinct regions of secondary flow vectors associated with each vane, whereas the measurements show a spanwise smoother, more merged picture.

(a) Circumferential variations   (b) Radial variations
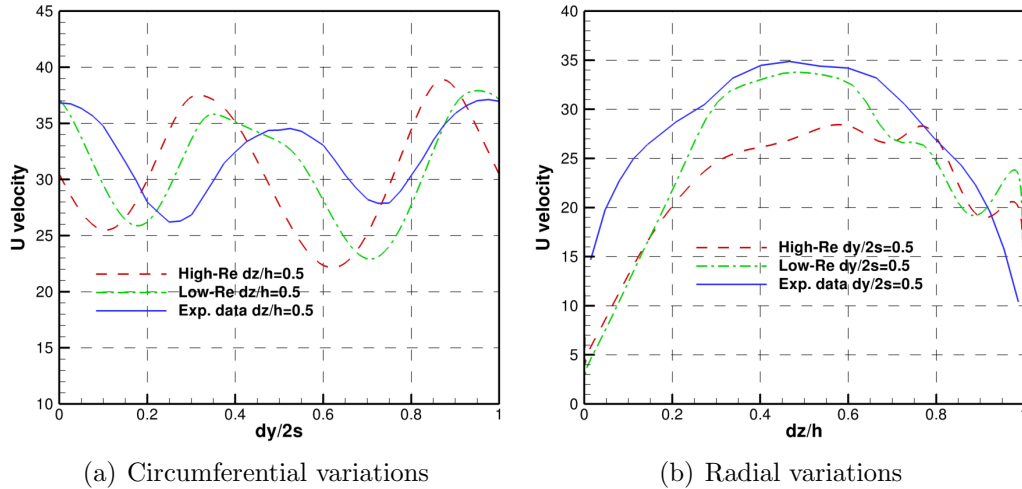
Figure 3.27: Axial velocity profiles at prediffuser exit

Although the flow has remained attached to both casings over the whole sector, strong circumferential variations in the flowfield are still clearly evident at prediffuser exit, see Figure 3.27a and 3.28. The 2D velocity and turbulence conditions provided by the upstream rotor and OGV row have enabled the low-energy flow adjacent to each casing to survive the pressure rise in the 1.6 area ratio prediffuser as can be seen in the axial velocity radial profiles in position dy/2s=0.5 Figure 3.27b (s indicates spanwise distance between the vane). The predicted near-end wall flow is in a worse state than observed in the measurements with both turbulence models with little difference in accuracy between the two models. Note that the different nature of the two high velocity regions associated with each OGV has been predicted correctly at least in trend terms compared to the measurements in that the right hand OGV (as seen in Figure 3.28) is associated with higher velocity than the left hand OGV.

(a) High-Re   (b) Low-Re   (c) Measured data
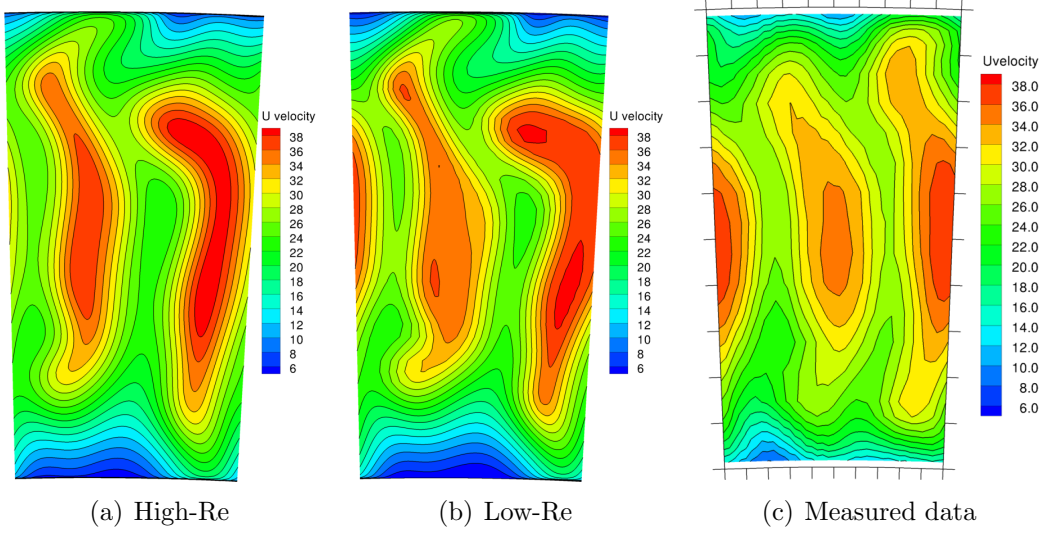
Figure 3.28: Axial velocity contours at prediffuser exit

3.2.5 Loss and Pressure Rise Performance

Finally, the high Re and low Re $k - \epsilon$ predictions of the overall performance of the OGV/prediffuser system are assessed against the mass-weighted static pressure recovery (C_p) and total pressure loss (λ) coefficients defined and measured in the experimental study [9]. The coefficients are defined as the increase in static pressure (mass-weighted over the sector area) (for C_p) and decrease in total pressure (mass-weighted) (for λ) and are normalised by a the reference inlet dynamic head. The definition of C_p and λ for flow change between two axial location '1' (upstream) and '2' (downstream) are calculated as follows:

$$C_p = \frac{\widetilde{p}_2 - \widetilde{p}_1}{(\widetilde{P} - \widetilde{p})}, \quad \lambda = \frac{\widetilde{P}_1 - \widetilde{P}_2}{(\widetilde{P} - \widetilde{p})} \tag{3.2}$$

Where

$$\widetilde{P} = \frac{1}{\dot{m}} \int_A \rho u P dA = \frac{1}{\dot{m}} \int_A \rho u (p + \rho \frac{1}{2} u^2) dA, \quad \widetilde{p} = \frac{1}{\dot{m}} \int_A p \rho u dA \tag{3.3}$$

A is the local cross-sectional area of the duct sector and $\dot{m}$ is the mass flow rate at any measurement plane defined as:

$$\dot{m} = \int_A \rho u dA$$

Three sets of coefficients are presented representing the flow change over the vane in isolation, over the prediffuser in isolation and overall, i.e. from OGV inlet to prediffuser exit. Table 3.1 shows that the high-Re model seemingly provides very good agreement for the overall performance, overpredicting loss but only by $\approx$ 0.8%, and underpredicting overall static pressure recovery by only $\approx$ 2%. This apparently very good agreement results, however, from a cancellation of errors – the vane loss (a large contribution) is predicted well (error -7.9%), but the prediffuser loss is overpredicted (+36% error); a similar behaviour is observed in the C_p breakdown, although not as dramatic. In contrast the low Re model results show a poor prediction of vane loss (-44%) and a better prediction of prediffuser loss (+6%), leading to an overall poor result for loss predictions (-35%).

Table 3.1: the OGV/prediffuser performance data

	C_{pV}	λ_V	C_{pd}	λ_d	C_p	λ
High-Reynolds	0.3467	0.1105	0.5509	0.0749	0.6457	0.1512
Low-Reynolds	0.4132	0.0669	0.5463	0.0584	0.6972	0.0973
Exp.	0.38	0.12	0.55	0.055	0.66	0.15

In summary therefore, considering the results presented for both velocity field development and overall performance prediction, the low Re model has not delivered any noticeable benefits. One possible explanation for this is that, although marginally better prediction for flow development from the low Re model could be seen, the low Re model is certainly not capturing correctly the physics of the flow over the OGV. There is some evidence that this might be because the flow over the OGV is very complex – signs of relaminarisation and return to fully turbulent boundary layer behaviour can be observed – and whilst the low Re model is capable of capturing the former process, whether it can capture the latter accurately is less certain. Compared with the low Re model, the high Re model might

be providing better results for the vane flow and overall loss because of some cancellation of errors – it certainly will not predict the relaminarising process and will treat the vane boundary layer as turbulent throughout. The prediffuser loss is however not well captured by the high Re model. In terms of a turbulence closure for CFD optimisation studies, the overall good performance of the high Re model is encouraging. Better turbulence modelling is however required as is shown from these results and the low Re RANS modelling has not improved the solution, so LES modelling should be investigated.

3.3   LES Results

3.3.1   LES Inlet Boundary Conditions – Background

Large Eddy Simulation (LES) is becoming more and more the method of choice for simulation of complex turbulent flows. This is particularly true if information on the dynamics of the large energetic flow structures is important, e.g. for highly anisotropic mixing or aeroacoustics application. Whilst high Re RANS, as reported above, has provided reasonably accurate predictions for the present flow problem, some questions as to modelling accuracy clearly remain, so it is important to investigate whether LES can provide improved accuracy, for example for the 3D wake mixing in the prediffuser adverse pressure gradient. However, as noted in the literature review in Chapter 1, a key challenge for LES is imposing physically meaningful unsteady 3D inlet conditions and the way this has been addressed is described next.

As noted earlier, and described in detail by Tabor and Baba-Ahmadi [115], there are basically two approaches to generate LES inlet conditions: library lookup (or precursor approach), in which a separate LES calculation of the inlet turbulent flow is performed, stored and mined to extract unsteady inlet conditions for the main LES calculation, and synthesis methods, in which target mean velocity data at inlet are supplemented by unsteady fluctuations with specific numerically manipulated turbulence characteristics, e.g. specified correlations (Gaussian), and

specified second moments [7][86][92].

The library lookup/precursor approach does not seem a viable option for the current flow problem as this would require a further LES calculation of the rotor stage at least. Given the availability of experimentally measured mean velocity and (some) turbulence information at rotor exit/OGV inlet, the synthetic turbulence approach is a better option and has been selected for use here. From the range of methods that have been proposed, a rescaling/recycling method (hereafter referred to as R^{2}M) is judged to be the most appropriate. This method, following the ideas of Lund, Wu and Squries [90] who applied it to boundary layer flows, has also been used in some flows with swirling by Pierce and Moin [82] and further modified for boundary layers by Xiao et al [93].

In general, these authors have so far only considered relatively simple geometries[90], or simple mean velocity profiles (only one or two components) [92][23]. For flows produced by rotating turbomachinery, where high spatial variations are present in all 3 dimensions as in the present case, further testing and modification was needed, as outlined in the following section.

3.3.2 LES Inlet Boundary Condition – R^{2}M – Implementation

There are essentially two variants of R^{2}M which have been used previously – the first involves only rescaling and recycling (following Xiao et al. [93]) and the second involves the use of source term forcing, Pierce and Moin [82][83]; both have been explored in the present work. Both variants require the creation of an extra Inlet Condition Domain (ICD) or R^{2}M domain (single or multi-block) upstream of the Main Computational Domain (MCD) inlet face, and LES calculations are run in both domains simultaneously making use of block-to-block coupling techniques to transfer information between ICD and MCD. Figure 3.29 shows the schematic diagram of the implementation of this two variants of R^{2}M. One difference in the current study is the implementation detail of the coupling

between the R^{2}M domain and the MCD. This is effected by ensuring a 'one-way transfer' – instantaneous velocities are transfered from the R^{2}M domain to the MCD inlet plane every time step but to make sure there is no feedback upstream from the MCD to the R^{2}M domain, the recycling plane is located a short distance upstream of the end of the R^{2}M domain. This is because in turbomachinery flow, the OGV vane row and its associated pressure field can have a relatively strong (potential) influence upstream, and this would interfere with the rescaling and recycling method in the R^{2}M domain.
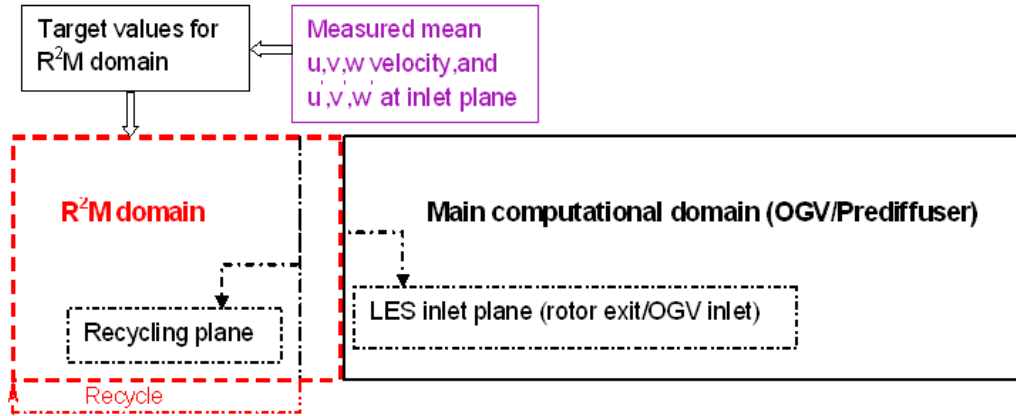
Figure 3.29: Schematic diagram of the implementation of R^{2}M

One final important aspect is the choice of the size of the R^{2}M domain. Clearly the size and the grid distribution (see later) in the radial and azimuthal directions (see Figures 3.30 and 3.31) are determined by the size/grid chosen in the MCD. For the axial size of the ICD, it is important that the length of the R^{2}M domain is great enough to allow unconstrained development of large scale resolved eddies in the axial direction. Of course the size of these turbulent eddies is not known a-priori, but an educated guess has to be made and subsequent checks will be carried out to make sure the chosen size is appropriate. These checks will be outlined later, and Figures 3.30 and 3.31 show that the axial length of the R^{2}M domain was chosen to be 1.1h (h = annular passage height).

Two methods of implementing the R^{2}M have been studied in the present work;

these are here referred to as Method A and B and are briefly outlined next.
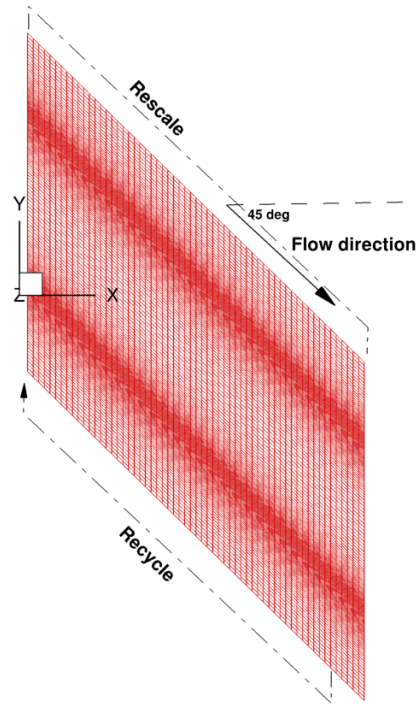
Figure 3.30: Mesh distribution across the R^{2}M domain
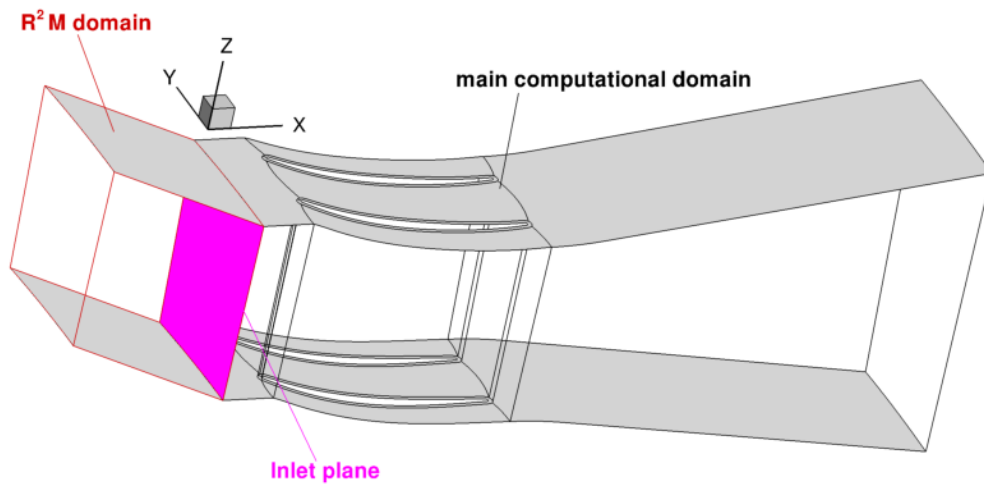
Figure 3.31: Connection between the R^{2}M domain and the main computational domain

Method A.

Method A is a modified version of the Xiao et al. [93] approach. The version described by Xiao et al.[93] was applied to a 2D wall boundary layer flow with only 1D (i.e. wall normal (z) varying only) mean velocity and normal stress (rms) levels supplied as input. The result was shown to perform as well as the original boundary layer-specific transformation method of Spalart ([88]) and Lund et al. [90]. In the present study, it is extended and used for the more complex OGV application. In this case, the mean velocity profiles depend on both spanwise and transverse co-ordinates (y and z). As shown in the RANS predictions prescribed above, information on all 3 mean velocity components is available from experiments [9] at the selected OGV inlet plane. Unfortunately turbulence information is only available in the form of just a single radial traverse. Since method A (and also B) requires information on all 3 normal stress (or rms) levels, the following simplified assumption had to be made to provide the required complete 'target' data:

(i) the single radial (z) profile was assumed to apply unchanged in the y direction.

(ii) the 3 normal stress components (adding up to the total turbulence energy k) were assumed to be in the ratio (1:1:0.5).

Of course this assumption does not match the turbulence to the strong y (azimuthal direction) mean velocity gradients, but this is very difficult to address without measured turbulence in the y direction and this simplification was accepted at this stage of testing.

In method A (and method B), the instantaneous fields within the R^{2}M and Main domains were initialised by superimposing white noise with an intensity matching the 'target' rms levels onto 'target' mean values of the measured 3 mean velocity components over the entire R^{2}M domain. The target mean velocity $\overline{u}_{i,target}(y,z)$ and rms fluctuation $u'_{i,target}(y,z)(i=1,2,3)$ data represent the statistical data extracted from measurements at rotor exit/OGV inlet (used as 2D inlet conditions for RANS) and interpolated for each grid node on the inlet plane as described

earlier.

An LES calculation was then run within the R^{2}M domain in which the flow field everywhere within the R^{2}M domain was rescaled every k time steps in the following way.

Firstly, the mean velocity components ($\overline{u}_i$) predicted by the LES were evaluated from a weighted sum of spatial averaging in the streamwise (assumed homogeneous) direction and time-averaging, with a weighting that decreased exponentially backward in time:

$$\overline{u}_i^{n+1}(y,z) = \frac{k\Delta t}{T} \langle u_i(x,y,z,t)\rangle_x + (1 - \frac{k\Delta t}{T})\overline{u}_i^n(y,z) \qquad (3.4)$$

Where Δt is the LES computational time step, T is an estimated characteristic time scale of the flow ($T = \alpha h/\overline{u}_\infty$ was used), $\langle\rangle_x$ represents a spatial average in the streamwise direction, and $u_i(x,y,z,t)$ is the current instantaneous LES velocity solution. superscript n indicates the estimated mean velocity from the previous (k-1) time mean value calculation.

The rms level of each velocity component is calculated similarly.

$$u_i^{'(n+1)}(y,z) = \sqrt{\frac{k\Delta t}{T} \langle [u_i(x,y,z,t) - \overline{u}_i^{n+1}(y,z)]^2\rangle_x + (1 - \frac{k\Delta t}{T})[u_i^{'(n)}(y,z)]^2}$$

$$(3.5)$$

Secondly, the current instantaneous velocity field ($u_i(x,y,z,t)$) was re-scaled to create a new instantaneous velocity in each grid plane within the ICD:

$$u_i^{new}(x,y,z,t) = \frac{u_{i,target}^{'}(y,z)}{u_i^{'(n+1)}(y,z)}[u_i(x,y,z,t) - \overline{u}_i^{n+1}(y,z)] + \overline{u}_{i,target}(y,z) \qquad (3.6)$$

Finally, the instantaneous field on the chosen recycling plane just upstream of the end of the R^{2}M block (see Figure 3.30) is transferred to the inlet plane of the R^{2}M block.

Method B.

Method B follows in part the approach to R²M taken by Pierce and Moin's[82] who introduced a body force to generate swirling flow in a periodic domain, with virtual axial and azimuthal body forces added to the LES momentum equations. Method B used here is similar but with two differences. As in method A, the LES in the R²M domain is run simultaneously with the LES calculation in the main domain rather than in separate computations as in Pierce and Moin's[82] implementation. Further, in Pierce and Moin's method, the body forces were introduced into only 2 momentum equations (axial and azimuthal) and were simple algebraic functions (either constant, linear or quadratic) of the radial location. For the current cases, all three velocity components must be considered. An artificial body force was added to all three momentum equations (in the R²M domain only), as shown below (here an overbar indicates spatially filtered variables):

$$\rho\frac{\partial \overline{u}_i}{\partial t} + \rho\frac{\partial \left(\overline{u}_i \overline{u}_j \right)}{\partial x_j} = -\frac{\partial \overline{P}}{\partial x_i} + \mu\frac{\partial^2 \overline{u}_i}{\partial x_j \partial x_j} - \frac{\partial \tau_{ij}}{\partial x_j} + F \tag{3.7}$$

with

$$F = \frac{\partial \overline{P}}{\partial x_i}$$

The forcing term F is adjusted to be equal and opposite to the pressure gradient term in the momentum equations; it is thus used to eliminate the pressure gradient term influence from the velocity field. The consequence is that the rescaling technique itself (which is retained in method B as well as the Pierce and Moin [82] implementation) is left to "force" the velocity field.

3.3.3   Testing of Alternative R²M Methods

Both R²M techniques proposed for study here require an extra R²M domain to be generated upstream of the inlet plane of the MCD, as shown in Figure 3.31. The inflow conditions to the R²M domain inlet in both methods are generated by recycling the velocity field from one chosen plane in the downstream region of the R²M domain, as shown in Figure 3.30. The instantaneous flow field rescaling

within the R²M block described above guarantees that the flow will be approximately statistically homogeneous in the streamwise direction. As commented above, the streamwise size of the R²M block should be selected so that the two-point correlations in the streamwise direction should fall to zero well within the R²M domain (say within half the streamwise size), as required by the recycling technique. The length of the R²M block in the streamwise direction was thus selected as approximately twice the integral length scale; this was estimated (from the RANS calculation) to have a value of 0.015m, thus the axial length of the R²M domain was set at 0.03m. Since the inlet of the OGV/prediffuser flow has a 45 deg swirl component provided by the rotor, the R²M block is of course best aligned appropriately with the main computational domain (Figure 3.30) for proper application of the periodic conditions on the side boundaries.

Since in the current case the coupling between the R²M domain and the MCD is via a 'one-way transfer', the investigation of the two alternative R²M techniques can be carried out only within the R²M domain. Periodic conditions and a convective outflow boundary condition were adopted respectively on the spanwise and outlet boundaries. The R²M domain takes the form of a straight channel upstream of the inlet face of the MCD and has the same cross-section node distribution as the inlet of the MCD as shown in Figure 3.30. The mesh is uniform in the streamwise direction as has been found necessary for the recycling technique (Xiao et al. [93]). The mesh resolution in the R²M domain is $60 \times 174 \times 121(N_x \times N_y \times N_z)$ cells, with the first near wall layer of cells at approximately $x_n^+ \approx 2$ and grid spacings in the streamwise and azimuthal directions $\Delta x_s^+ \approx 80$, $\Delta x_t^+ \approx 20$ (s, n, t indicate streamwise, normal and spanwise to the wall respectively). In the current case, rescaling is carried out every time step.

Figures 3.32 and 3.33 compare radial profiles of time-averaged and circumferentially averaged mean velocity components and rms values of the 3 normal stresses at locations $\Delta x/L = 0.25, 0.5, 1.0$ within the R²M domain, where L represents the domain length. The results from both methods A and B are compared to experimentally measured target radial profiles at rotor exit/OGV inlet (taken from Figures 3.2 and 3.4). The solid line represents the target values, whilst the

(a) $\Delta x/L=0.25$

(b) $\Delta x/L=0.5$

(c) $\Delta x/L=1.0$
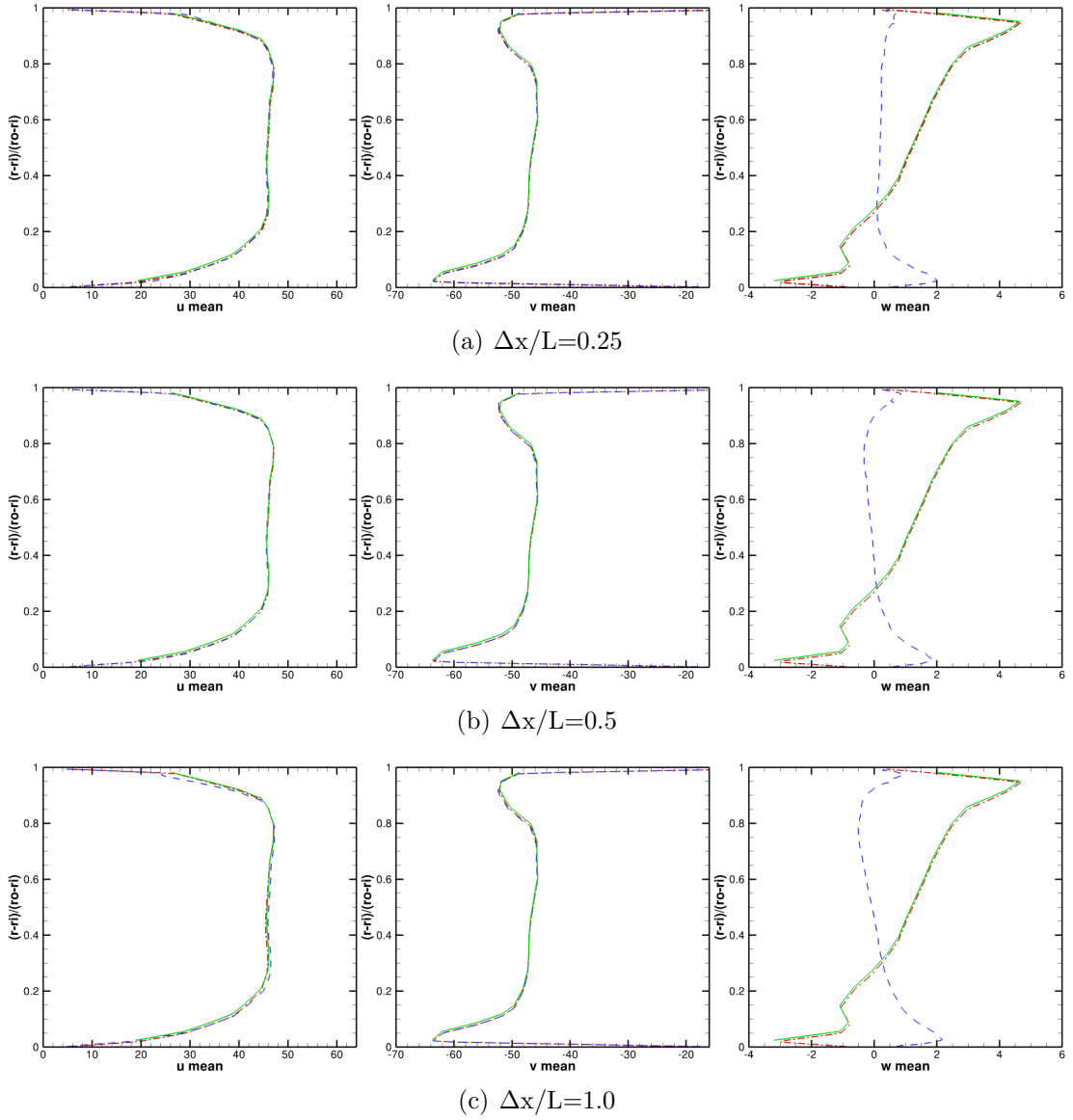
Figure 3.32: Time-averaged and circumferentially averaged profiles of mean velocity at different distances within the R²M block provided by Method A and Method B. Solid line-Target value, dashed line-Method A, dashdot line-Method B

(a) Δx/L=0.25

(b) Δx/L=0.5

(c) Δx/L=1.0
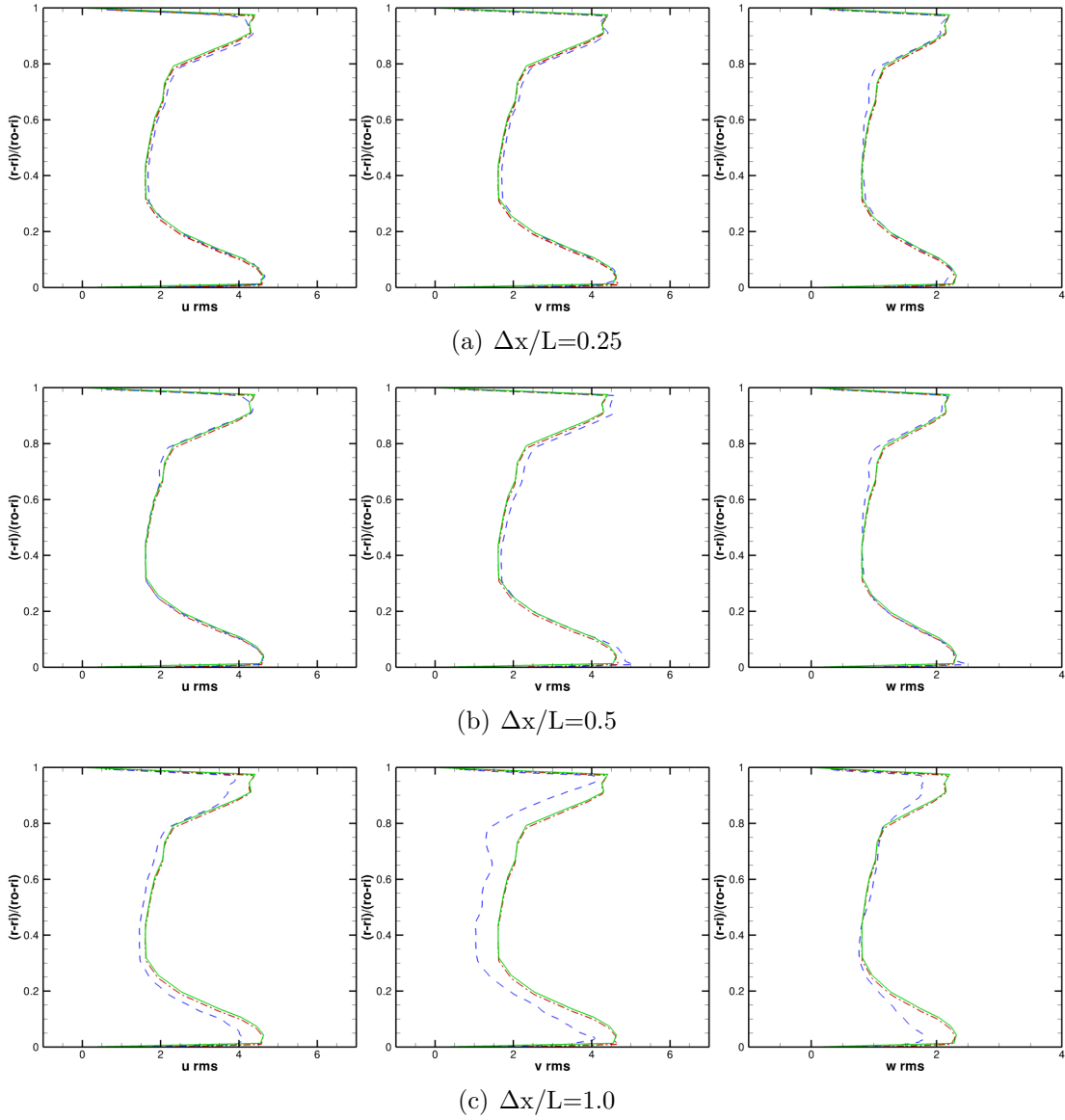
Figure 3.33: Time-averaged and circumferentially averaged profiles of rms at different distances within the R^{2}M block provided by Method A and Method B. Solid line-Target value, dashed line-Method A, dashdot line-Method B

dashed and dash-dot lines refer to results provided from method A and method B. These figures show that method B produces very accurate results for both mean and rms profiles. Although method A provided good results for mean axial and circumferential velocities, the small radial velocity produced did not fit the target data at all. In addition, the rms components from method A, though quite close to the target values, were not as accurate as with method B. The explanation for the improved performance of method B over method A is that the constant re-scaling of the velocity field is sufficient to establish the nett mean flow momentum in the axial and swirl directions, there is no need for a finite pressure gradient in x and y directions to drive the flow. Whilst in method A the static pressure gradients are small, the 'noise' in these essentially zero pressure gradients is sufficient to drive the small radial velocity away from the target profiles. It can also be clearly seen in Figures 3.32 and 3.33 that (with method B) an essentially streamwise homogeneous turbulent flow is created by the R^{2}M technique, since the profiles of both statistical mean and turbulence qualities are independent of $\Delta x/L$.

Figure 3.34 shows well how method B was able to produce accurate distributions of all three mean velocity components in both spanwise and radial directions compared to the input target values. Although the circumferentially averaged mean velocity predictions from method A (especially u,v components) are as good as method B (Figure 3.32), the 2D assessment (Figure 3.34 spanwise and radial directions) shows that method A is still not as accurate as method B when assessed against target measured data. The normal Reynolds stresses produced by method A were also influenced by the the inlet and outlet boundaries in the method A R^{2}M block as can be seen in Figure 3.35, whereas the method B solution showed excellent streamwise homogeneity. Accordingly, method B was the chosen R^{2}M technique for all further predictions.

To check that the axial extent of the R^{2}M domain had been correctly chosen, two-point spatial correlation coefficients were evaluated from the LES solution within the R^{2}M block. The normalised two-point correlation coefficient (at a location x_{ref}) $R_{11}/u'^2 = \overline{u_1(x_{ref}+dx)u_1(x_{ref})}/\overline{u_1^2(x_{ref})}$ (i.e. the longitudinal

(a) Method A

(b) Method B
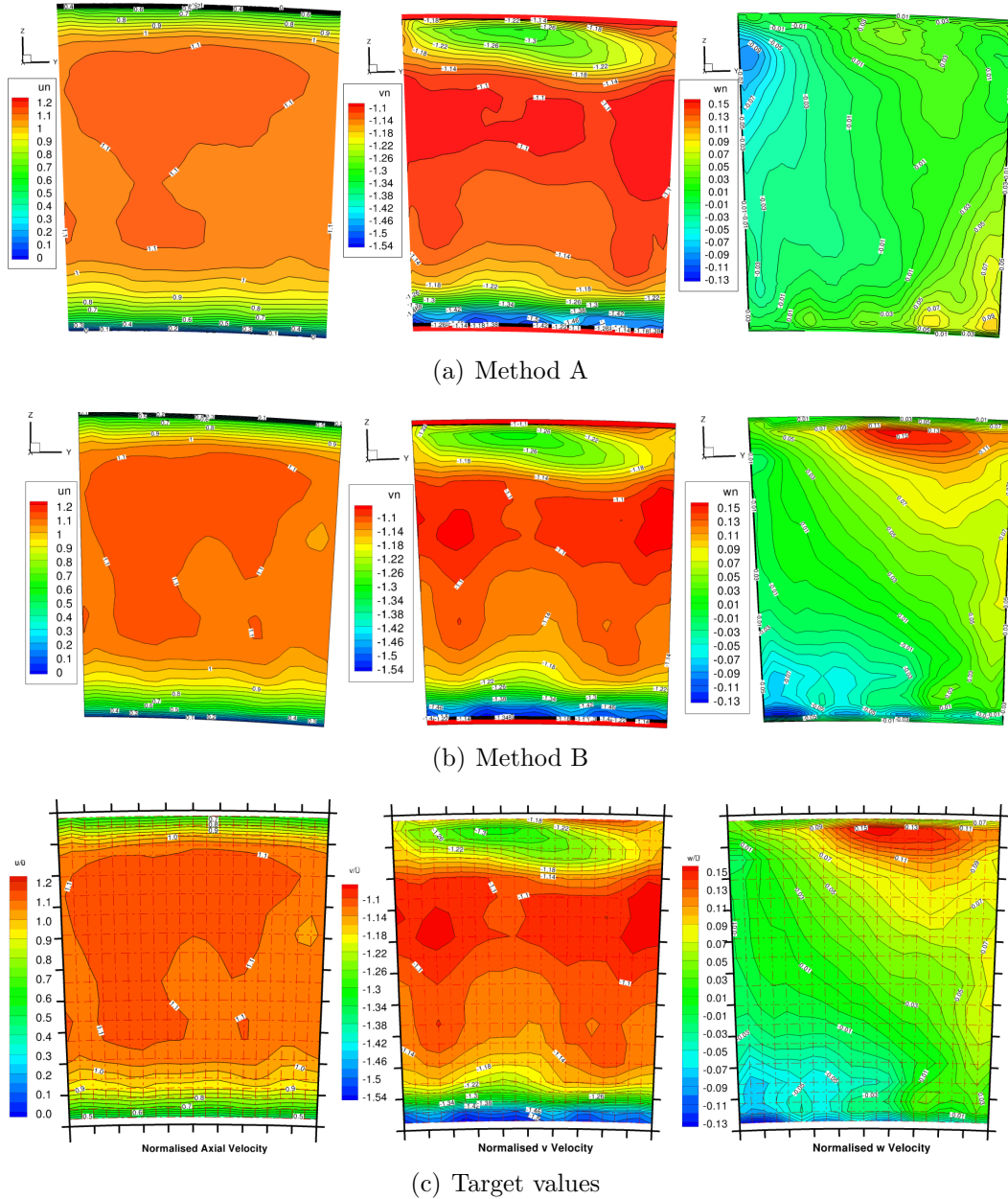
(c) Target values

Figure 3.34: Contours of mean values provided by Methods A and B, compared to target values

(a) Method A   (b) Method B
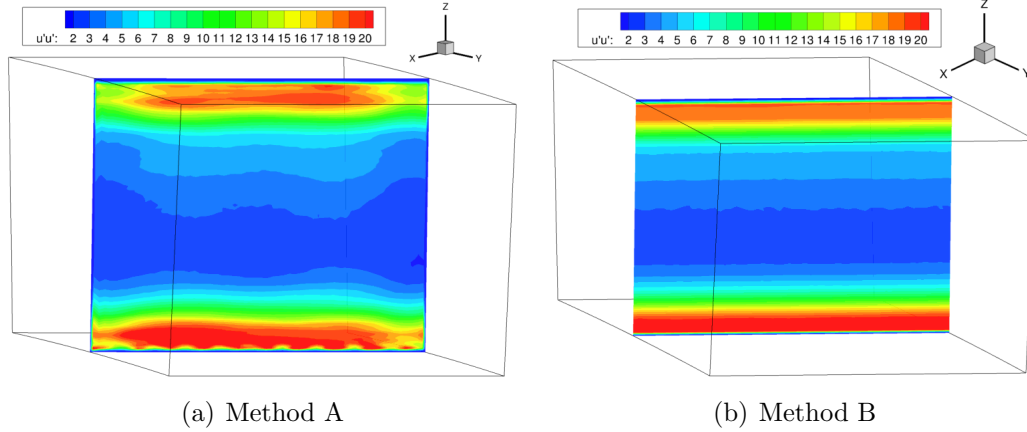
Figure 3.35: Contours of axial normal Reynolds stress ($\overline{uu}$) along the R^{2}M block in the streamwise direction

autocorrelation function [12]) for the axial velocity was calculated. Figure 3.36 shows the correlation coefficient from method B with the reference point located at $d/h = 0.05, 0.1, 0.5$ (d indicates the distance from the inner wall and h represents the radial height of the R^{2}M domain), and increasing axial separation (dx) between the two points. Note how for all 3 points the coefficient falls to zero well within the R^{2}M domain before it rises again (as it must as the recycling plane is approached). Note also that the implied integral scale (zero crossing of the correlation) is small for points near the wall but becomes much larger in the central of the flow.

Finally, time series data were extracted for various locations along the R^{2}M domain centreline and Fast Fourier transforms evaluated to generate spectral information. Figure 3.37 shows the energy spectrum predicted by method B at the centre of the R^{2}M domain exit plane. The spectral shape is as expected, there is some evidence of energetic nearly-periodic motions at 10^2 or 10^3 frequencies in the large scale energy containing region of the spectrum (perhaps due to some vortex shedding type process), an inertial $-5/3$ power law region is also apparent followed by a rapid cut-off at higher frequencies. It was considered that the tests and checks were sufficient to demonstrate the adequacy of the R^{2}M technique and attention was this turned to using this to produce LES solution of the
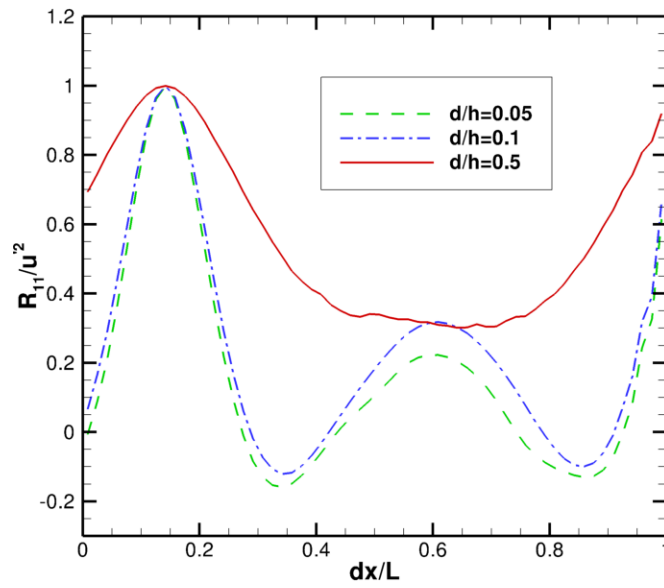
Figure 3.36: Two point spatial correlation within the R^{2}M block, method B

OGV/prediffuser.
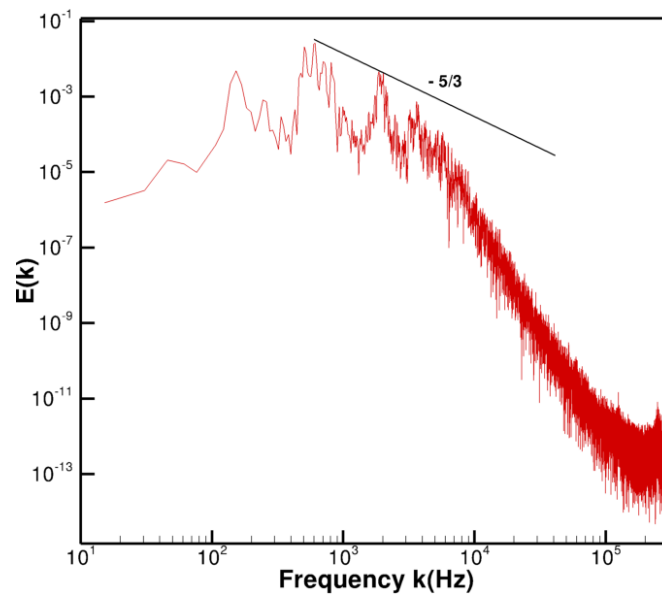
Figure 3.37: Energy spectrum generated from time series data at the centre of the R^{2}M block exit plane, method B

3.3.4   LES Main Computational Domain Grid Details

In order to resolve the near-wall energetic motions, LES requires fine grids near walls. In practice, as recommended by Sagaut[17] this is achieved by placing the first cell in the zone $y^+ < 1.0$ and controlling the finite volume cell size in the near wall mesh. There have been numerous studies on the resolution required for capturing turbulence production mechanisms in the near-wall region. Zang[116] has proposed adequate resolution requires $\Delta x_s^+ \approx 80, \Delta x_t^+ \approx 30$ while Piomelli and Balaras[6] have recommended $\Delta x_s^+ \approx 100, \Delta x_t^+ \approx 20$, with the first grid-point off the wall at $x_n^+ \approx 2$ (wall units are defined as $x_i^+ = x_i u_\tau / \upsilon$ and s, n, t indicate streamwise, normal and spanwise to the wall respectively). In the present study, the mesh resolution for the main computational domain remained the same for all LES calculations. The number of mesh points for LES calculations is almost the same as for the low-Re RANS prediction, only with a slightly coarser mesh close to the wall and a more uniform mesh distribution in the wall normal (radial) direction. The mesh resolution for the LES simulations are (estimated by using the high Re RANS predictions):

i) For the vane 'O' mesh, the grid spacings in the streamwise and spanwise directions were $\Delta x_s^+ \approx 25, \Delta x_t^+ \approx 40$, the first grid-point away from the wall was at $x_n^+ \approx 1$.

ii) For the prediffuser 'H' mesh, the grid spacings in the streamwise and azimuthal directions were $\Delta x_s^+ \approx 100$, $\Delta x_t^+ \approx 20$ in non wake region and $\Delta x_t^+ \approx 8$ in the wake mixing region, the first grid-point away from the wall was at $x_n^+ \approx 5$.

3.3.5   LES Results

Using the R^{2}M (method B) approach and the mesh as described above, the DELTA flow solver was run in LES mode for the OGV/prediffuser problem. The LES calculations were run with a constant time step of 1×10^{-6}secs (CFL≈0.6). A total of 8 flow-through times (≈30000 timesteps, the flow through time is defined by the computational domain length divided by the averaged OGV inlet axial velocity) was performed for LES initial flow development (to give the unsteady

flow time to "forget" the start-up field values) and another 10 flow-through times (≈40000 timesteps) was performed for statistical sampling. An LES calculation using a simple white noise perturbation (10% of mean velocity) superimposed on the inlet mean velocity contours was also carried out for comparison purposes.

To illustrate the unsteady flow characteristics of these simulations and to provide evidence of the turbulent structures captured, the second invariant of the velocity gradient tensor (the Q criterion proposed by Hunt et al [117]) was used:

$$Q = -\frac{1}{2}(S_{ij}S_{ij} - \Omega_{ij}\Omega_{ij}) \tag{3.8}$$

where S_{ij} and Ω_{ij} are, respectively, the strain-rate and rotation tensor. In other words, Q is the balance between the magnitude of the strain rate $S^2 = S_{ij}S_{ij}$ and the magnitude of the rotation rate $\Omega^2 = \Omega_{ij}\Omega_{ij}$; The implication of the latter observation is fairly straightforward: positive Q isosurfaces isolate areas where the strength of rotation overcomes the strain, thus making those surfaces eligible for identification as contours of local vortices [118].

Figure 3.38 shows isocontours of the Q-criterion at the mid-annulus height section of the whole OGV/prediffuser geometry for both white noise and R^{2}M inlet condition LES simulations. The value of Q=3 was chosen to show the large scale turbulent structures most clearly. Note that three-dimensional and much larger scale turbulent structure can be clearly observed in the inlet flow generated by the R^{2}M approach, whilst the white noise method similarly shows very small and uncorrelated structures that disappear very quickly (already gone by the time the inlet flow reaches the OGV leading edge). Interestingly, even the R^{2}M generated turbulence disappears further downstream. At least the turbulence next to the vane surface disappears, some larger structures in the core of the passage flow are still identifiable over the whole vane chord length. The most likely explanation for this (also noticed above in discussing the low Re RANS results) is that it is due to the strong acceleration over the OGV aerofoils. Turbulence reappears in both cases further down the vane surface (it re-appears earlier in the R^{2}M solution) and the highly turbulent wakes passing through the prediffuser are clearly seen.
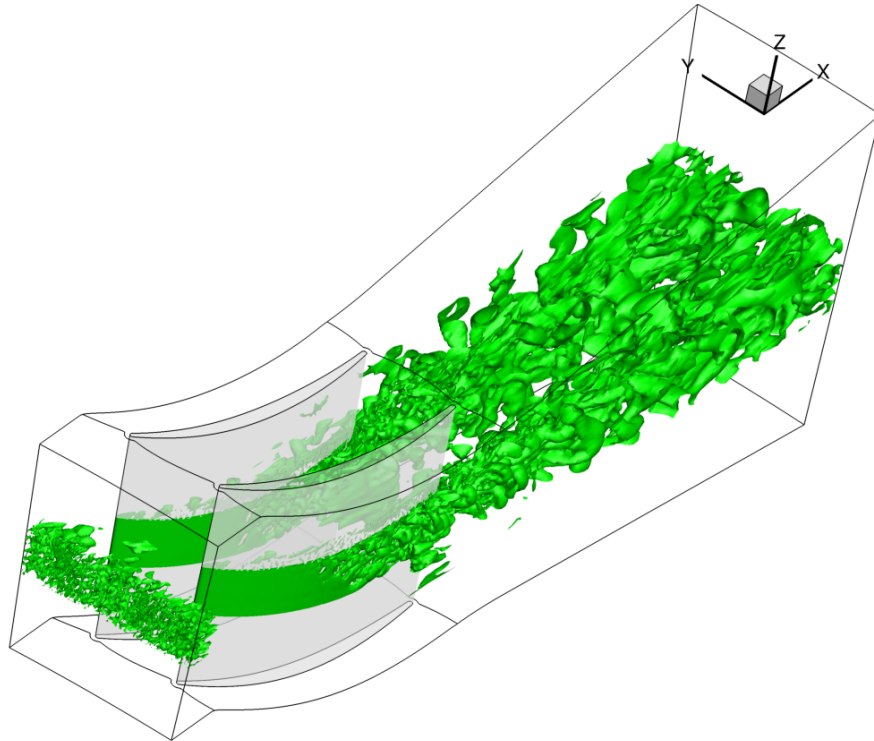
(a) white noise
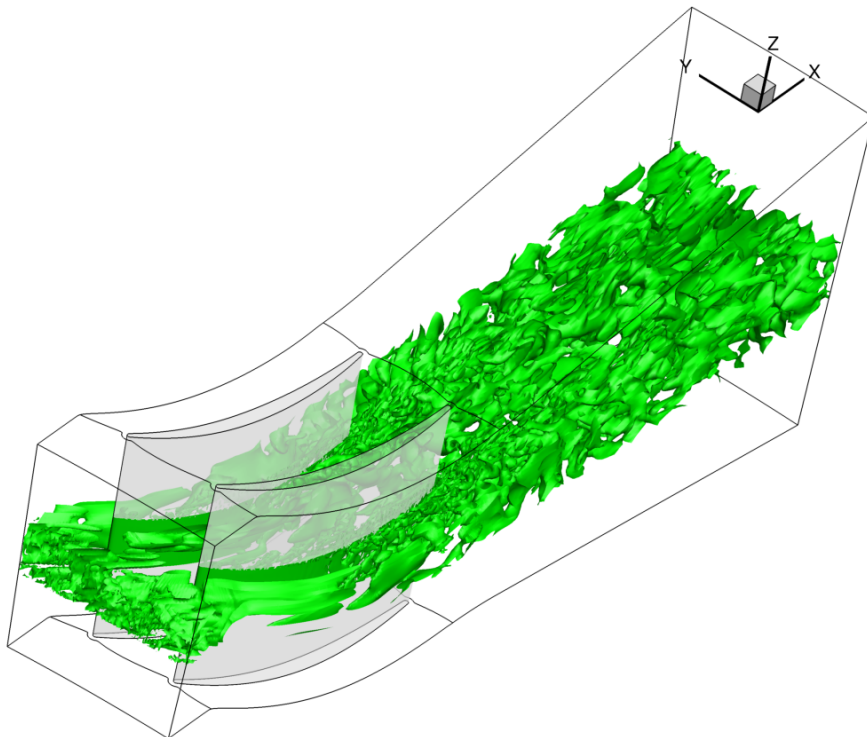
(b) R²M

Figure 3.38: Isocontours of Q=3 at mid-annulus height of the OGV/prediffuser assembly.

Differences in white noise and R^{2}M solutions can be seen in the wake – the white noise structures are larger and fewer in number than the R^{2}M picture, although the differences are perhaps less than in the inlet flow. This picture illustrates the extremely complex challenge presented for the turbulence modelling of this flow. Given the numerical challenge outlined in Chapter 1 concerning the required LES spatial resolution for near-wall flow, Figure 3.38 raises questions on the adequacy both of the current mesh in the region of the forward part of the OGV, and also the ability of the current simple SGS model to predict accurately the relaminarisation and re-appearance of turbulence processes.

Figure 3.39 and Figure 3.40 present contour plots of instantaneous vorticity magnitude developed in the OGV/prediffuser flow for both white noise and R^{2}M inlet conditions. Two radial planes in the streamwise direction are shown, one across the middle of the vane passage (Figure 3.39) and the other near the suction side of the OGV ($dy/s = 6\%$ Figure 3.40). It can be noted from these figures that the white noise imposed in the inlet flow decays almost instantaneously, whereas in contrast, the R^{2}M approach generates inlet eddy structures which are just about visible throughout the flow, surviving best in the endwall boundary layers. Unsteadiness and disturbance particularly near the outer wall of the blades was captured in the predictions as can be seen in Figure 3.40.

Figures 3.41 and 3.42 present Reynolds axial normal stress and Reynolds shear stress ($\overline{uv}$) predictions separately on a mid-annulus height plane. It is noticeable that solutions using both inlet condition methods indicate a strong generation of turbulence starting approximately half way along the blade. Close inspection of the predictions show that this is associated with the prediction of a very thin separated flow zone as shown in the zoom-in view on the vane suction side mean axial velocity field in Figure 3.43. Whether such a zone exists in the experiment is not known (although unlikely), but the complex laminarisation and subsequent transition to a turbulent boundary layer on the suction side surface are extreme modelling challenges as noted above. The size of the separated region is noticeably reduced in the R^{2}M prediction, which is thus believed to be an improvement on the white noise approach.
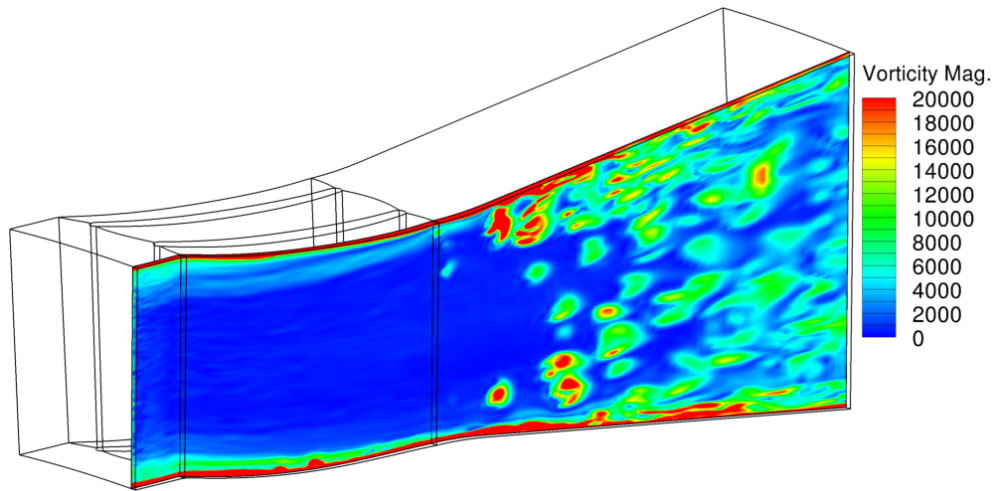
(a) white noise
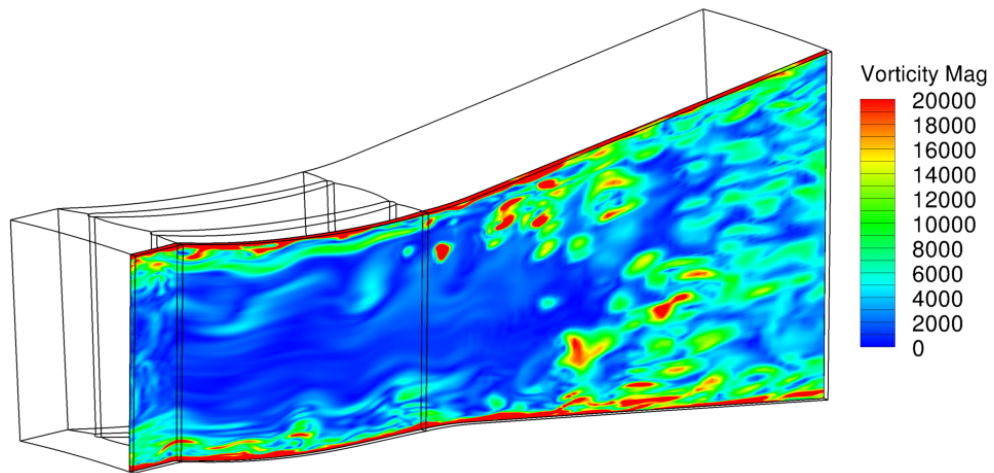
(b) R²M

Figure 3.39: Contours of vorticity magnitude on mid-passage radial plane
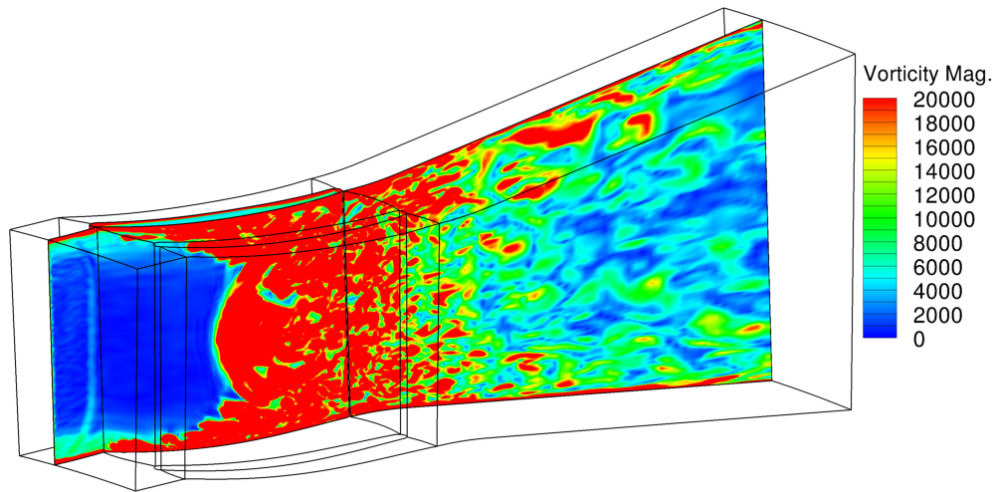
(a) white noise
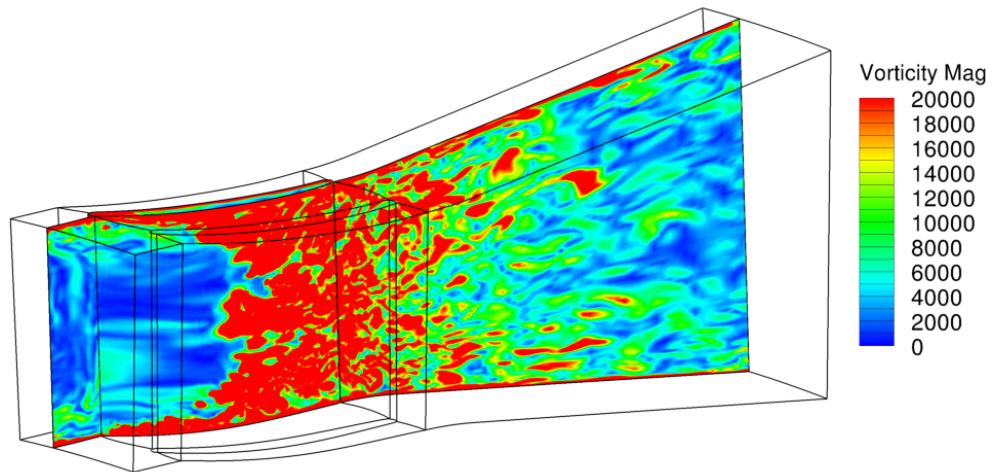
(b) R^{2}M

Figure 3.40: Contours of vorticity magnitude near vane suction surface (dy/s=6%)
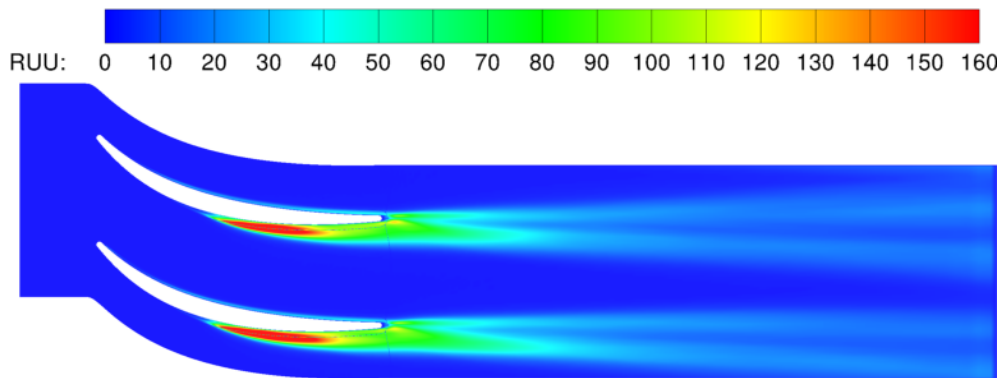
(a) white noise
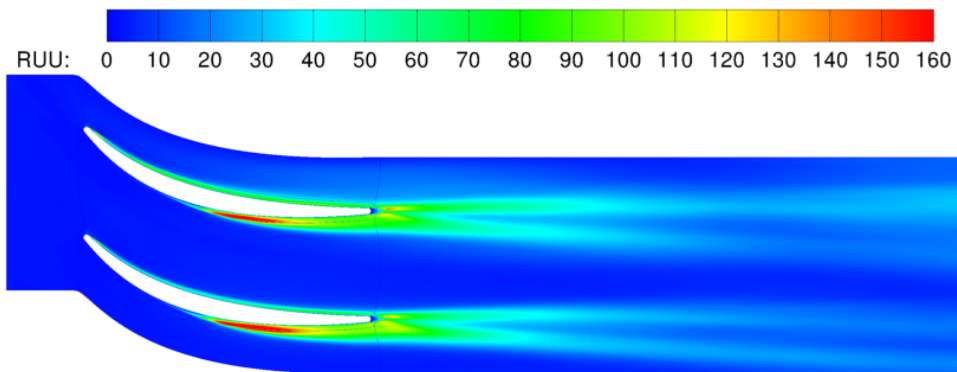
(b) R²M

Figure 3.41: Contours of Reynolds axial normal stress on a mid-annulus height plane
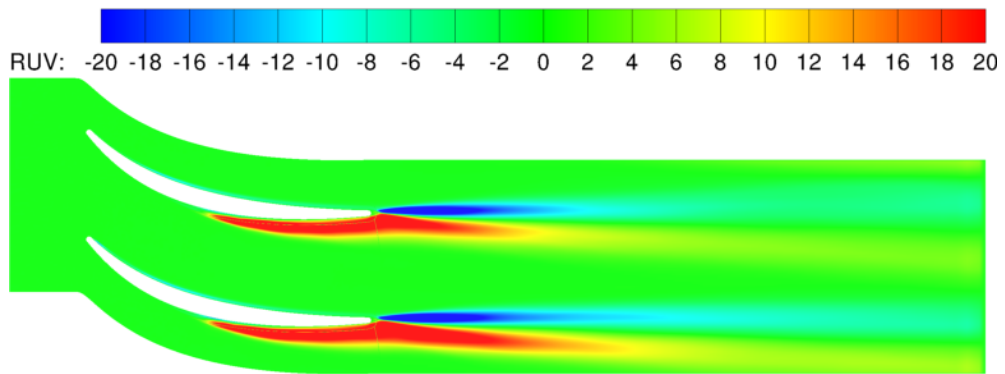
(a) white noise
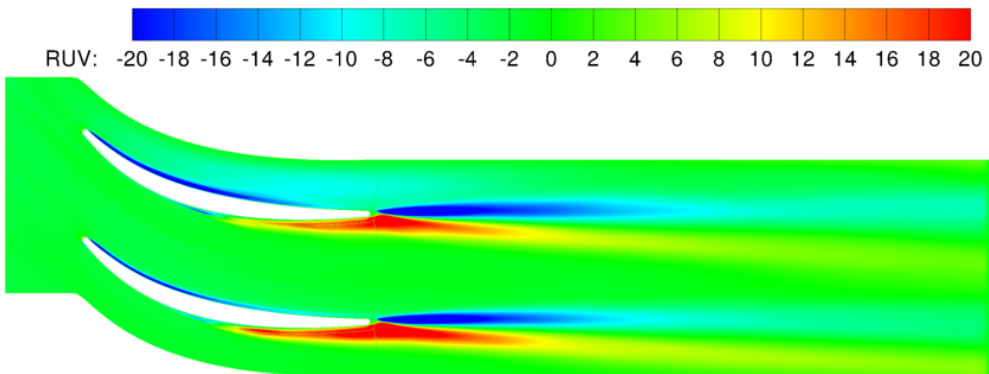
(b) R²M

Figure 3.42: Contours of Reynolds $\overline{uv}$ shear stress on a mid-annulus height plane

(a) white noise

(b) R^{2}M
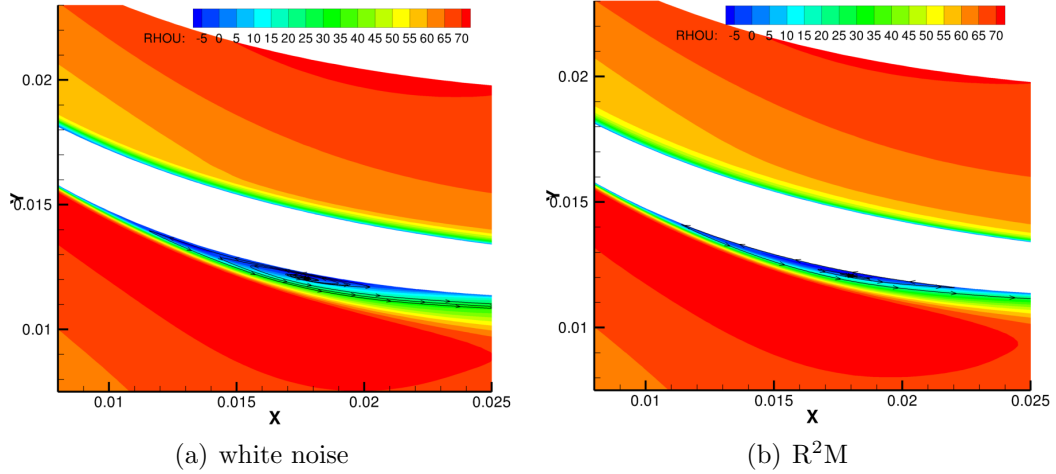
Figure 3.43: Separation zone predicted on the vane suction surface at the mid-annulus height plane

Figure 3.44 shows the Q-criterion coloured by instantaneous axial velocity. A rapid destabilisation into three-dimensional structures can be observed. It displays indications of leading edge horseshoe vortices near the vane tip in Figure 3.45a, trailing edge vortices, and a high turbulent zone beginning from the vane mid-chord and extending down the prediffuser as shown in the zoomed-in views in Figure 3.45b.

Contours of instantaneous axial and radial velocity of the OGV/prediffuser flow field are presented in Figure 3.46. The unsteadiness in the wake and the two very high gradient shear layers created by the vane, one on the suction side and one on the pressure side, can be easily identified. These merge at the trailing edge or OGV exit. It can be seen that the refined LES mesh is needed to resolve as much of the large scale motion as possible, since this is responsible for turbulence production. Clearly differences between the two wakes also can be identified particularly in the instantaneous radial velocity field on the mid-annulus plane, where a majority of negative w values (towards the inner wall) are found in the upper vane and positive values (towards the outer wall) in the lower vane. In all probability this difference is due to the influence of the inlet flow IGV effects.
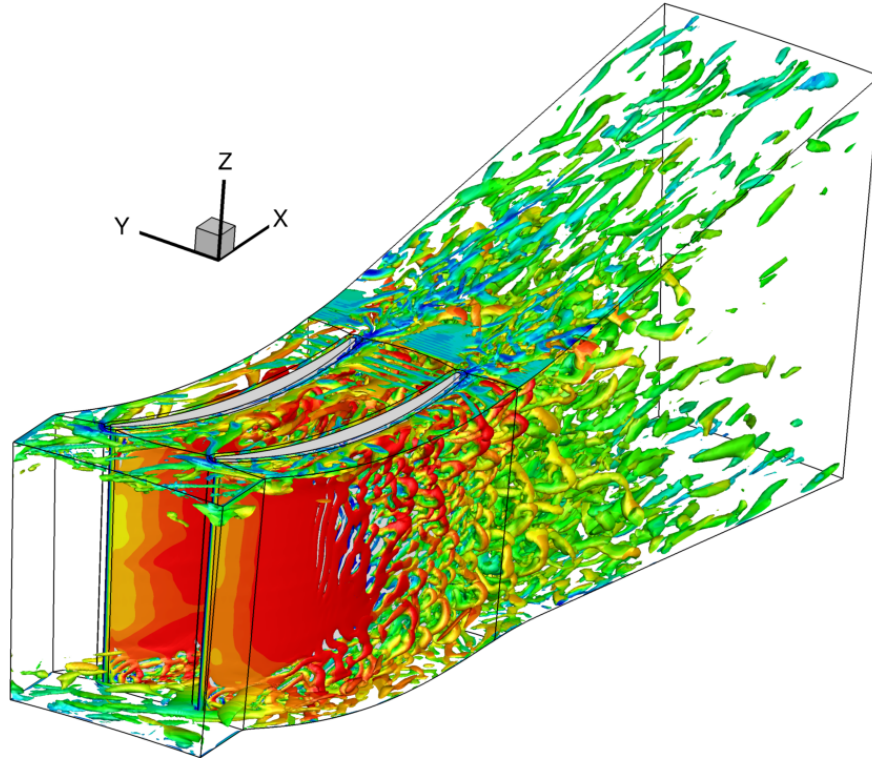
Figure 3.44: $Q = 2 \times 10^7 (\frac{1}{2}(\Omega^2 - S^2))$ coloured by instantaneous axial velocity
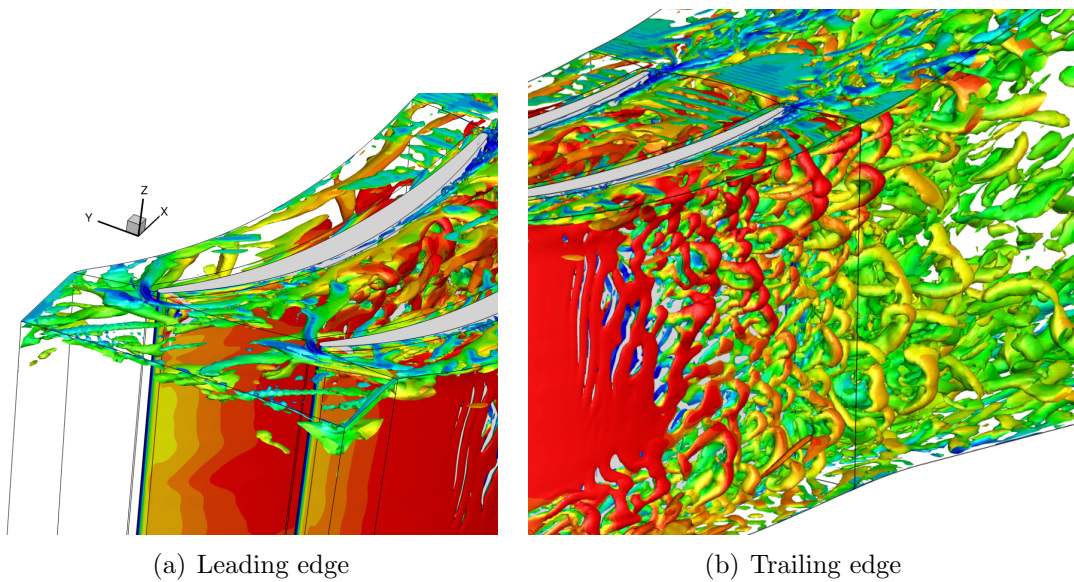
(a) Leading edge

(b) Trailing edge

Figure 3.45: Zoom-in views of the Q criterion
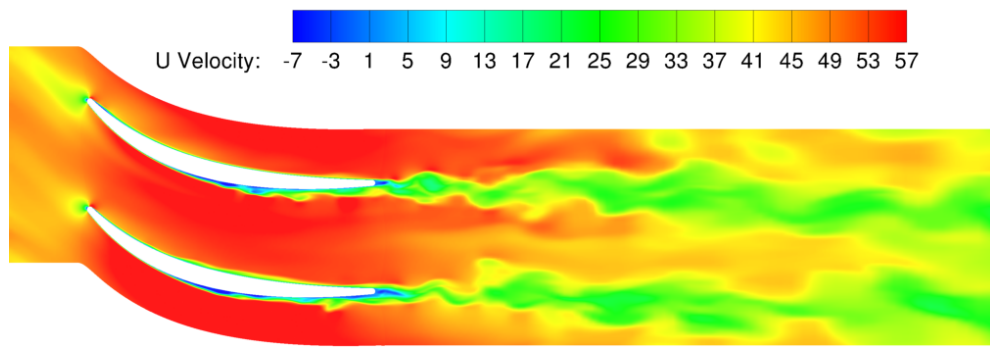
(a)
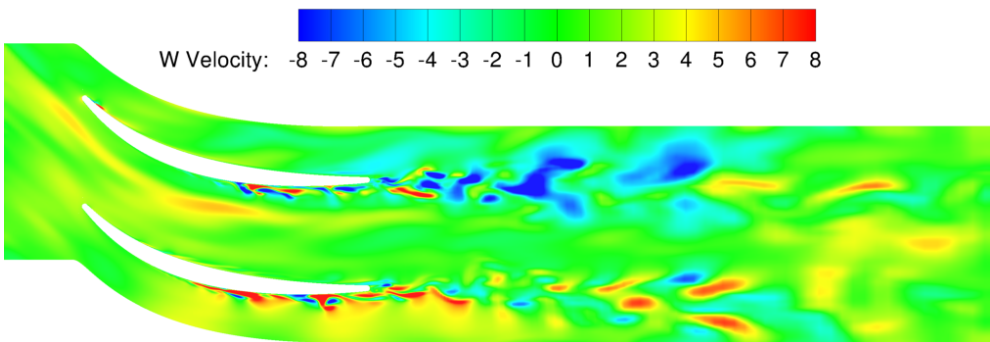
(b)

Figure 3.46: Contours of instantaneous axial velocity and radial velocity

Figure 3.47 shows the high-Re $k - \epsilon$ and LES R^{2}M solutions for the 3 mean velocity components compared against experimental data measured at OGV exit. Indications are visible again of a thin recirculation zone in the wake at the OGV trailing edge in both RANS and LES solutions. There is some evidence that this contains stronger backflow in the LES compared to the RANS solution, presumably because of the separation predicted on the vane suction surface. Both CFD solutions seem to overpredict wake thickness compared to the measured data with the LES solution here showing the smaller error. In the region of the outer wall suction surface corner the strong secondary flows are visible, with low energy fluid being swept away along the suction surface of the blade. This low energy is likely to be associated with the outer wall boundary layer which is better predicted by the high-Re RANS model in terms of boundary layer thickness (perhaps showing the weakness of the van Driest damping in the LES SGS model). The trends in all 3 velocity components match the experimental data, with the overall wake thickness and shape reasonably well captured.

Figure 3.48 shows a comparison between CFD (both high Re RANS and LES) predictions and measurements for mean axial velocity at prediffuser exit. Once again a good trend prediction is evident; both RANS and LES predictions at prediffuser exit capture the main features shown in the measured data such as the IGV influence on the two different high velocity regions. The near-end wall flow is predicted to be in a worse state by the RANS solution than both LES and measurements with more accuracy in the LES model. Even then there are still some differences between LES prediction and measurements probably due to the separated flow produced in the LES simulation. Whilst differences exist between RANS and LES, it does not seem that the LES solution could be claimed to be closer to measurements in every respect, although some aspects (e.g. the IGV effect) do seem better predicted. There is less curvature seen in the right hand high velocity island in the LES compared with RANS, and this does reflect what is seen in the measurement.

(a) High-Re RANS

(b) R^2M

(c) measured data
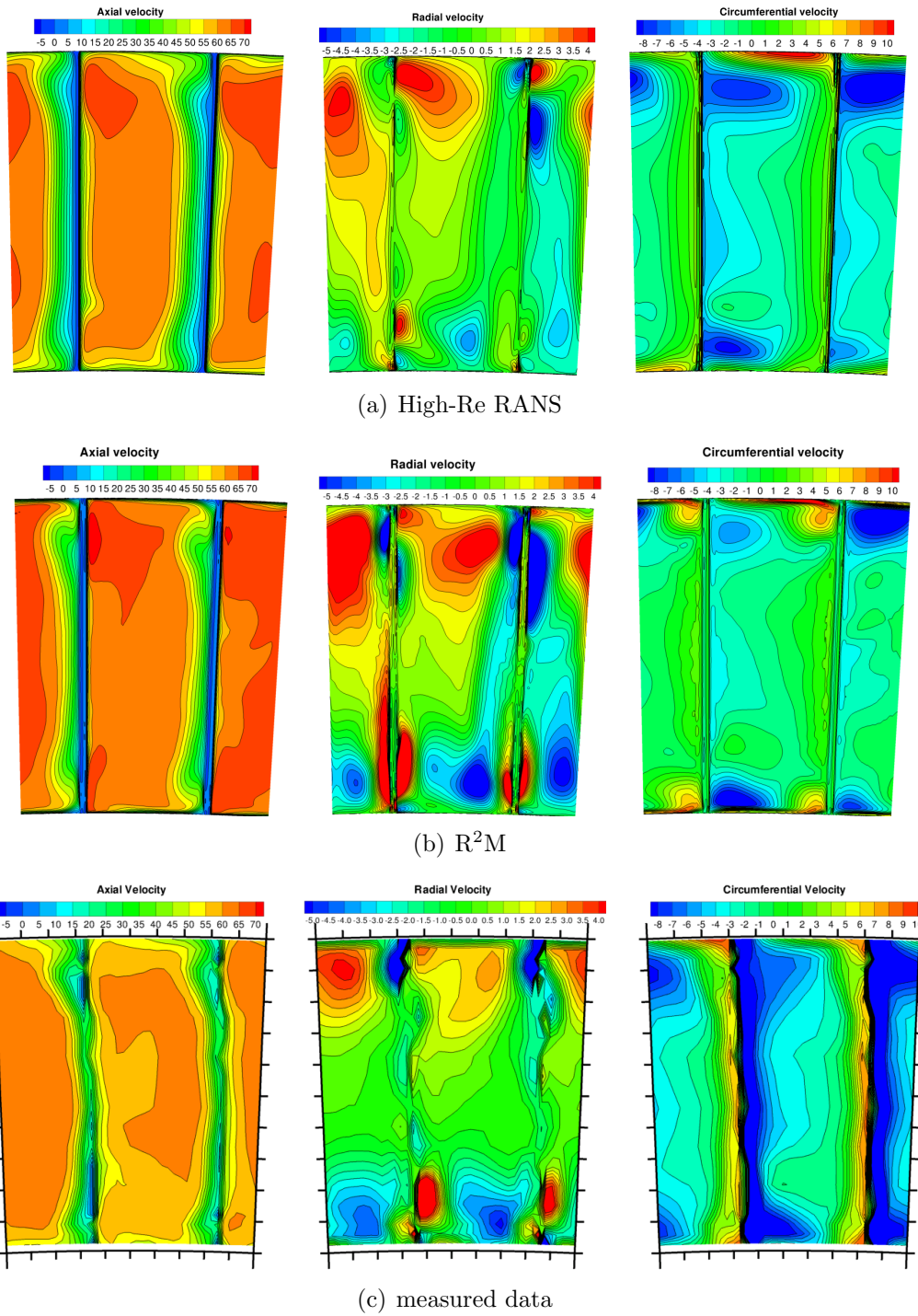
Figure 3.47: Mean velocity contours at OGV exit (upstream view)

(a) High-Re RANS   (b) R²M   (c) exp. data
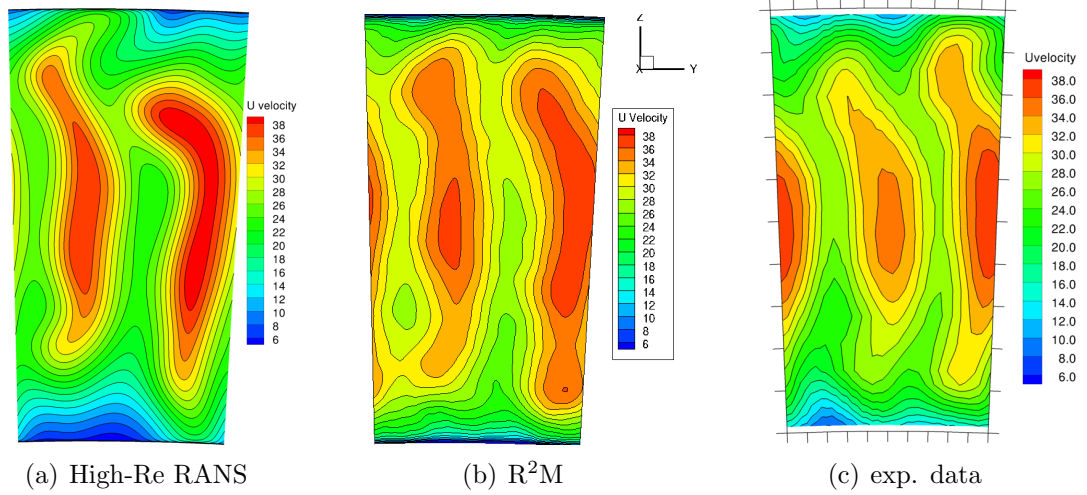
Figure 3.48: Mean axial velocity contours at the prediffuser exit (upstream view)

3.3.6   Loss and Pressure Rise Performance

The overall system performance from both CFD solutions and measurements is summarised in Table 3.2. Mass-weighted total pressure loss λ and static pressure recovery C_p coefficients for the isolated OGV row (C_{pV}, λ_V), prediffuser (C_{pd}, λ_d) and overall OGV/prediffuser system are again presented. Compared to the measured performance coefficients it can be noted that:

(i) the high-Re RANS model provides better agreement with the overall total pressure loss with only 0.8% overprediction, whilst LES predicted a value 28% too low.

(ii) this worse overall performance of LES is dominated by the poor performance of vane losses (43% too low)

(iii) in the prediffuser the LES approach has performed better, with λ only $\approx$18% overprediction compared to $\approx$ 36% overprediction by RANS.

For overall performance in terms of performance coefficients RANS has captured the OGV row better, whereas LES has performed better in the prediffuser.

Table 3.2: the OGV/prediffuser performance data

	C_{pV}	λ_V	C_{pd}	λ_d	C_p	λ
High-Reynolds	0.3467	0.1105	0.5509	0.0749	0.6457	0.1512
LES R^{2}M	0.3276	0.0679	0.5559	0.0652	0.6636	0.1074
Exp.	0.38	0.12	0.55	0.055	0.66	0.15

3.4 Summary

The results of the predictions presented in this chapter show that although high Re and low Re turbulence model RANS calculations do display different features, both predictions show essentially the same overall characteristics for the development of the OGV/prediffuser flow. In fact, for global system performance parameters such as pressure rise or loss coefficient, the high Re model is closer to the experimental data. The cause identified for this was the poor prediction of the low Re model for vane loss. Although the low Re model is capable of predicting the relaminarisation process, its ability to capture the return to turbulence process is perhaps not as well validated. As a consequence if the predicted boundary layer is still laminar or weakly turbulent, it will separate when it encounters the adverse pressure gradient at the rear of the vane, whereas this has probably not happened in the experiment. Hence, the use of a high Re approach in optimisation methods, which include many CFD runs, seems to be justified. Equally, at present in terms of RANS modelling, the high Re CFD provides the better results.

Further, in a manner similar to the comment above on the low Re RANS results, separation on the vane suction surface were predicted by a full LES modelling. These have a similar effect on producing OGV exit profiles for the full LES which are no better than the high Re RANS result, and possibly contain regions of unrepresentative high turbulence and shear stress which then 'contaminate' predicted flow development in the prediffuser. It seems that appreciably more grid nodes, and perhaps a more advanced SGS model, would be needed to allow the full LES approach to capture the complex flow physics of the OGV suction surface flow. Unfortunately this would be prohibitively expensive. The LES grid would need considerable refinement, accompanied by a better SGS model (e.g. a

transport-equation SGS model) than the simple Smagorinsky, to cope with the flow complexities in the OGV flow. Thus, a zonal hybrid RANS/LES approach is well worthy of investigation, and this is presented in the following chapter.

Chapter 4

Hybrid RANS/LES Interface Treatment

4.1 Introduction

Hybrid RANS/LES simulations have received considerable attention over recent years due to their ability to apply the high accuracy of LES only in regions of the flow where its advanced turbulence modelling approach can deliver benefits economically. In a typical application, LES CFD is applied in the region where complex anisotropic turbulence structures or flow separations prevail and RANS CFD is coupled to the LES CFD in the remainder of the computational domain.

Reviews of previously published hybrid RANS/LES simulations can be found in chapter 1 which gave an outline of the two broad catalogues of Hybrid methods – global and zonal [44]– the discussion in Chapter 1 argued that the approach most appropriate to the OGV/prediffuser application was the zonal method. The main difficulty that arises in zonal methods is to determine how information is exchanged at the RANS/LES domain interface. In the RANS zone the flow solution is (usually) statistically steady and the Reynolds stresses are entirely provided by the statistical turbulence model. In the LES region, on the other hand, the resolved (unsteady) scales contain most of the fluctuating turbulence energy and hence contribute most to the time-averaged Reynolds shear stress. As a conse-

quence, there is a crucial need for methods able to address how these two quite different approaches to handling turbulence can communicate physically accurately with each other at the RANS/LES interface.

As pointed out in chapter 1, this communication problem is essentially identical to the question of how RANS CFD information can be complemented to provide unsteady, physically correctly correlated information in the context of inlet condtion generation for a 'pure' LES solution, as addressed in the previous chapter by using the R^2M technique.

In fact a technique similar to R^2M was employed by Schlüter et al. [23] in a hybrid RANS/LES calculation, where an inflow boundary-condition for the LES region was generated by re-scaling an instantaneous flow database from a separate LES calculation to match an upstream RANS solution. As commented in the Introduction to this thesis, the approach of Schlüter et al. [23] is not believed to be very appropriate, since the separate LES calculation database that was re-scaled was of a quite different flow (fully-developed pipeflow) to the flow field existing at the RANS/LES interface (a compressor exit flow). Instead, the route followed here is very much in line with the R^2M approach described above.

A zonal hybrid RANS/LES has been carried out for the OGV/prediffuser flow, where RANS CFD is applied to the OGV region and LES CFD is used in the prediffuser. The LES solution domain is attached directly downstream of the RANS solution domain. The RANS domain exit flow information is used as the target data to 'drive' an R^2M calculation to generate the unsteady inflow boundary conditions for the LES domain. Interfacing these two CFD techniques requires the generation of turbulent eddies in the LES field capable of supporting the time-averaged Reynolds stresses provided by the RANS field.

The R^2M technique requires an input specification of ('target') data not only for the 3 mean velocity components but also for all three individual turbulent normal stresses. The former are of course readily available from any RANS CFD predictions; the latter are not so readily available when only an eddy viscosity

turbulence model has been used, since this provides only the value of the <u>total</u> turbulence energy k not its separate components. The Bounssinesq relationship could be used to derive these, but this is not usually found to be adequate, often leading to negative normal stresses. A simple but more accurate approach to this has been used and is described in this chapter. A new method based on use of an Algebraic Stress Model (ASM) was adopted to extract anisotropic individual Reynolds normal stresses from the RANS $k - \epsilon$ results at the interface. These were then used together with the mean velocity field to supply the target information required by the R^{2}M technique to generate unsteady inflow data for the LES region.

4.2 Set up of Hybrid RANS/LES Interface Treatment

To specify the precise location of the RANS/LES interface is a critical issue since this can impact the prediction significantly. However, no general criterion has been proposed so far for the zonal approach. For the current flow case (the OGV/prediffuser assembly), the OGV region is occupied by (presumed) attached boundary layer flows. On the other hand, the diffuser region is dominated by (i) turbulent mixing out of the 3D wake flow and (ii) adverse pressure gradient influenced flow. Studies over the last few decades have largely shown that LES can deliver superior predictions to RANS for free shear flows such as jets, mixing layers, and wakes. For high Re wall dominated flow, however, the results have been much less encouraging. Here, the length scale of the dynamically important motions decreases towards the wall – in a sense, the energetic, dynamically important scales are no longer 'large', and the interpretation of LES is no longer unambiguous. Hence, in the present study, RANS was applied in the OGV region and LES in the diffuser region. The division between the RANS (red line) and LES (black line) zones is shown in Figure 4.1, where the LES zone starts a small distance downstream of the OGV row trailing edge to avoid any small recirculation zone. An overlapping zone (between the RANS/LES interface and

the RANS outlet plane) was chosen in order to exclude excess influence of the outflow boundary condition applied at the RANS domain outlet.
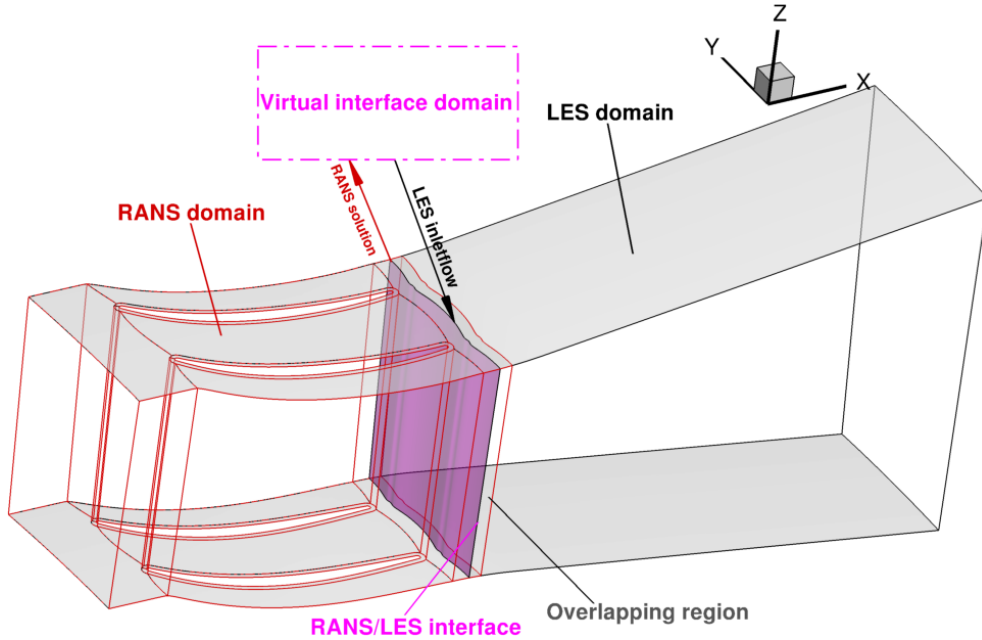
Figure 4.1: RANS/LES computational zones division in OGV/prediffuser

It is assumed that at the location of the (red) downstream boundary in the RANS zone, the velocity is everywhere out of the RANS domain and there are negligible upstream pressure effects. The need for information exchange is therefore only in the flow direction from the upstream to the downstream flow solver: the convective terms in the governing equations transfer information in the direction of the velocity vector and the LES inlet plane is located where the axial velocity is everywhere positive. Hence, for the upstream RANS region, an outflow boundary condition (zero gradient) was set at the RANS domain boundary; and for the downstream LES, the inlet unsteady velocity field is delivered by an R^2M approach driven by data extracted from the RANS solution.

As explained above, since at least part of the turbulence energy spectra is temporally resolved in LES, the challenge is to generate an appropriate unsteady field which is constructed to have the same turbulence energy as implied at each point
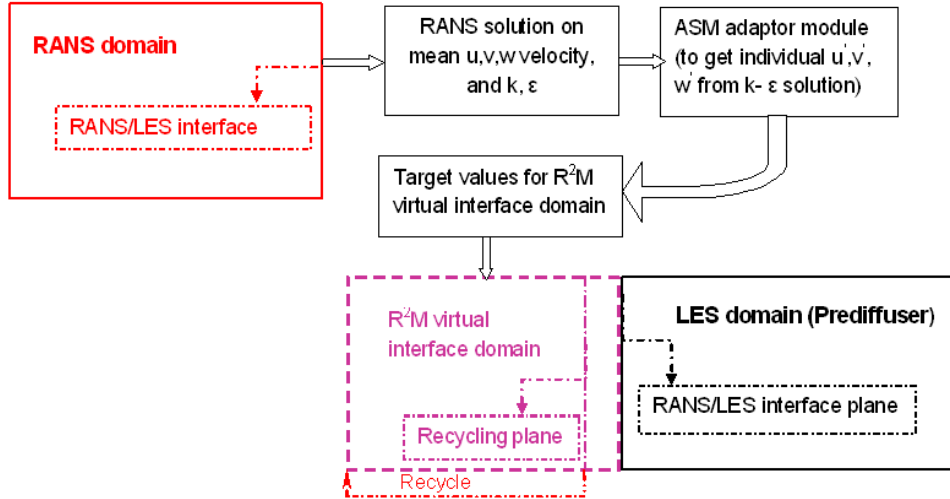
Figure 4.2: Schematic diagram of the RANS/LES coupling in OGV/prediffuser

by the RANS CFD. The next section details the approach adopted to solve this problem. The R²M technique will be used to achieve this. As described in the pure LES use of this technique in Chapter 3, R²M requires creation of an inlet condition generation domain. When used as part of an interfacing treatment, this domain is a "virtual interface domain" which exists computationally between the RANS and LES domain, but does not occupy any part of the physical (geometrical) domain. The schematic diagram of the RANS/LES coupling is illustrated in Figure 4.2; the "virtual interface domain" is used to extract RANS data, generate LES compatible data using R²M and refer it to the LES domain.

4.3 RANS/LES Interface Methodology Based on Use of An Algebraic Stress Model

4.3.1 RANS data

Before attempting to define the LES inflow, it is useful to have a closer look at the data delivered by the RANS flow solver. In a steady RANS computation, the velocity components appear explicitly as part of the time-averaged solution. Similarly, all turbulent motions are described statistically via the turbulence model. From the point of view of using an R^{2}M approach to guide the generation of the unsteady velocity field required by the LES flow solver, it would be most convenient to use a full Reynolds-stress turbulence model, where each of the Reynolds normal stresses needed as R^{2}M target data is modeled by its own transport equation. However, the most popular (and computationally affordable) turbulence models for RANS computations are two-equation models based on an eddy viscosity assumption, which deliver information only on the time-averaged value of the turbulent kinetic energy of the turbulent fluctuations.

Various approaches, of increasing complexity, can be adopted to convert RANS information on k at any grid node into information on the 3 components of k – the Reynolds normal stresses. For example, assuming isotropy, the normal stresses of the Reynolds stress tensor can be recovered from:

$$\overline{u_i'^2} = \frac{2}{3}k, \quad i = 1, 2, 3 \tag{4.1}$$

A more consistent approach would be to follow the Bounssinesq hypothesis as assumed by all eddy viscosity models whereby each Reynolds stress component is defined by:

$$\overline{u_i' u_j'} = -\nu_t \left(\frac{\partial \overline{u_i}}{\partial x_j} + \frac{\partial \overline{u_j}}{\partial x_i}\right) + \frac{2}{3}k\delta_{ij} \tag{4.2}$$

Eq. 4.2 does not strictly imply isotropy of the 3 normal stresses; the turbulent viscosity ν_t is isotropic (it is a scalar) but the appearance of the strain rate term in eq. 4.2 means $\overline{u_1'^2}$, $\overline{u_2'^2}$ etc can deviate from the isotropic $2/3k$ value, however,

the strain rate is only a local quality and takes no account of any of the important physical processes that contribute to the <u>individual</u> normal stress anisotropy (particularly anisotropic convection, diffusion and generation processes). Thus the normal stress values delivered from eq. 4.2 are in general not found to reflect observed normal stress anisotropy well. In reality, downstream of the OGV row, with strong 3D wakes, the distribution of turbulence intensity is likely to be far from isotropic. An alternative approach is needed to extract a representative Reynolds normal stress field at OGV exit from the turbulence energy provided by the $k - \epsilon$ model – the approach chosen here is to use an Algebraic Stress Model (ASM).

4.3.2 'Adaptor' Methodology Based on ASM

In order to produce more realistic turbulence statistics for the LES inlet, an 'adaptor' step based on an algebraic stress models (ASM) is applied. The classical algebraic stress model(ASM) approach is outlined in Pope [12] as being developed via an approximate modelling of the Reynolds stress ($\tau_{ij} \equiv \overline{u_i' u_j'}$) transport equations which may be written as follows:

$$T_{ij} = \frac{\partial}{\partial x_k}(\rho \overline{u_k} \overline{u_i' u_j'}) - \frac{\partial}{\partial x_k}(\frac{C_s k}{\epsilon} \tau_{kl} \frac{\partial \tau_{ij}}{\partial x_l}) = P_{ij} + R_{ij} - \frac{2}{3}\epsilon \delta_{ij} \qquad (4.3)$$

Where P_{ij} is the production term, R_{ij} is the (modelled) pressure strain term, and an isotropic assumption has been made for the dissipation term. The left hand side T_{ij} represents the balance between convection and diffusion terms, i.e. all <u>transport</u> terms.

If an assumption is made that the transport terms for any individual Reynolds stress component may be related to the transport terms in the modelled k equation pro rata with the ratio of the individual stress to k, then Pope [12] shows this may be written as:

$$T_{ij} = \frac{\tau_{ij}}{k}(P_k - \epsilon) = \frac{\overline{u_i' u_j'}}{k}(P_k - \epsilon) \qquad (4.4)$$

Where P_k represents the production term in the k equation. The final ASM relation may be defined by combining eqs 4.3 and 4.4:

$$\frac{\overline{u_i' u_j'}}{k}(P_k - \epsilon) = P_{ij} + R_{ij} - \frac{2}{3}\epsilon\delta_{ij} \tag{4.5}$$

The precise structure of eq. 4.5 depends on the choice of the model for the R_{ij} term. For the present study, the simplest model of Gibson and Launder [119] has been chosen, which is:

$$R_{ij} = -C_1\frac{\epsilon}{k}(\overline{u_i' u_j'} - \frac{2}{3}k\delta_{ij}) - C_2(P_{ij} - \frac{2}{3}P_k\delta_{ij}) \tag{4.6}$$

Consequently, the ASM becomes:

$$\frac{\overline{u_i' u_j'}}{k}(P_k - \epsilon + C_1\epsilon) = (1 - C_2)P_{ij} + \frac{2}{3}(C_2 P_k + (C_1 - 1)\epsilon)\delta_{ij} \tag{4.7}$$

This compromises six independent (but implicit) algebraic equations for the six individual Reynolds stress components $\overline{u_i' u_j'}$. Eq. 4.7 can be solved (by matrix inversion) to determine the Reynolds stresses $\overline{u_i' u_j'}$ as long as k and ϵ and the mean velocity gradients (which appear in P_{ij} and P_k) are known (these are of course precisely what is output by the RANS solution).

The production tensor is given by:

$$P_{ij} = -\overline{u_i' u_k'}\frac{\partial \overline{u_j}}{\partial x_k} - \overline{u_j' u_k'}\frac{\partial \overline{u_i}}{\partial x_k} \tag{4.8}$$

The production of kinetic energy P_k is given in terms of ν_t and $\partial \overline{u_i}/\partial x_j$ by :

$$P_k = \frac{1}{2}P_{ii} = -\overline{u_i' u_j'}\frac{\partial \overline{u_i}}{\partial x_j} \approx \nu_t(\frac{\partial \overline{u_i}}{\partial x_j} + \frac{\partial \overline{u_j}}{\partial x_i})\frac{\partial \overline{u_i}}{\partial x_j} \tag{4.9}$$

The model constants are taken to be $C_1 = 1.8, C_2 = 0.6$.

4.3.3 Illustration of Data Extracted from RANS Using the ASM Technique

Figures 4.3 and 4.4 show the important data extracted from the high Re RANS solution at the RANS/LES interface and required by the ASM equations, namely the turbulence energy k, the dissipation ϵ and the 6 strain rate components. The turbulence is high in the wake region because of the existence of high gradients caused by the interaction of the two vane (suction and pressure side) boundary layers. Similarly high magnitudes of the two normal strain rates S_{11} and S_{22} appear in the wake region. The largest shear strain rate is S_{12}, which is bigger by around a factor of 3 compared to the other shear stresses. This is because the u, v velocities change significantly in each of the axial and azimuthal directions in the wake region. At the same time, the normal strain S_{33} and the shear strains S_{13}, S_{23} take on large values in the two end wall regions. These clearly non-zero values of all six strain rates indicate how strongly 3D the OGV wake flow is.

Using the data shown in Figures 4.3 and 4.4, the 'adaptor' method based on the ASM produced the six components of the Reynolds stresses at the RANS/LES interface as shown in Figure 4.5. Note that compared with the values obtained using eq. 4.2, a highly anisotropic normal stress field is produced with the maximum stress being the $\overline{u'^2}$ component and the ratio of $\overline{u'^2}/\overline{v'^2}/\overline{w'^2}$ in the region of high turbulence being 1/0.6/0.5 (approximately 1/1/1 from eq. 4.2) and the $\overline{u'v'}$ shear stress being dominant on the edges of the blade surface, but $\overline{u'w'}$ and $\overline{v'w'}$ being high and negative near the outer end wall. The data shown in Figure 4.5, together with the mean velocity components, complete the target data that required to drive the R²M technique at the RANS/LES interface.
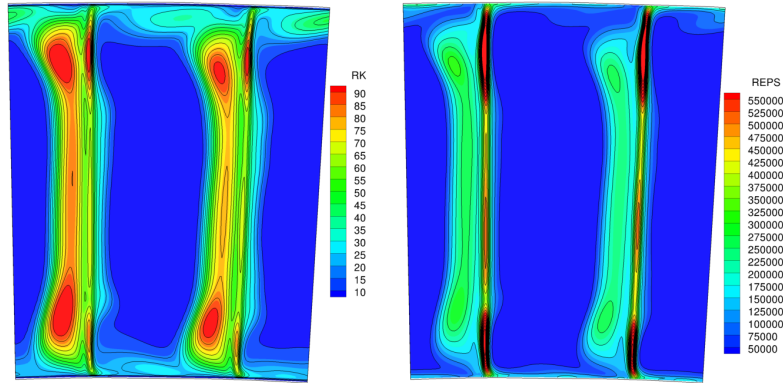
Figure 4.3: Contours of data extracted from high-Re RANS solution at the RAN/LES interface

(a) Normal strains

(b) Shear strains
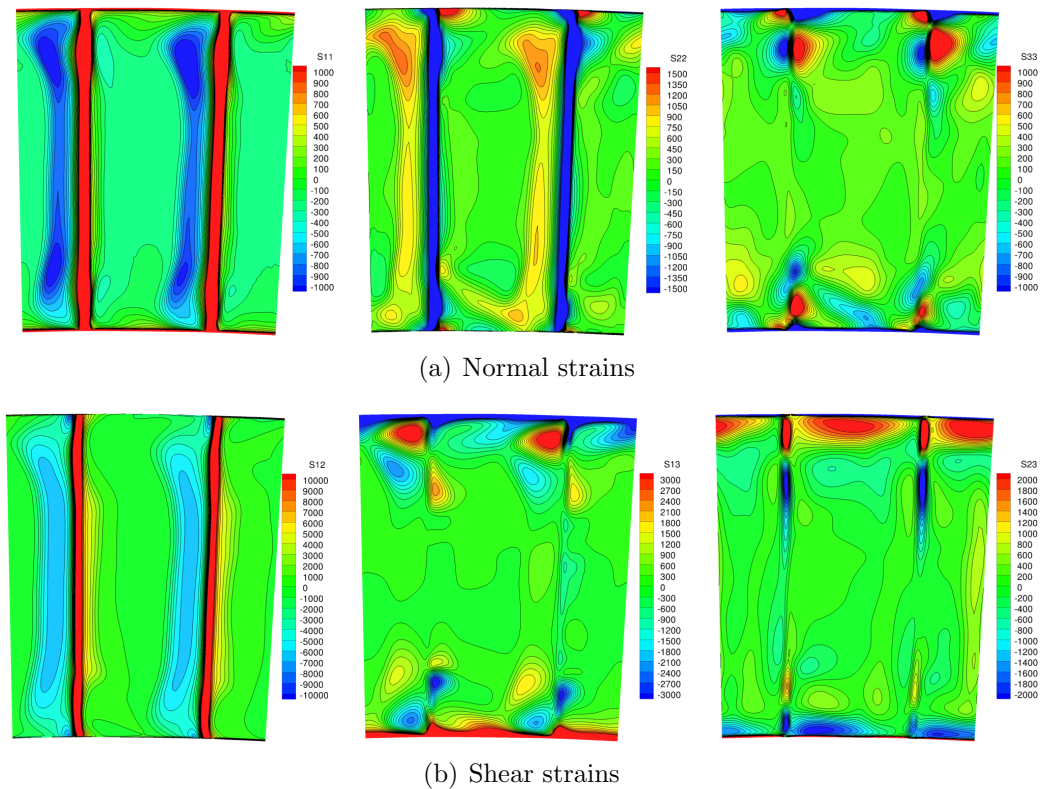
Figure 4.4: Contours of strain rate extracted from high-Re RANS solution at the RAN/LES interface

127
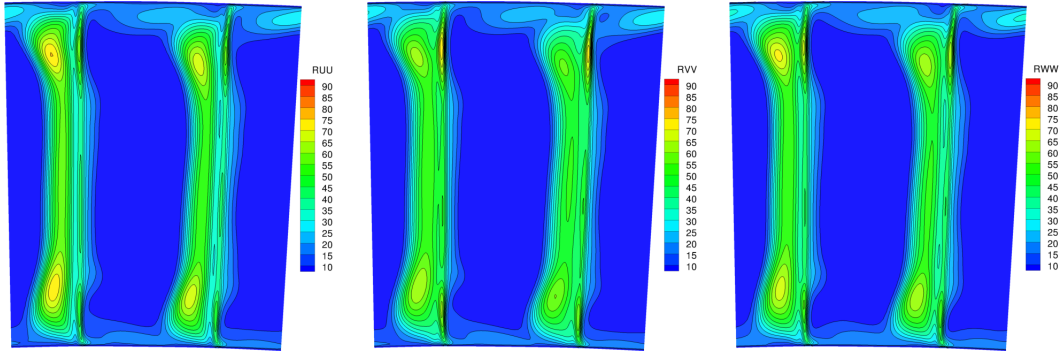
(a) Reynolds normal stresses using eq. 4.2
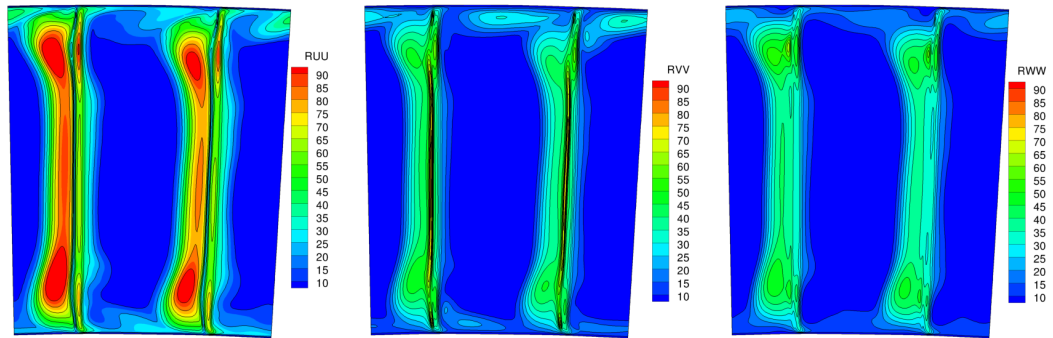
(b) Reynolds normal stresses using the ASM technique
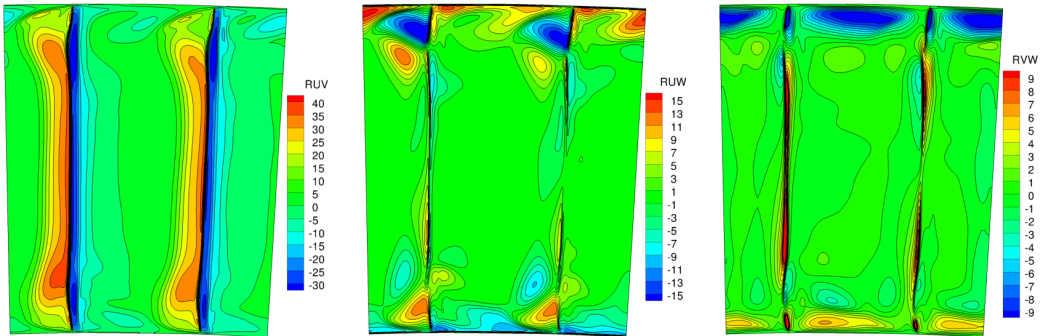
(c) Reynolds shear stresses using the ASM technique

Figure 4.5: Contours of Reynolds stress components extracted at the RANS/LES interface

4.3.4 RANS to LES Coupling – Summary

In the present work an improved method has been proposed for RANS/LES coupling based on an ASM 'adaptor'. After using the ASM to complete the generation of target data from the available RANS solution, the R^{2}M technique proposed in section 3.3.2 (method B) can now be used to generate LES compatible unsteady inlet data. The procedure for information coupling between RANS and LES is illustrated schematically in Figure 4.6.
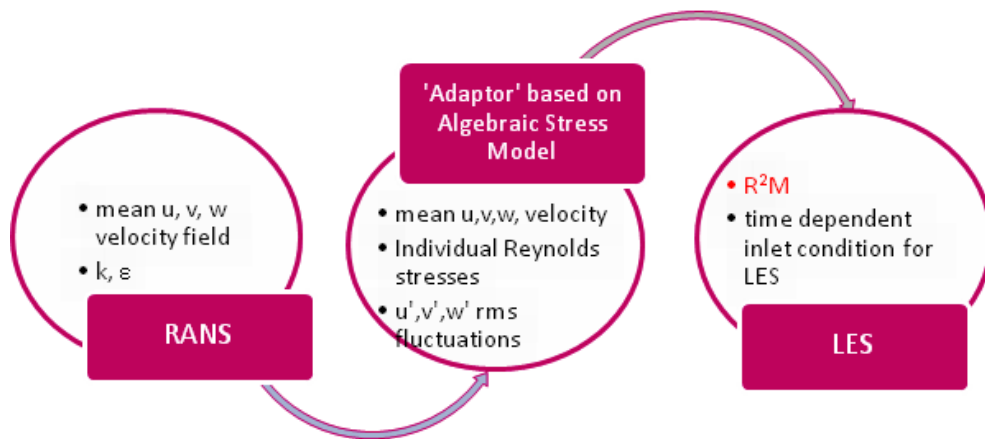
Figure 4.6: Flow chart of RANS-to-LES coupling

Chapter 5

Hybrid RANS/LES Results

5.1 Hybrid RANS/LES Simulation of A Conventional OGV/prediffuser Design

5.1.1 Boundary Conditions

For the RANS computational domain, the same specified (2D) velocity inlet conditions were applied as used in the high Re $k - \epsilon$ RANS simulation presented earlier in Chapter 3; at the outlet plane, since it was decided to have a 'one-way' connection between RANS and LES domain, a zero gradient condition was applied. For the LES domain, the inlet conditions were generated using the interfacing R^{2}M based method as introduced in chapter 4. In this way, the statistical velocity and turbulence information generated by the RANS solution was created as spatially continuous input to the LES domain. The usual convective outflow condition was applied at the LES domain outlet plane (prediffuser exit).

5.1.2 Numerical Results

When the R^{2}M based RANS/LES interfacing approach is applied, an extra interface block must be considered at the inlet of the prediffuser and run simultaneously with the main LES simulation domain (the R^{2}M block as shown in Figure 5.5 below). As explained in Chapter 4, it is important to ensure that the axial length of this interface block is sufficiently large that it does not con-

strain the axial correlation length scales generated by the interfacing approach. This is best assessed by examining the length scale implied by the two-point spatial correlation in the axial direction extracted from the unsteady LES solution provided by the interfacing method. The non-dimensional 2-point 2nd order axial separation correlation $R_{11}/u'^2 (= \overline{u_1(x_{ref} + dx, t) u_1(x_{ref}, t)} / \overline{u_1^2(x_{ref})}$) and the derived axial integral lengthscale $L_{11} (= \int_0^\infty R_{11}/u'^2 dx)$ are shown in Figure 5.1. Two typical positions are chosen, one from the middle of the blade passage ($y^* = dy/2s = 0.5, z^* = dz/h = 0.5$, where s indicates the distance between the vane and h indicates the height of the vane) and the other from the blade trailing edge ($y^* = 0.25, z^* = 0.5$) at 50 % of the span of the OGV. Decorrelation of fluctuations is achieved within half the domain length in the streamwise direction, which indicates that the R²M computational domain is large enough. The correlations exhibit a second peak near the outlet of the R²M domain only due to the recycling process adopted. The longitudinal integral lengthscale extracted from the two-point correlation, which is characteristic of the larger eddies, is shown in Figure 5.1 (b) for the lengthscale in the middle of the blade passage where larger turbulence scales were found. It is noted that the R²M domain length is several times larger than the biggest eddy integral lengthscale, which comprises ≈15% of the domain length.

(a) Longitudinal autocorrelation function

(b) Longitudinal integral scale
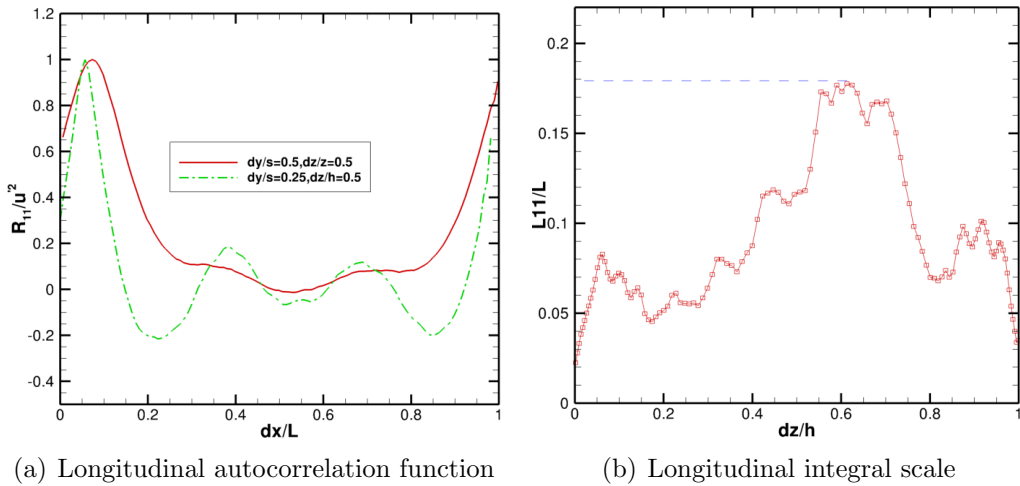
Figure 5.1: Axial two-point autocorrelation across the R²M block

Since the flow at OGV exit is characterised by strong radial and circumferential variations, two profiles in the corresponding directions were chosen (Figure 5.2) to examine the statistical properties of the unsteady velocity field generated by the interfacing method. The two profiles chosen enable the strong spanwise gradients present in the OGV wakes and the strong radial gradients present in the end wall boundary layer to be examined. Figures 5.3 and 5.4 present comparisons of mean velocities and turbulent Reynolds normal stresses between values generated from the interface technique and those extracted directly from the RANS domain solution. These results show excellent agreement between target RANS values and interface statistics derived from the LES unsteady field along both circumferential and radial directions. Small under-predictions (approximately 1% to 3% for v velocity) are detected in the wake region (Figure 5.3). Similarly, a small (4%) over-prediction of the Reynolds normal stress $\overline{\rho v' v'}$ may be seen in the OGV blade wake region outside the endwall boundary layers (Figure 5.3b).
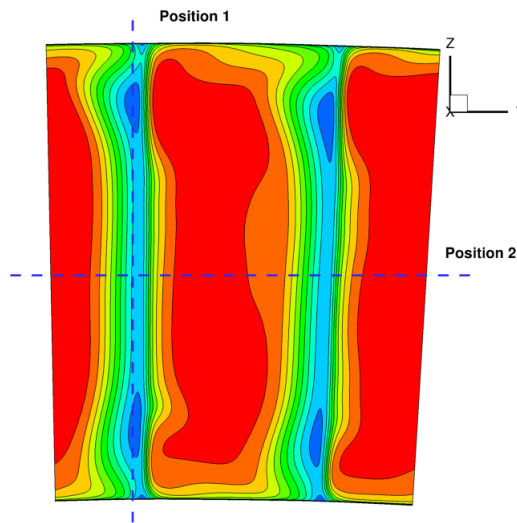
Figure 5.2: Selected positions to compare in the interface

The flow structure in Figure 5.3 shows the low axial velocity region over the central 80% of the passage length, with two deeper low momentum zones indicating hub and tip effects; the velocity then rises before falling again in the two endwall boundary layers. The effectiveness of the OGV in removing almost all of the rotor
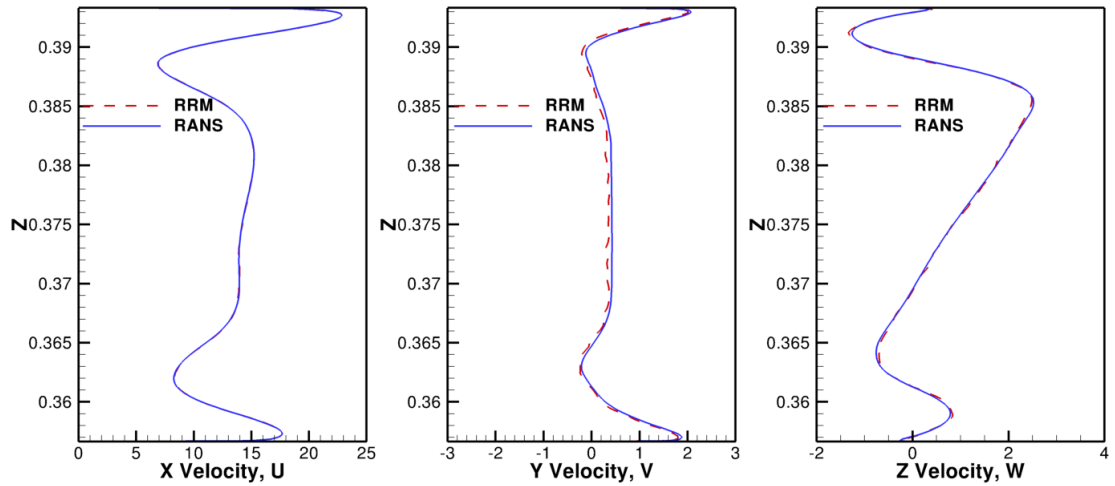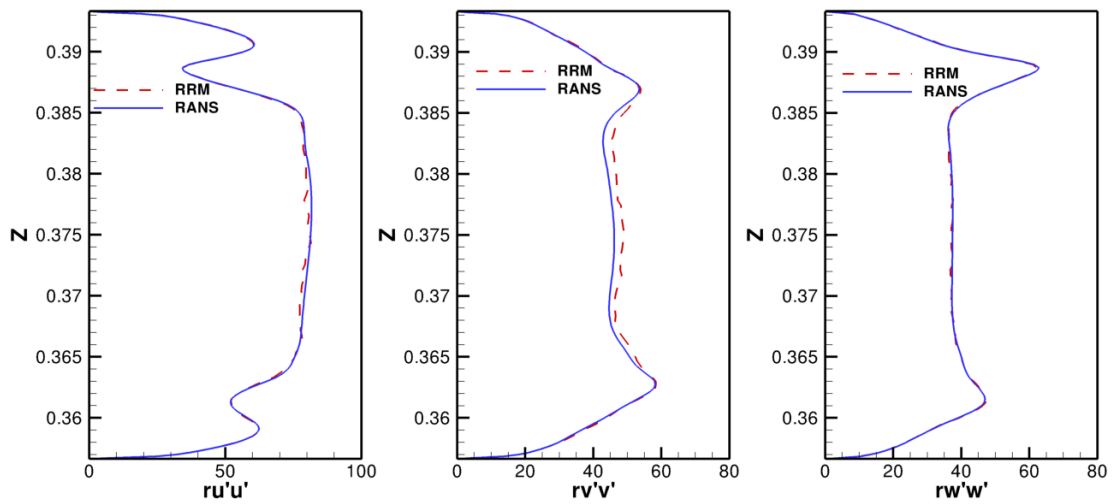
(a) Mean velocity

(b) Reynolds normal stresses

Figure 5.3: Comparison between regenerated turbulence statistical profiles and the RANS target values (position 1)
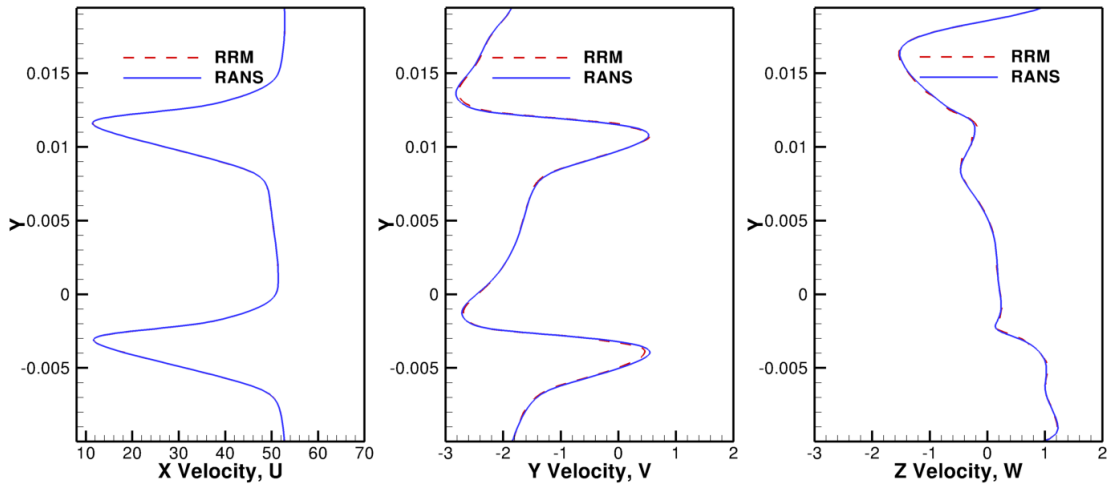
(a) Mean velocity
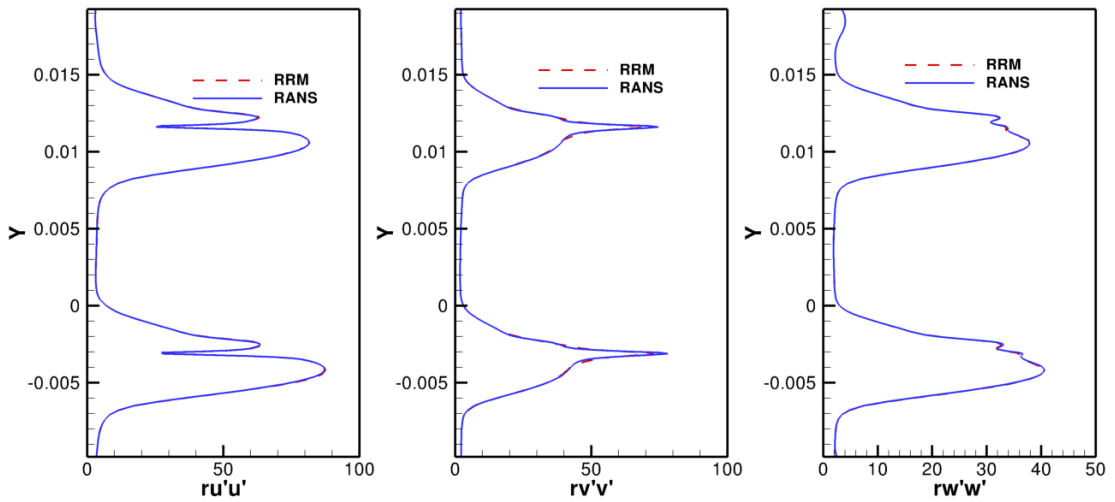
(b) Reynolds normal stresses

Figure 5.4: Comparison between regenerated turbulence statistical profiles and the RANS target values (position 2)

swirl is shown by the low v velocity, only of order 0.1 m/s. Finally, the change in sign of the w velocity in the core of the wake shows that the flow is being driven towards each endwall. The turbulence statistics show low anisotropy in the core of the wake flow with $u' : v' : w'$ of 1:0.6:0.5; anisotropy is higher in the region where wake and endwall boundary layers merge, where $u' : v' : w'$ is 1:0.5:0.35. The OGV wake structure is seen best in the azimuthal profiles in Figure 5.4. The small positive v velocity in the central region of the passage indicates a small underturning is predicted. The high turbulence levels in the wake are easily visible, with different structure appearing in u', v', w' profiles in the near wake region; for example, the two peaks in the u' profile are a consequence of the different levels of turbulence created by the OGV pressure and suction side boundary layers which merge in the wake, but at this section close to the trailing edge have still not diffused into a smooth profile. One final important point to note is that the close similarity in LES-derived turbulence energy implied by the figures compared to the total turbulence energy in the RANS solution, shows that the interface treatment transports all energy generated in the RANS domain across the RANS/LES interface.

The unsteady velocity field created by the interface treatment and passing into the LES domain is displayed in Figures 5.5 and 5.6 via instantaneous axial velocity contours in two orthogonal planes (Figure 5.5) and a coloured isosurface of the Q-criterion (Figure 5.6) (a Q contour level of $Q = 6 \times 10^4$ which best shows details on the vortex structures has been chosen). Using the Q-criterion small vortex-like structures may be detected in the prediffuser flow. Figures 5.5 and 5.6 illustrate how the unsteady turbulent eddies develop within the prediffuser. Turbulence, present only statistically in the upstream RANS domain has to be generated as an unsteady field in the LES domain, driven by the unsteady inlet conditions at the LES inflow boundary. It can be seen that the turbulence present in the OGV wakes and endwall boundary layers, when displayed as unsteady velocity contours which show the eddy structure growing in these instantaneous snapshots. The turbulent stator wakes in the RANS domain are modeled with an eddy viscosity model, which gives these a very smooth appearance. In the LES domain, the turbulence is converted into unsteady resolved fluctuations, and hence dynamical

vortical structures can be identified.
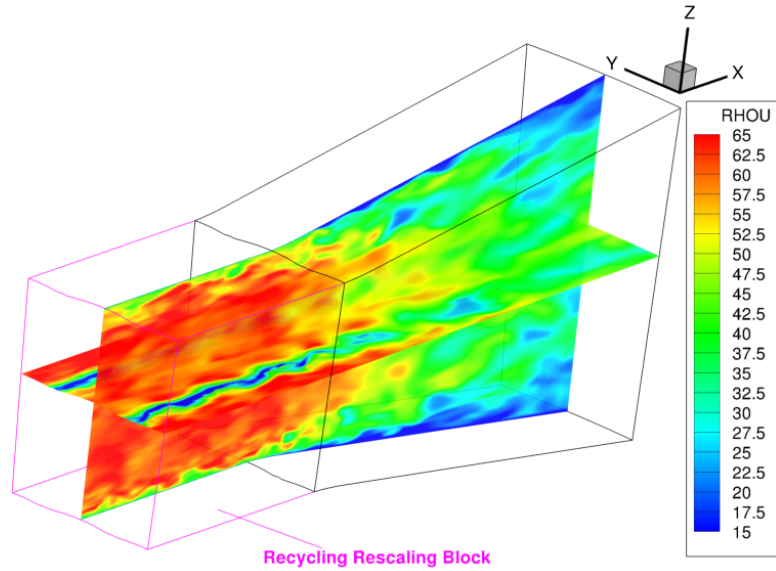
Figure 5.5: Instantaneous axial velocity contours in the diffuser
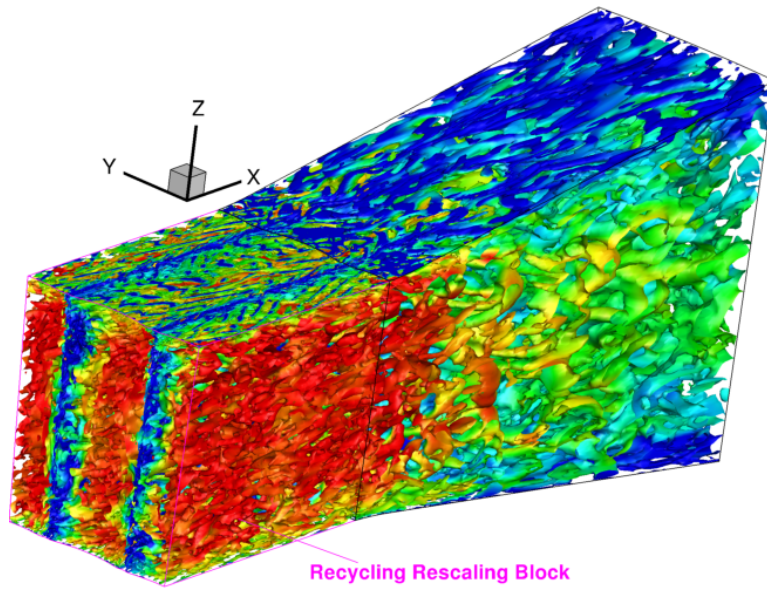
Figure 5.6: Isosurfaces of Q-criterion($Q = 6 \times 10^4$) colored by instantaneous axial velocity

This is visualised most clearly in Figure 5.7 which shows the steady wakes of the OGVs identified clearly in the RANS domain being transformed into unsteady

136

wakes in the LES domain on an axial/azimuthal plane at 50% of the OGV span. This picture shows that the OGV wakes merge just past the mid-prediffuser length, although this is of course an unsteady location, varying in time between 60% and 95% of prediffuser length. The predicted time-averaged turbulent OGV wakes propagating downstream in the prediffuser are shown via time-mean axial velocity (Figure 5.8) and turbulence kinetic energy contours (Figure 5.9) again on the same radial plane as Figure 5.7. The wakes of the OGV can clearly be identified as continuous between RANS and LES domains. The communication of the flow solvers at the interface is hereby demonstrated as ensuring that the 3D flow features are transferred from the upstream flow solver to the downstream domain, and the wakes propagates correctly across the interface.
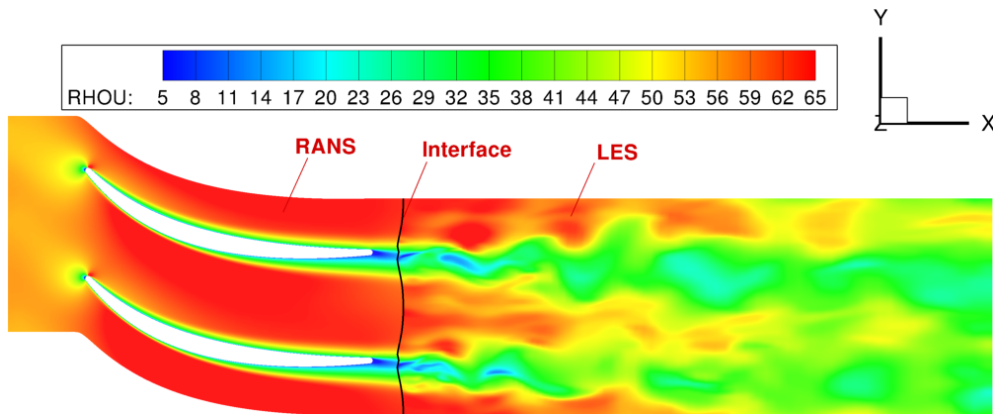
Figure 5.7: Velocity contours of OGV prediffuser : RANS mean velocity to LES instantaneous velocity

Figure 5.9 shows that in the high turbulence region, compared with full RANS solution the wakes in the hybrid RANS/LES solution contain higher turbulence and mix out more quickly, which results in apparently thicker wakes in the prediffuser (LES domain). The difference between the upper and lower vane wakes reflects the influence of the upstream IGV wake, where the upper vane in the figure has the IGV geometrically upstream. The lower level of turbulence and smaller region of high turbulence are predicted by both methods.

Figure 5.10 compares the hybrid RANS/LES predicted mean axial velocity distribution at prediffuser exit with the full RANS solution and with measured data.
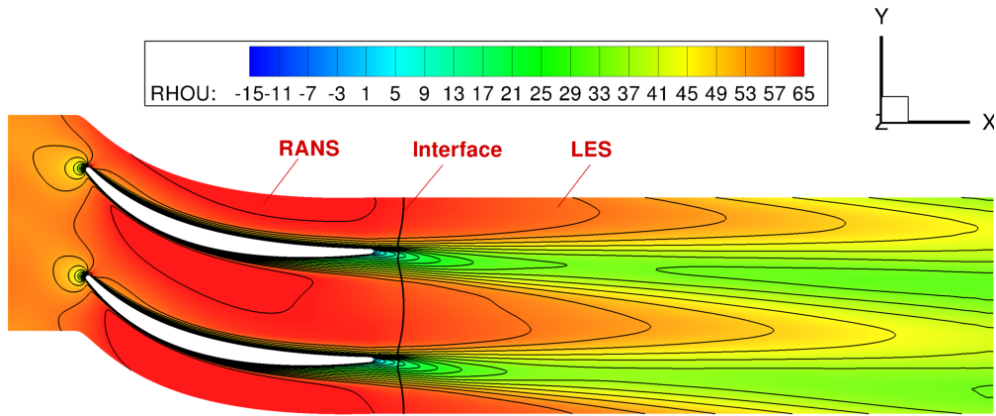
Figure 5.8: Mean velocity contours of OGV(RANS) and diffuser(LES)
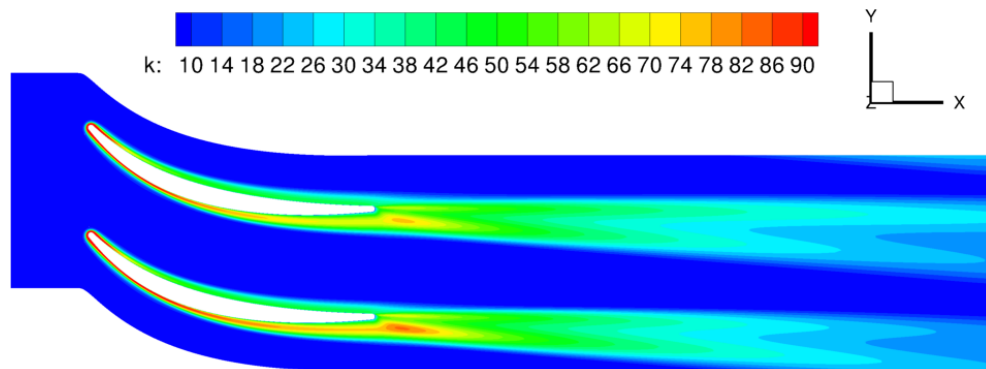
(a) High-Re RANS
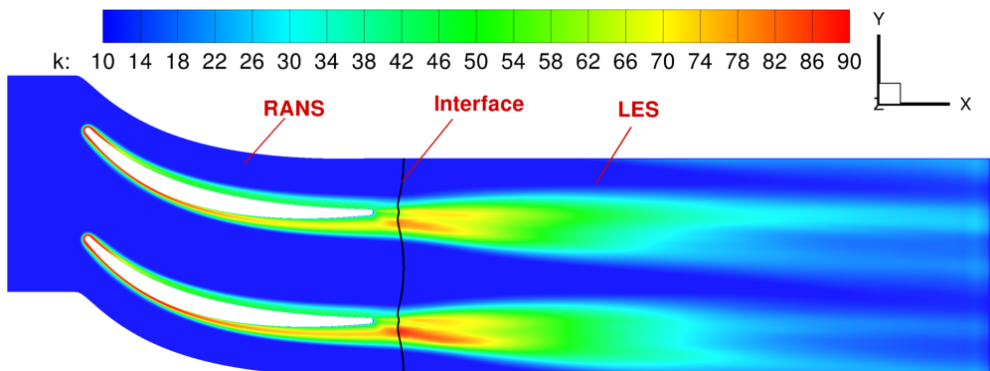
(b) Hybrid RANS/LES with OGV(RANS) and diffuser(LES)

Figure 5.9: Turbulent kinetic engergy contours

138

The hybrid RANS/LES shows an improved prediction for both axial velocity magnitude and contour shapes compared with the full RANS result. Improved end wall boundary layers predictions are also observed in the hybrid RANS/LES solution, especially the inner end wall boundary layer which is very close to the measurement and clearly better than the full RANS prediction. If compared to the full LES solution in Figure 3.48, there has been a clear improvement when adopting the hybrid approach, the comparison of Figure 5.10b with experiments is closer than either full RANS or full LES predictions.

(a) High-Re RANS   (b) hybrid RANS-LES   (c) exp. data
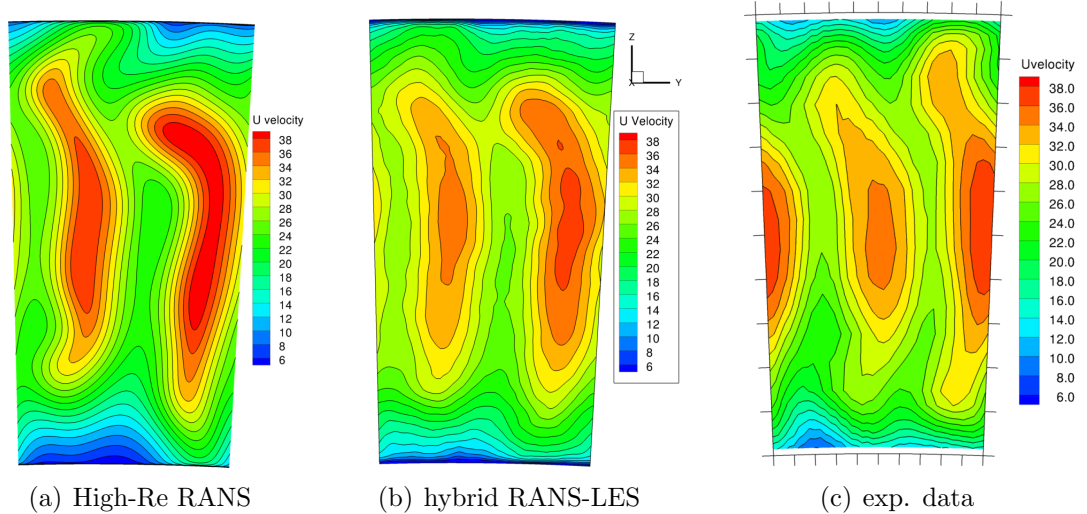
Figure 5.10: Statistical axial velocity contours at the diffuser exit

Table 5.1: the OGV/prediffuser performance data

	C_p	λ
High-Reynolds	0.6457	0.1512
Hybrid RANS/LES	0.6414	0.1581
Exp.	0.66	0.15

The overall system performance from the hybrid RANS/LES prediction compared with high Re RANS and measurements is summarised in Table 5.1. Very similar performance through the OGV is of course predicted by both hybrid RANS/LES and high Re RANS, because in the hybrid method the high Re RANS was applied

in the vane region. The use of a hybrid RANS/LES approach has improved over the "full" LES approach (compared with Table 3.2) and the overall performance figures from the hybrid approach are now very similar to the high Re RANS results. In comparison with the improved ability to predict the flow velocity distribution (see Figure 5.10) this is an encouraging result.

5.2 Hybrid RANS/LES Simulation of An Integrated OGV/Prediffuser Design

The design methodology used to produce the conventional OGV/prediffuser configuration of section 5.1 considers the compressor OGV and the downstream prediffuser essentially in isolation. The OGV is designed to optimise the performance of the compressor stage, and no consideration is given to the downstream secondary flow and diffusion processes experienced by the flow. Likewise, design of the prediffuser is based on information often obtained from experiments without taking specific account of the OGV generated inlet conditions, even though it is widely accepted that the prediffuser performance is sensitive to inlet conditions (Klein [3]). To improve on this, an integrated OGV/prediffuser design methodology was suggested by Barker et al [9], to consider the aerodynamic interactions that occur between compressor OGV and prediffuser systems, and thereby optimise/improve the overall performance of the OGV/prediffuser system. Manipulation of the secondary flow created by the OGV to enable the wakes/endwall boundary layers to 'survive' larger prediffuser area ratios was carried out by adjustment of the OGV shape using 3 OGV and one prediffuser design parameters – blade sweep, blade lean, blade trailing edge recamber, and prediffuser area ratio. The integrated OGV/prediffuser design (with axial blade sweep, trailing edge recamber and a 1.8 diffuser area ratio) that resulted from this investigation has been chosen here as the second test case to examine the performance of the Hybrid RANS/LES method developed in the present thesis.

5.2.1 System Geometry and Mesh

The solution domain for the integrated OGV/prediffuser configuration remained essentially unchanged from that adopted for the conventional configuration, containing 2 OGVs which incorporated the sweep and trailing edge camber changes and an increased area ratio prediffuser (but of the <u>same</u> axial length as in the datum geometry). Changes to the prediffuser area ratio were achieved by altering the inner/outer wall annulus profiles in the geometry file prior to grid generation. Changes to vane sweep and trailing edge camber were made using the parametric capability provided for this in the Rolls-Royce PADRAM software.

As described in section 2.6.2, the vane geometry was read into PADRAM from a geometry file which corresponded to a set of 2D vane aerofoil profiles (point strings) at fixed annulus heights. In order to change the geometry of the OGV, these profiles were manipulated within the PADRAM code either translating axially (to introduce sweep to the blade as illustrated in Figure 5.11 b) or rotating circumferentially (to lean the blade, although this was not adopted in the design chosen), or altered in shape (to recamber the blade trailing edge, see Figure 5.11c). The magnitude of these geometric transformations are controlled via a specified design parameters file, in which radial profiles of lean, sweep and recamber parameters are provided. The usual format is to specify the maximum values of the geometric parameters (e.g. amount of axial sweep) at mid-passage height and the radial profile of this – the procedure adopted in LOPOCOTEP was to use a parabolic radial profile with its maximum value in mid-passage and a zero value at inner/outer walls (see Figure 5.11). Note that when the blade is swept, the blade profiles are moved purely axially, rather than along the chord line. The numbers of nodes and mesh distribution in the hybrid RANS/LES mesh resolution used for the conventional configuration were kept for the integrated configuration.

(a) Datum blade (straight one)

(b) Blade with sweep

(c) Recambered blade

(d) Blade with sweep and recamber
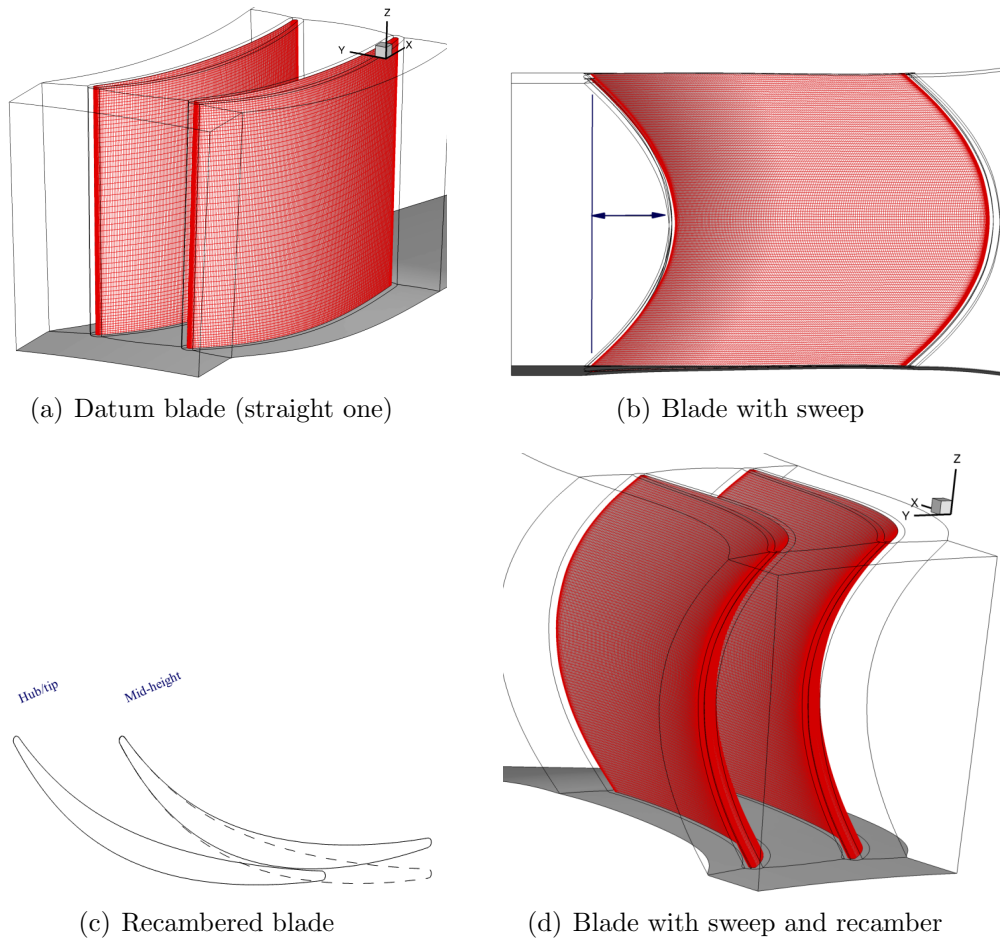
Figure 5.11: Blade with sweep and recamber

5.2.2 Boundary Conditions

As for the conventional OGV/prediffuser configuration, the hybrid RANS/LES calculations for the integrated configuration, were carried out using the same boundary conditions for both RANS and LES computational subdomains.
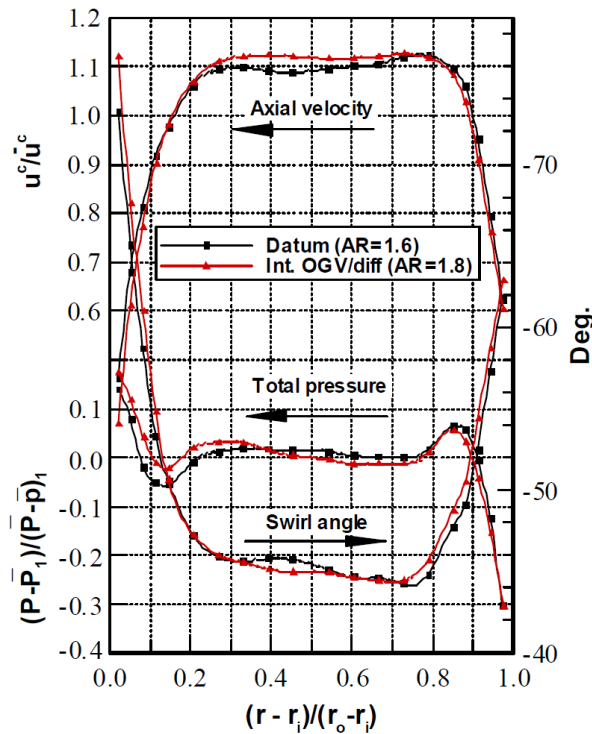
Figure 5.12: Circumferentially averaged profiles at rotor exit/OGV inlet, taken from [9]

For the RANS domain, the same measured 2D profiles of three velocity components were applied at domain inlet, together with the measured radial profiles of k and ϵ as derived from the hotwire measurements [9]. One concern was whether changes to the OGV geometry would invalidate the use of these profiles taken for the conventional vane at rotor exit/OGV inlet. For example, large changes in vane shape will be accompanied by local static pressure field changes which would propagate upstream and might influence the stagnation pressure and flow angle profiles measured in the test rig at rotor exit. Fortunately, in their experimental

study Barker et al [9] checked the measured profiles at rotor exit for both OGV shapes and compared them. It was found ([9]) that the upstream effect of the modification to the OGV blade geometry on the measured profiles was small (see Figure 5.12). This justifies the use of the same inlet conditions as used for the conventional configuration.

For the LES computational domain, R^{2}M was applied to generate spatially and temporally correlated unsteady inflow conditions from the time-averaged RANS solution at OGV exit. Figure 5.13 shows the Reynolds stresses generated by the ASM interfacing technique from the RANS solution. Compared with the datum OGV configuration the integrated OGV design shows a clearly thicker wake and evident aerodynamic off-loading of the vane at hub and tip due to the vane sweep and camber changes with associated thinning of the end wall boundary layers.

5.2.3   Numerical Results

A similar structured approach to analysis of results for the integrated design will be followed as for the conventional design reported in Section 5.1.

Figures 5.14 and 5.15 first present examples of instantaneous axial velocity and vorticity magnitude contours in the interface block and the LES domain (prediffuser) respectively. It can be seen that temporally and spatially correlated unsteady flow is generated from the RANS solution within the interface block which then propagates downstream across the interface. On an instantaneous basis small, very thin negative axial velocity regions are noted in the prediffuser wall boundary layers, which were however not present in the time-mean flow field (see below). The smaller scale vortex regions seen in the interface block grow and decay in magnitude as they are decelerated in the prediffuser.

A check on the acceptability of the size of the interface block was again carried out — the 2-point axial velocity correlation $R_{11}/u^{'2}$ and the longitudinal integral lengthscale L_{11} are shown in Figure 5.16. One test point from the middle of the
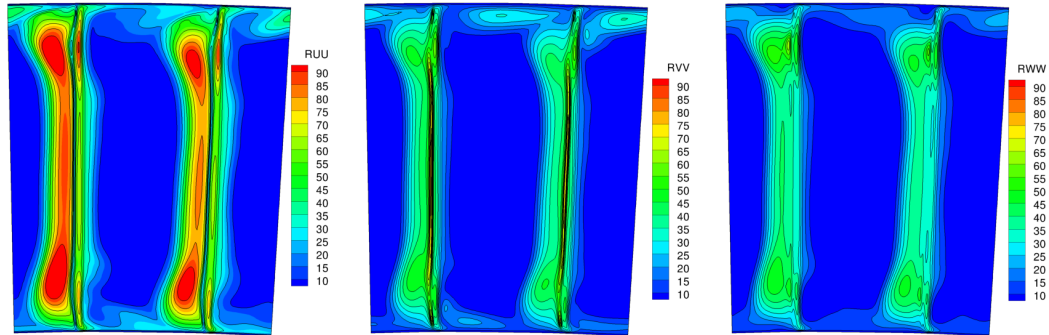
(a) Normal stress (Conventional OGV)
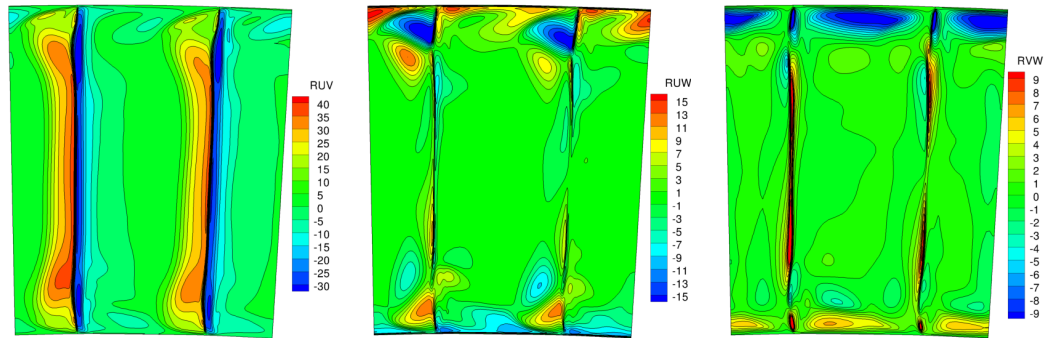
(b) shear stresses (Conventional OGV)
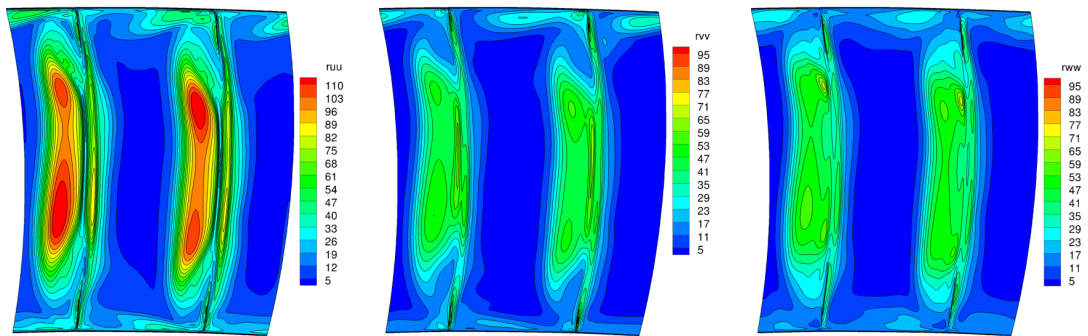
(c) normal stresses (Integrated OGV)
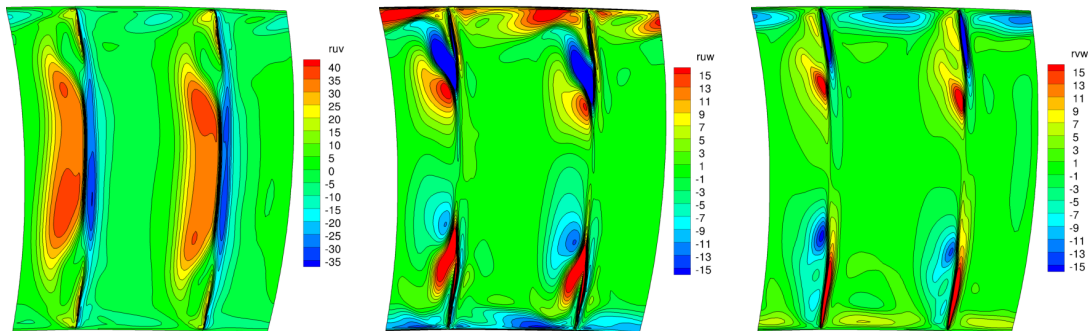
(d) shear stresses (Integrated OGV)

Figure 5.13: Contours of the Reynolds stress components extracted at the RAN/LES interface by the ASM method
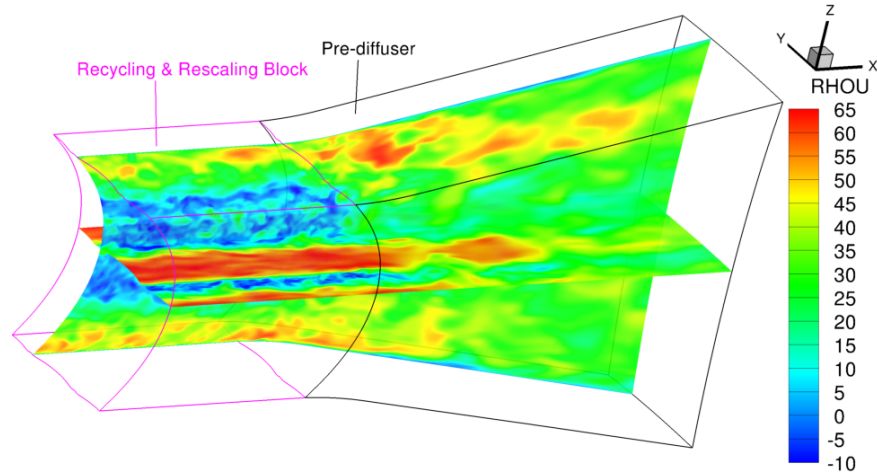
Figure 5.14: Instantaneous axial velocity contours in the diffuser
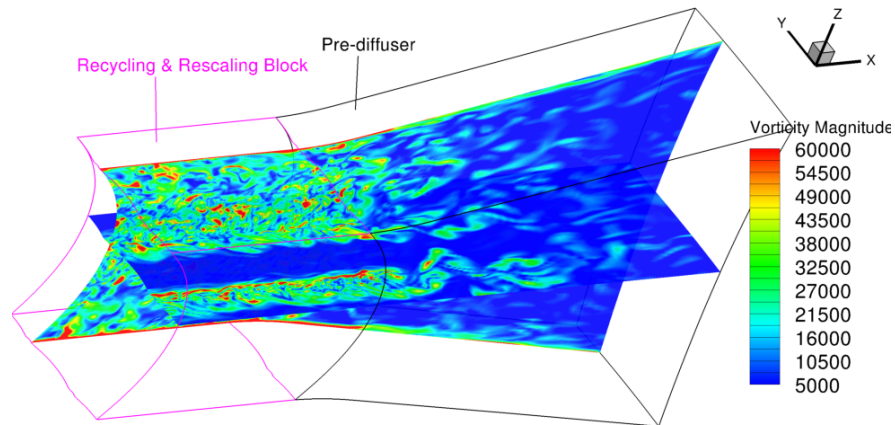
Figure 5.15: Instantaneous vorticity magnitude contours in the diffuser

vane passage and the other at the vane trailing edge at mid span of the outlet guide vanes were chosen. Decorrelation of fluctuations is again observed within half the domain length in the streamwise direction, indicating that the interface block size is acceptable.

Figure 5.17 and 5.18 demonstrate clearly that the wake generated by the vanes propagates smoothly across the interface from the time-averaged RANS domain into the filtered unsteady LES domain (section shown is at mid-span of the vanes). The wakes seem to spread more quickly than in the datum OGV case

146
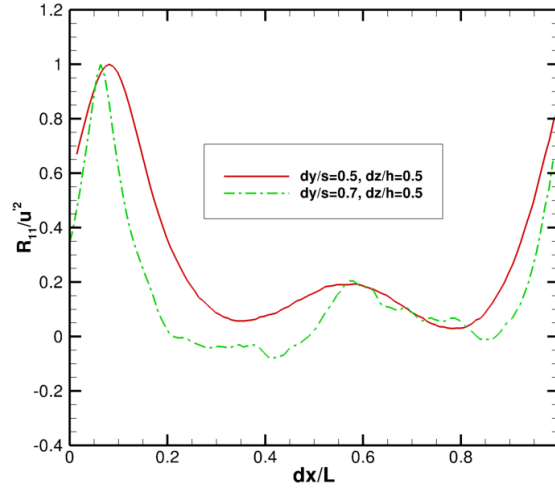
Figure 5.16: two points correlation across the R^{2}M block

(compare with Figures 5.7 and 5.8). The high velocity streaks issuing from each passage only extend $\approx 1/3$rd of the way down the prediffuser, compared to perhaps 60-75% in the conventional system to indicate the more rapid mixing induced by the IOGVs. Partial boundary layer separation from the suction-side blade surface near the trailing edge may be noted in the prediction (Figure 5.17), presumably due to the stronger adverse pressure gradient in the downstream region of the suction surface than was present for the datum vane. Boundary layer separation at the trailing edge leads to a distinctly thicker wake region at the OGV exit, which will represent an increase source of loss in the vane passage.

It is also evident that the two vane wakes develop differently, with the contours from the lower vane (as seen in the orientation shown in Figure 5.18) penetrating further downstream than from the upper vane. This is caused by the different secondary flows generated by the integrated OGV geometry in response to the incoming flow which for one vane (the upper) contains the effects of an upstream IGV wake.

Introduction of sweep leads to a redistribution of the span-wise loading on the vane, generating secondary flows which are strongly different from the two vanes. This is illustrated in Figures 5.19 and 5.20. Higher loading is present near the
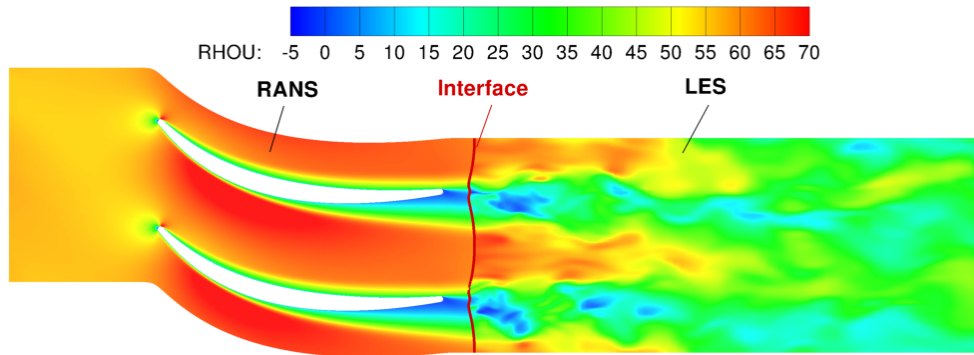
Figure 5.17: Velocity contours of OGV prediffuser : RANS mean velocity to LES instantaneous velocity
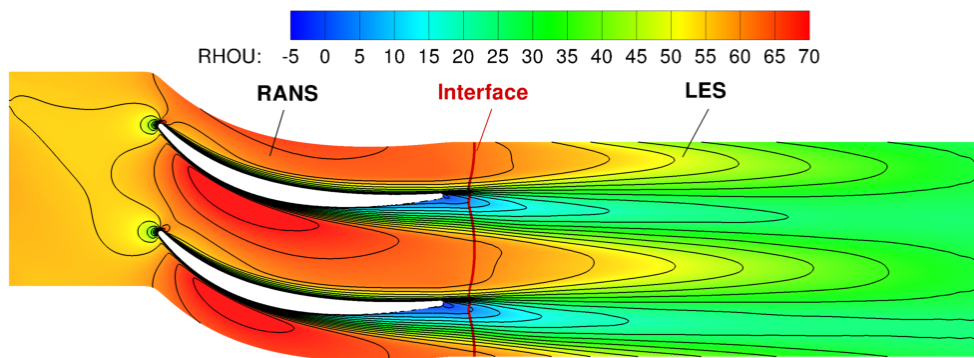
Figure 5.18: Mean velocity contours of OGV(RANS) and diffuser(LES)

midspan region and comparatively lower loading at the tip and hub regions. This reduction of tip loading should result in reduction of tip losses for the swept vane, whilst the secondary flows generated should act to re-energise the prediffuser endwall boundary layers. Very close to the suction side vane surface the presence of small separation zones toward the trailing edge also influence the direction of the secondary flow, as see in the surface streamlines in Figures 5.19 and 5.20.

The predicted development of the OGV-created flowfield as it passes down the prediffuser is captured, and compared with measured data ([9]), in Figure 5.21 – 5.23 in terms of the mean axial velocity component and streanline interpretation of the secondary flow field. At the location closest to OGV exit (22% down the prediffuser, Figure 5.21), the effect of the secondary flow generated by the

(a) Suction side
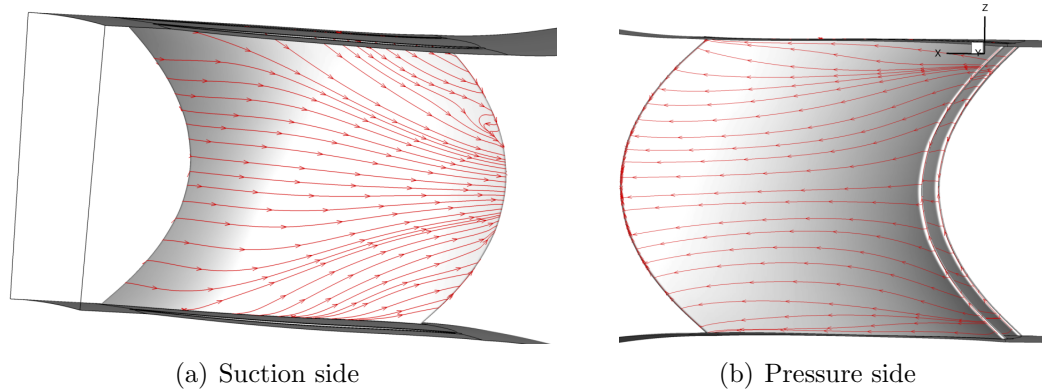
(b) Pressure side

Figure 5.19: Streamlines on the pressure and suction side of vane 1

(a) Suction side
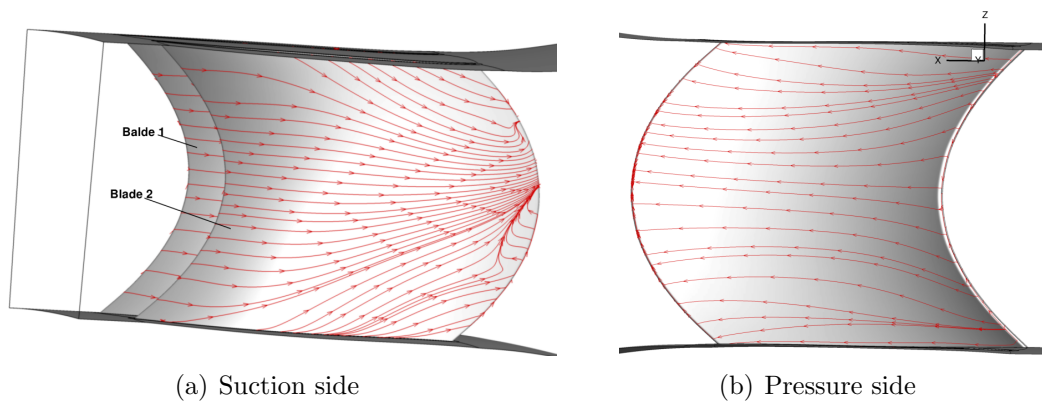
(b) Pressure side

Figure 5.20: Streamlines on the pressure and suction side of vane 2

integrated design shows a very different contour shape compared to the datum design (see Figure 3.47). The wake regions show evidence of two 'pinched off' zones at hub and tip caused by the strong OGV-driven secondary flow which acts to drive flow from the core of the passage towards both endwalls. The feature is also clearly evident in the measured data although weaker than predicted. The wakes are predicted to be thicker than measured, undoubtedly caused by the presence in the predictions of boundary layer separation on the vane suction side near the trailing edge, particularly visible for the left hand vane in Figure 5.21. The endwall flow re-energisation seems also to be stronger in predictions than experiments as the endwall boundary layers are thinner than measured, although the trend is certainly correct. At the second location (44% down the prediffuser,

(a) Predicted axial velocity contours

(b) Predicted secondary flow vectors and stream lines

(c) Measured axial velocity contours

(d) Measured secondary flow vectors and stream lines
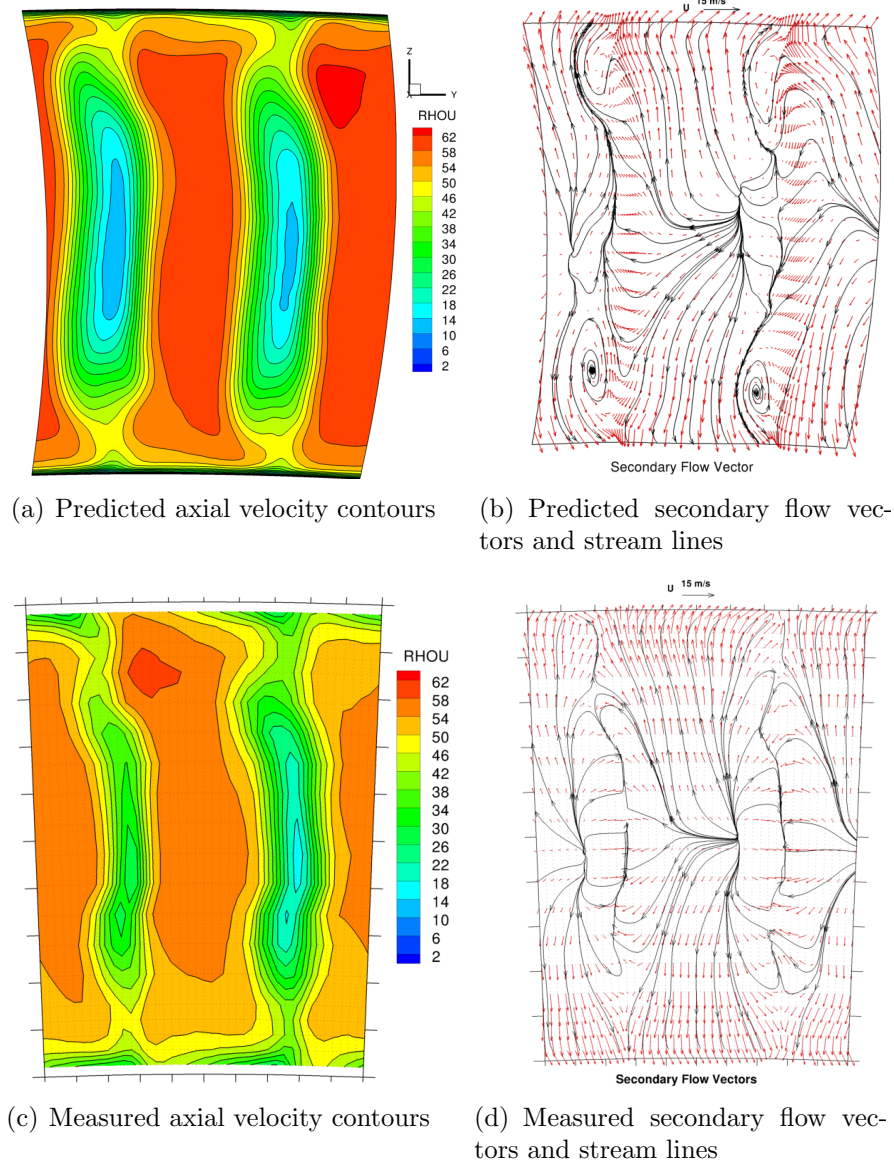
Figure 5.21: Axial velocity contours, secondary flow vectors and stream lines at the position of x/L=22%

Figure 5.22) the predicted high axial velocity contour shapes show evidence of two bulges near inner/outer end walls, which is a feature also observed in the experiment. The thicker vane wakes in the predictions has caused the two velocity regions to be displaced circumferentially more than seen in the measured data. Finally, at prediffuser exit (100%, Figure 5.23) the two high velocity regions are

(a) Predicted axial velocity contours

(b) Predicted secondary flow vectors

(c) Measured axial velocity contours

(d) Measured secondary flow vectors
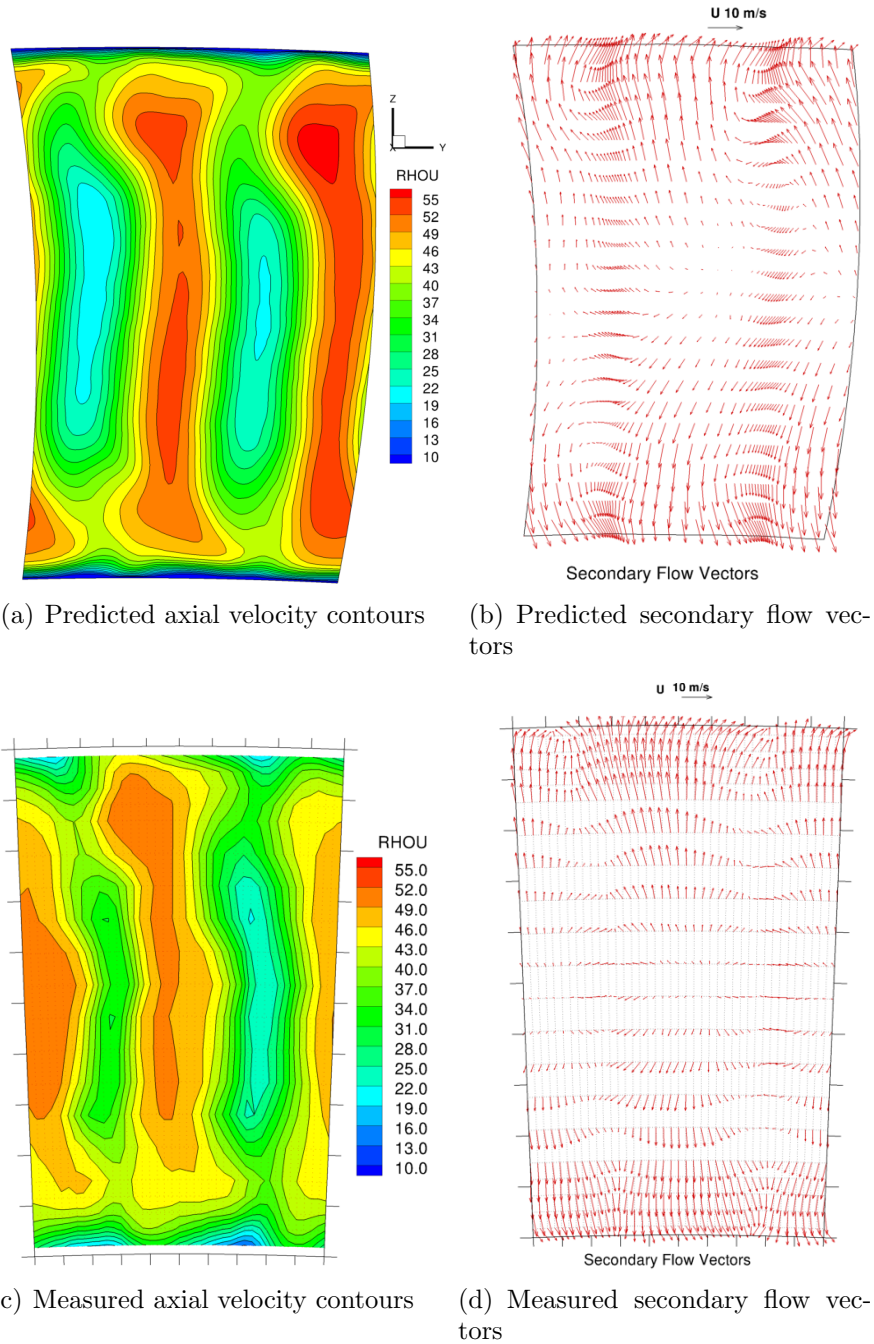
Figure 5.22: Axial velocity contours and secondary flow vectors at the position of x/L=44%
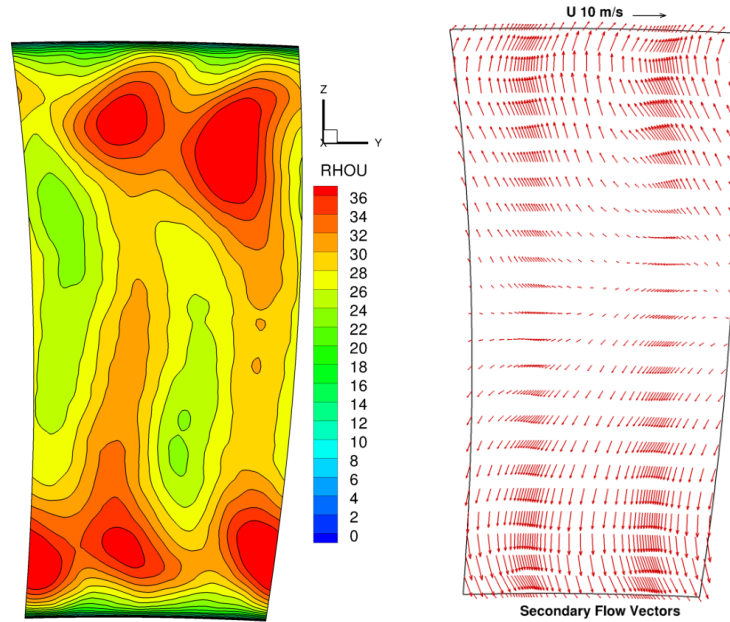
(a) Predicted axial velocity contours

(b) Predicted secondary flow vectors
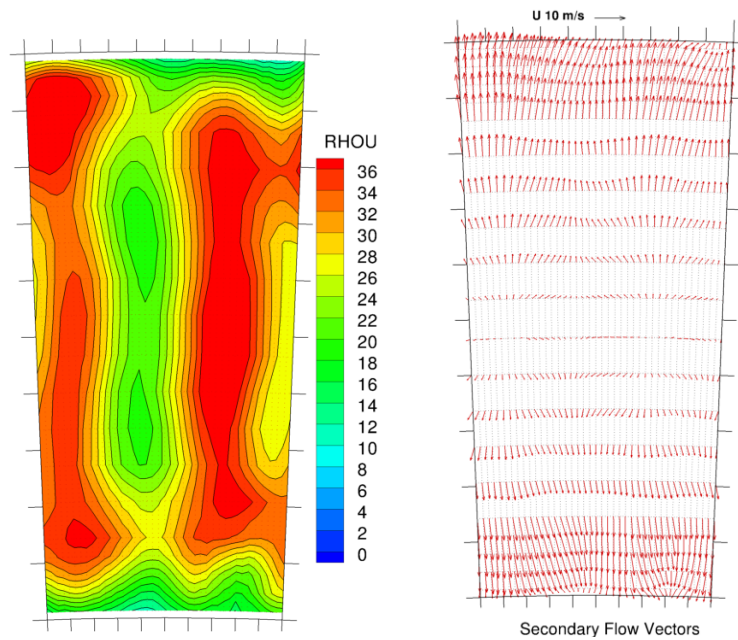
(c) Measured axial velocity contours

(d) Measured secondary flow vectors

Figure 5.23: Axial velocity contours and secondary flow vectors at prediffuser exit (x/L=100%)

predicted to join together as the 'bulge' zones merge, this is also happening in the measurements, although at a slower rate.

Finally, Table 5.2 shows the overall system performance from both hybrid RANS/LES predictions and measurements for the integral OGV configuration (the conventional OGV design hybrid predictions and experiments are also shown for comparison). The hybrid prediction has captured the trend of an increase in λ and an increase in C_p when moving form the conventional OGV to the IOGV design, with a qualitatively good assessment of the magnitude of the change. Of course, even though λ has increased for the OGV/prediffuser, the reduction in bulk mean velocity achieved with IOGV higher area ratio (see higher C_p) means that the dump loss will be reduced, so the overall performance is a gain.

Table 5.2: the OGV/prediffuser performance data

	C_p	λ
IOGV Hybrid RANS/LES	0.6696	0.1807
IOGV Exp.	0.69	0.18
Conventional OGV Hybrid RANS/LES	0.6414	0.1581
Conventional Exp.	0.66	0.15

Chapter 6

Summary, Conclusions and Future Work

6.1 Summary and Conclusions

In the gas turbine engine, the OGV/prediffuser combination is key to achieve a good design for combustor external aerodynamics [3]. Since the flow includes 3D turbulent wakes and boundary layers in adverse pressure gradients with the possibility of flow separation, the OGV/prediffuser combination offers significant turbulence modelling challenges for CFD. In order to understand the optimum approach for modelling turbulence in this important sub-component of compressor/combustor interaction, comparisons between various turbulence modelling approaches (RANS, LES, and Hybrid RANS/LES) for the OGV/prediffuser flow have been carried out and validated against the benchmark experimental data of [9]. This was accomplished in three stages.

In the first stage, numerical studies of a conventionally designed OGV/prediffuser configuration (with straight vanes and a 1.6 area ratio prediffuser) using two RANS turbulence models were carried out and analysed. Both high and low Reynolds number $k - \epsilon$ turbulence models were applied together with experimentally determined inlet conditions, 2D (radial/azimuthal) velocity contours and 1D (radial) k and ϵ profiles. The calculations were compared with detailed experimental data from the LOPOCOTEP[9] project. The results showed: both

RANS models gave a reasonable representation of the flow development in both the OGV and prediffuser compared with the measured data. With respect to the turbulence models, the use of the higher fidelity low Re model did produce some small but identifiable differences in the mean velocity predictions compared to the high Re model; however, the predicted overall performance coefficients were better with the high Re model. This provides good justification for the adoption of a high Re model in CFD-based optimisation of OGV/prediffuser system. The probable cause of poor low Re model performance was its inability to capture the return to turbulent flow in the relaminarised boundary layer on the vane suction surface. On the basis of the evidence in the present RANS study, it seems a low Re model does not offer sufficient benefits.

In the second stage, LES prediction of the OGV/prediffuser flow was investigated. In this 'full' LES application, in order to generate spatially and temporally correlated unsteady inlet conditions, the modified Recycling and Rescaling Method (R^2M) reported by Xiao el al [93] for generating unsteady inflow conditions from specified mean statistics and turbulence normal stresses was developed to be applicable to a rotor exit/OGV inlet plane; and LES predictions using both the R^2M technique and a crude white noise perturbation for unsteady inlet condition generation were carried out, compared and validated against measurements. Two methods of implementing the R^2M technique were studied: the first (method A) was modified and developed from the method used by Lund et al [90] and Xiao et al [93] involving only recycling and rescaling; the second (method B) was developed by combining recycling and rescaling with a variant of the method of Pierce and Moin [82][83] to use source term forcing. The particular source term forcing adopted was to specify these such that they removed the effects of any mean pressure gradients in the momentum equations, leaving just the rescaling technique to drive the flow field. Results and comparison between the two methods showed that method B was clearly superior in its ability to produce accurate distribution of all three mean velocity components and rms profiles compared to method A, and is appropriate for generating LES unsteady inflow from pre-specified turbulence statistics.

Using the method B approach for R²M, 'full' LES calculations were carried out and compared with an LES calculation driven by simple white noise inlet perturbations. The R²M driven LES predicted much more physically correct turbulence structures in the inlet flow; only clearly uncorrelated structures that decayed very quickly were generated by the white noise predictions. Further downstream the disappearance of the generated inlet turbulence, even in the R²M predictions, was due to the strong acceleration (relaminarisation) over the OGV aerofoil. Although turbulence reappeared further down the vane surface (it re-appeared earlier in the R²M solution), the complexity of this flow physics seemed to provide two challenges for the mesh and simple SGS model used in the present LES. Observation and analysis of the LES predicted statistical solutions showed partial flow separation of the OGV suction side boundary layer. This is probably caused by the presence of relaminarisation and subsequent too slow reappearance of turbulence on the suction side OGV boundary layer. If the turbulence does not re-appear quickly enough, the laminar-like boundary layer will certainly separate in the strong adverse pressure gradient on the rear of the vane. Whether such a separation zone exists in practice is not known (although unlikely), but the complex flow processes observed on the suction side surface probably demand further LES near wall mesh refinement, as well as perhaps a more advanced LES sub grid scale model than used here.

Finally, a zonal hybrid RANS/LES approach for the OGV/prediffuser flow problem was investigated and validated for both conventional (datum straight vanes with 1.6 area ratio prediffuser) and integrated geometries (swept vane, trailing edge recamber and 1.8 area ratio prediffuser). RANS CFD was applied to the OGV region and LES CFD was used in the prediffuser. To allow the two different flow solvers to communicate through the RANS/LES interface, an interface technique was developed. This used an 'adaptor' methodology based on an algebraic stress model to extract more accurate distributions of <u>individual</u> Reynolds normal stresses from an eddy viscosity RANS solution. These were then input together with the RANS mean velocity solution to the LES R²M virtual interface block as target values to generate unsteady inlet flow for the LES domain.

The zonal hybrid RANS/LES solutions demonstrated successful communication of the flow solvers at the interface and that the 3D flow features and turbulent kinetic energy were transfered properly from the upstream RANS flow solver to the downstream LES domain. The wakes propagated correctly across the RANS/LES interface. The results and analysis showed that compared to RANS and LES approaches, the Hybrid RANS/LES approach was able to provide good predictions of OGV/prediffuser flow in that it provided overall performance coefficients as well as the RANS only approach, but gave velocity field predictions at prediffuser exit that were closer to measured values even for the complex 3D integrated vanes. It is believed to offer an optimum approach for OGV/prediffuser flow simulation considering both accuracy and cost. To demonstrate this, the hybrid approach was applied to an integrated design and showed good predictions of the changes to the flow field structure brought about by the vane geometry changes, and good agreement with measured changes in C_p and λ loss coefficients.

6.2   Recommendations for Future Work

Recommendations for further work forthcoming from this study can be separated into three main areas:

Firstly, for the current 'full' LES study, the simple Smagorinsky model (with some near-wall damping) was adopted. It is evident from the results presented here that the OGV suction surface near wall complex flow behaviour demands use of a more advanced approach to SGS modelling which may also include near wall mesh refinement. Models such as the dynamic kinetic energy subgrid-scale model (as proposed by Kim [120]) should be explored to allow the subgrid-scale turbulence in flows which involve relaminarisation and return to turbulence to be captured accurately by solving a transport equation for the subgrid-scale turbulence kinetic energy.

Secondly, for hybrid RANS/LES simulations, an improvement in the choice of

the RANS turbulence model (in the OGV region) should be explored. The best candidate may be Reynolds-stress models, which can be successful in calculating flows with significant mean streamline curvature and flows with strong swirl or secondary flows [12], although perhaps an eddy viscosity model known to perform well for boundary layer in adverse pressure gradients could be explored (e.g. $k - \omega$).

Finally, the zonal hybrid RANS/LES approach used in the present study is a coupling between a steady RANS solver and an LES solver. A better capture of the flow physics would be made possible by adopting an URANS/LES combination. One improvement which could then be achieved were if better experimental measurements could be made of the rotor exit flow used as inlet conditions in the present study. Firstly, 2D measurements of turbulence quantities to match the 2D mean flowfield data would be more consistent than the current practice. This would require use of optical techniques such as PIV. Secondly, if these measurements (as well as for the mean velocity) could be made time-resolved then the influence of the unsteady blade-passing frequency calculation would be introduced and computationally modelled by the the URANS treatment. This has been ignored in the present work and may influence the leading edge OGV flow. If the experimental data were not available, the alternative would be to include the rotor stage in the calculation, which would also require a URANS approach (inlet conditions to the IGV are much simpler and readily available). Future improvements to this would also include modification to the communication between the URANS and LES solutions to make sure both solvers can communicate and run simultaneously.

Bibliography

[1] G. Boudier, L.Y.M. Gicquel, T. Poinsot, D. Bissières, and C. Bérat. Comparison of LES, RANS and experiments in an aeronautical gas turbine combustion chamber. *Proceedings of the Combustion Institute*, 31:3075–3082–506, 2007. vii, 3, 4

[2] J. U. Schlüter, X. Wu, S. Kim, S. Shankaran, J. J. Alonso, and H. Pitsch. A framework for coupling Reynolds-averaged with large-eddy simulations for gas turbine applications. *ASME Journal of Fluids Engineering*, 127(4):806–815, 2005. vii, 4, 5, 31, 32

[3] A. Klein. Characteristics of combustor diffusers. *Progress in Aerospace Sciences*, 31(3):171–271, 1995. vii, 7, 8, 9, 11, 12, 140, 154

[4] A.G. Barker and J.F. Carrotte. Influence of compressor exit conditions on combustor annular diffusers, part 1: Diffuser performance. *AIAA Journal of Propulsion and Power*, 17(3):678–686, 2001. vii, 13, 14

[5] D.C. Wilcox. *Turbulence Modeling for CFD*. DCW Industries, La Cañada, California, 1993. vii, 18, 50

[6] U. Piomelli and E. Balaras. Wall-layer models for large eddy simulations. *Ann. Rev. Fluid Mech.*, 34:376–404, 2002. vii, 20, 21, 102

[7] P. Batten, U. C. Goldberg, and S. R. Chakravarthy. LNS – an approach towards embedded LES. *AIAA Paper 2002-0427*, 2002. vii, 24, 27, 89

[8] J. Fröhlich and D. von Terzi. Hybrid LES/RANS methods for the simulation of turbulent flows. *Progress in Aerospace Sciences*, 44(5):349–377, 2008. vii, 29

[9] A. G. Barker, J. F. Carrotte, J. Luff, and J. J. McGuirk. Design of an integrated OGV/diffuser system. Technical Report TT03R01, EU FP5 project GRID1-2000-25062: LOPOCOTEP, 2003. viii, x, 13, 14, 15, 38, 39, 42, 49, 53, 61, 62, 63, 64, 65, 84, 86, 92, 140, 143, 144, 148, 154

[10] Y.B. Suzen and P.G. Huang. Numerical simulation of unsteady wake/blade interactions in low-pressure turbine flows using an intermittency transport equation. *ASME Journal of Turbomachinery*, 127(7):431–444, 2005. 2

[11] D. J. Dorney and H.C. Flitan et al. Effects of blade count on boundary layer development in a low-pressure turbine. *AIAA-2000-0742*, 2000. 2

[12] S. B. Pope. *Turbulent Flows*. Cambridge University Press, Cambridge, UK, 2000. 3, 17, 18, 47, 50, 100, 124, 158

[13] J. Yao, A. Jameson, J. J. Alonso, and F. Liu. Development and validation of a massively parallel flow solver for turbomachinery flows. In *Proc. of 38th Aerospace Sciences Meeting and Exhibit, Reno, NV, AIAA-2000-0882*, Jan. 2000. 3

[14] R. L. Davis and J. Yao et al. Unsteady interaction between a transonic turbine stage and downstream components. *International Journal of Rotating Machinery*, 10(6):495–506, 2004. 3

[15] B. Janus, A. Dreizler, and J. Janicka. Flow field and structure of swirl stabilized non-premixed natural gas flames at elevated pressure. In *Proc. of ASME Turbo Expo 2004: Power for Land, Sea and Air, Vienna, Austria, ASME-GT2004-53340*, Jun. 2004. 3

[16] F. di Mare, W. P. Jones, and K. R. Menzies. Large eddy simulation of a model gas turbine combustor. *Combustion and Flame*, 137:278–294, 2004. 3

[17] P. Sagaut. *Large Eddy Simulation for Incompressible Flows : an Introduction.* Springer, Berlin ; London, 2002. 3, 102

[18] C. D. Pierce and P. Moin. Progress-variable approach for large-eddy simulation of turbulent non-premixed combustion. *Journal of Fluid Mech.*, 504:73–97, 2004. 3

[19] W. W. Kim and S. Syed. Large-eddy simulation needs for gas-turbine combustor design. In *Proc. of 40th Aerospace Sciences Meeting and Exhibit, Reno, NV, AIAA-2004-0331*, Jan. 2004. 3

[20] H. Mongia. Recent advances in the development of combustor design tools. *AIAA-2003-4495*, 2003. 3

[21] P. Moin and S. Apte. Large-eddy simulation of realistic gas turbine combustors. *AIAA-2004-0330*, Jan. 2004. 3

[22] J. U. Schlüter, S. Shankaran, S. Kim, H. Pitsch, J. J. Alonso, and P. Moin. Towards multi-component analysis of gas turbines by CFD: Integration of RANS and LES flow solvers. In *Proc. of ASME Turbo Expo 2003, Atlanta, ASME GT2003-38350*, Jun. 2003. 4, 15, 29, 31, 32

[23] J. U. Schlüter, H. Pitsch, and P. Moin. Large eddy simulation inflow conditions for coupling with Reynolds-averaged flow solvers. *AIAA J.*, Vol.42(3):478–484, 2004. 4, 89, 119

[24] J. U. Schlüter, H. Pitsch, and P. Moin. Outflow conditions for integrated large eddy simulation/Reynolds-Averaged Navier-Stokes simulations. *AIAA J.*, Vol.43(1):156–164, 2004. 4, 29, 31, 32

[25] J. U. Schlüter, X. Wu, S. Kim, J. J. Alonso, and H. Pitsch. Coupled RANS-LES computation of a compressor and combustor in a gas turbine engine. In *Proc. of 40th AIAA/ASME/SAE/ASEE Joint Propulsion Conference and Exhibit, AIAA 2004-3417*, Jul. 2004. 4

[26] G. Medic, G. Kalitzin, D. You, E.v.d. Weide, J.J. Alonso, and H. Pitsch. Integrated RANS/LES computations of an entire gas turbine jet engine. In

Proc. of 45th AIAA Aerospace Sciences Meeting and Exhibit, Reno, Nevada USA, AIAA-2007-1117, Jan. 2007. 4

[27] F. Hamba. A hybrid RANS/LES simulation of turbulent channel flow. *Theoret. Comput. Fluid Dynamics*, 16(3):387–403, 2003. 5

[28] N. J. Georgiadis, J. I. D. Alexander, and E. Reshotko. Hybrid Reynolds-Averaged Navier-Stokes/Large-Eddy simulations of supersonic turbulent mixing. *AIAA Journal*, 41(2):218–229, 2003. 5

[29] C. R. Fishenden and S. J. Stevens. The performance of annular combustor dump diffusers. *AIAA Journal of Aircraft*, 10:61–67, 1977. 7, 10, 11

[30] K.C. Karki, V.L. Oechsle, and H.C. Mongia. A computational procedure for diffuser-combustor flow interaction analysis. In *Proc. of 35th IGTI Symposium, Brussels, Belgium, ASME 90-GT-35*, 1990. 11

[31] P. Koutmos and J.J. McGuirk. Numerical calculations of the flow in annular combustor dump diffuser geometries. *Proc. Inst. Mech. Engrs*, 203:319–331, 1989. 11

[32] W. Shyy. A numerical study of annular dump diffuser flows. *Computational Method In Applied Mechanics and Engineering*, 53:47–65, 1985. 11

[33] S.J. Stevens, U.S.L. Nayak, J.F. Preston, P.J. Robinson, and C.T.J. Scrivener. Influence of compressor exit conditions on diffuser performance. *AIAA Journal of Aircraft*, 15(8):482–488, 1978. 11, 12

[34] S.J. Stevens and G.J. Williams. The influence of inlet conditions on the performance of annular diffusers. *ASME Journal of Fluid Engineering*, 102:357–363, 1980. 11, 12

[35] S.J. Stevens, S.P. Harasgama, and A.P. Wray. Influence of blade wakes on the performance of combustor shortened prediffusers. *AIAA Journal of Aircraft*, 21(9):641–648, 1984. 12

[36] T. Zierer. Experimental investigation of the flow in diffusers behind an axial flow compressor. *ASME paper 93-GT-347*, 1993. 13

[37] A.G. Barker and J.F. Carrotte. Influence of compressor exit conditions on combustor annular diffusers, part ii: Flow redistribution. *AIAA Journal of Propulsion and Power*, 17(3):687–694, 2001. 13

[38] A.G. Barker and J.F. Carrotte. Compressor exit conditions and their impact in flametube injector flows. *ASME Journal of Engineering for Gas Turbines and Power*, 124:10–19, 2002. 13

[39] A. D. Walker, J. F. Carrotte, and J. J. McGuirk. Enhanced external aerodynamic performance of a generic combustor using an integrated ogv/prediffuser design technique. *ASME Journal of Engineering for Gas Turbines and Power*, 129(1):80–87, 2007. 13, 14

[40] J. Wang, C. H. Priddin, and J. J. McGuirk. CFD - based automatic optimisation of flow interactions in combustor ogv/pre-diffuser systems. *Submitted to ASME Journal of Fluids Engineering*, 2012. 14

[41] S. Shahpar. SOPHY: An integrated CFD based automatic design optimisation system. In *Proc. of ISOABE Conf. Munich, Germany, ISABE-2005-1086*, 2005. 14

[42] P. K. Kundu and I. M. Cohen. *Fluid Mechanics*. Academic Press, London,UK, 2002. 17

[43] J.O. Hinze. *Turbulence, An Introduction to its Mechanism and Theory*. McGraw Hill, New York, 1959. 17

[44] P. Sagaut, S. Deck, and M. Terracol. *Multiscale and Multiresolution Approaches in Turbulence*. Imperial College Press, london, 2006. 17, 22, 28, 29, 118

[45] J. Blazek. *Computational Fluid Dynamics : Principles and Applications*. Elsevier, Amsterdam ; London, 2005. 18, 43

[46] O. Reynolds. On the dynamical theory of incompressible viscous fluids and the determination of the criterion. *Philosophical Transactions of the Royal Society*, 186:123–164, 1895. 18

[47] J. Boussinesq. Theorie de l'écoulement tourbillant. *Mém. Prés. par div. savant a lacad. Sci. Paris*, 23:46–55, 1877. 18, 43

[48] L. Prandtl. Bericht *ü*ber Untersuchungen zur ausgebildeten Turbulenz. *Z. Angew. Math. Mech.*, 5:136–139, 1925. 18

[49] L. Prandtl. Ueber ein neues Formelsystem fur die ausgebildete Turbulenz. *Nach. Ges. Wiss. Gottingen, Math.-Phys.*, pages 6–18, 1945. 18

[50] A.N. Kolmogorov. The equations of turbulent motion in an incompressible fluid. *Izv. Akad. Nauk. SSSR, Ser. Phys.*, 6:56–58, 1942. 18

[51] W. P. Jones and B. E. Launder. The prediction of laminarisation with a two-equation model of turbulence. *International Journal of Heat and Mass Transfer*, 15(2):301, 1972. 18, 44, 45

[52] C.P. Donaldson and H. Rosenbaum. Calculation of the turbulent shear flows through closure of the Reynolds equations by invariant modeling. *Aeronautical Research Associates of Princeton*, ARAP Report No. 127, 1968. 18

[53] B.E. Launder, G.J. Reece, and Rodi W. Progress in the development of a Reynolds-stress turbulence closure. *Journal of Fluid Mechanics*, 68:537–566, 1975. 18

[54] B. Lakshminarayana. Turbulence modelling for complex shear flows. *AIAA Journal*, 24:1900–1917, 1986. 18

[55] D. R. Chapman. Computational aerodynamics development and outlook. *AIAA Journal*, 17:1293–1313, 1979. 20

[56] W. C. Reynolds. *The potential and limitation of direct and large eddy simulations*. In "Whither Turbulence? Turbulence at the Crossroads" pp:313-342, Heidelberg: Springer, 1990. 20

[57] D.A. Von Terzi and J. Fröhlich. Coupling conditions for LES with downstream RANS for prediction of incompressible turbulent flows. In *Proceedings of the 5th international symposium on turbulence and shear flow phenomena, Vol. 2*, pages 765–770. Elsevier, 2007. 21, 29

[58] P. Batten, U. C. Goldberg, and S. R. Chakravarthy. Subgrid turbulence modeling for unsteady flow with acoustic resonance. In *Proc. of 38th Aerospace Sciences Meeting, Reno, NV, AIAA-2000-0473*, 2000. 23

[59] C. G. Speziale. Computing non-equilibrium flows with time-dependent RANS and VLES. In *Proc. of 15th International Conference on Numerical Methods in Fluid Dynamics*, volume 490, pages 123–129. Springer Berlin / Heidelberg, 1997. 23

[60] U. Schumann. Subgrid scale model for finite difference simulations of turbulent flows in plane channels and annuli. *Journal of Computational Physics*, Vol. 18:376–404, 1975. 24

[61] J. S. Baggett. On the feasibility of merging LES with RANS for the near-wall region of attached turbulent flows. In *Proc. of Annual Research Briefs 1998, Center for Turbulence Research*, pages 267–277, 1998. 24

[62] T.C. Fan, M. Tian, J.R. Edwards, H.A. Hassan, and R.A. Baurle. Validation of a hybrid Reynolds-Averaged/Large-Eddy simulation method for simulating cavity flameholder configurations. In *Proc. of 31st AIAA Fluid Dynamics Conference and Exhibit, AIAA-2001-2929*, Jun. 2001. 25

[63] C.C. Fan, X. Xiao, J. R. Edwards, H. A. Hassan, and R.A. Baurle. Hybrid Large-Eddy/Reynolds-Averaged Navier-Stokes simulations of shock-separated flows. *AIAA Journal of Spacecraft and Rockets*, 41(6):897–906, 2004. 25

[64] F.R. Menter. Two-equation eddy viscosity turbulence models for engineering applications. *AIAA J*, Vol. 32(8):1598–605, 1994. 25

[65] X. Xiao, J. R. Edwards, and H. A. Hassan. Blending function in hybrid Large-Eddy/Reynolds-Averaged Navier-Stokes simulations. *AIAA Journal*, 42(12):2508–2515, 2004. 25

[66] T.C. Fan, M. Tian, J.R. Edwards, H.A. Hassan, and R.A. Baurle. Hybrid LES/RANS simulation of a shock wave/boundary layer interaction. In *Proc.*

of 40th AIAA Aerospace Science Meeting and Exhibit, AIAA 02-0431, Jan. 2002. 25

[67] P. R. Spalart. Detached eddy simulation. *Ann. Rev. Fluid Mech.*, 41:181–202, 2009. 26, 27

[68] P.R. Spalart, W.H. Jou, M. Strelets, and S.R. Allmaras. *Comments on The Feasibility of LES for Wings, and on a Hybrid RANS/LES Approach.* Advances in DNS/LES. Greyden Press, 1997. 26, 27

[69] P.R. Spalart and S.R. Allmaras. A one-equation turbulence model for aerodynamic flows. In *Proc. of AIAA, 30th Aerospace Sciences Meeting and Exhibit, Reno, NV, AIAA-1992-0439*, page 23, Jan. 1992. 26

[70] P.R. Spalart and S.R. Allmaras. A new version of detached eddy simulation, resistant to ambiguous grid densities. *La Recherche Aérospatiale*, 5(21), 1994. 26

[71] A. Travin, M. Shur, M. Strelets, and P. Spalart. Detached eddy simulations past a circular cylinder. *Flow, Turbulence and Combustion*, 63(1):293–313, 2000. 26, 27

[72] P. Spalart, S. Deck, M. Shur, K. Squires, M. Strelets, and A. Travin. A new version of detached eddy simulation, resistant to ambiguous grid densities. *Theoretical and Computational Fluid Dynamics*, 20(3):181–195, 2006. 27

[73] J. Forsythe, K. Hoffman, and K.D. Squires. Detached eddy simulation with compressibility corrections applied to a supersonic axisymmetric base flow. *AIAA-2002-0586*, 2002. 27

[74] D. A. von Terzi, C. Hinterberger, M. García-Villalba, J. Fröhlich, W. Rodi, and I. Mary. LES with downstream RANS for flow over periodic hills and a model combustor flow. In *EUROMECH Colloquium 469, Large Eddy Simulation of Complex Flows, TU Dresden, Germany*, Oct. 2005. 29

[75] D. von Terzi, I. Mary, and J. Fröhlich. Segregated LES/RANS coupling conditions for the simulation of complex turbulent flows. In *Proc. of Numerical*

Simulation of Turbulent Flows and Noise Generation, Notes on Numerical Fluid Mechanics and Multidisciplinary Design, volume 104, pages 231–252. Springer, 2009. 29

[76] P. Quéméré and P. Sagaut. Zonal multi-domain RANS/LES simulations of turbulent flows. *International Journal for Numerical Methods in Fluids*, 40(7):903–925, 2002. 29

[77] A. Akselvoll and P. Moin. Large-eddy simulation of turbulent confined coannular jets. *Journal of Fluid Mechanics*, 315:387–411, 1996. 31

[78] H.J. Kaltenbach, M. Fatica, R. Mittal, T.S. Lund, and P. Moin. Study of flow in a planar asymmetric diffuser using large-eddy simulation. *Journal of Fluid Mechanics*, 390:151–185, 1999. 31

[79] A. Spille-Kohoff and H. J. Kaltenbach. Generation of turbulent inflow data with a prescribed shear-stress profile. In C. Liu, L. Sakell, and T. Beutner, editors, *Proc. of DNS/LES Progress and Challenges, Third AFOSR International Conference on DNS/LES, Arlington,TX*, Aug. 2001. 33

[80] A. Keating, U. Piomelli, E. Balaras, and H.J. Kaltenbach. A priori and a posteriori tests of inflow conditions for large-eddy simulation. *Physics of Fluids*, 16(12):4696–4712, 2004. 33

[81] A. Keating, G. De Prisco, and U. Piomelli. Interface conditions for hybrid RANS/LES calculations. *International Journal of Heat and Fluid Flow*, 27(5):777, 2006. 33

[82] C. D. Pierce and P. Moin. Method for generating equilibrium swirling inflow conditions. *AIAA Journal*, 36(7):1325–, 1998. 33, 34, 53, 89, 94, 155

[83] C.D. Pierce. *Progress-variable approach for large-eddy simulation of turbulent combustion*. PhD thesis, Stanford university, Department of Mechanical Engineering, 2001. 34, 53, 89, 155

[84] P. Batten, U. C. Goldberg, and S. R. Chakravarthy. Interfacing statistical turbulence closures with large-eddy simulation. *AIAA Journal*, 42(3):485–, 2004. 35

[85] P. Druault, S. Lardeau, J.P. Bonnet, F. Coiffet, J. Deville, and E. Lamballais. Generation of three-dimensional turbulent inlet conditions for large-eddy simulation. *AIAA Journal*, 42(3):447–456, 2004. 35

[86] I. Veloudis, Z. Yang, J. J. McGuirk, G. J. Page, and A. Spencer. Novel implementation and assessment of a digital filter based approach for the generation of LES inlet conditions. *Flow Turbulence Combust*, 79:1–24, 2007. 35, 42, 51, 89

[87] M. Klein, A. Sadiki, and J. Janicka. A digital filter based generation of inflow data for spatially developing direct numerical or large eddy simulation. *Journal of Computational Physics*, 16:652–665, 2003. 35

[88] P.R. Spalart. Direct simulation of a turbulent boundary layer up to $re_\theta = 1410$. *J. Fluid Mech.*, 187:61–, 1988. 35, 92

[89] P.R. Spalart. Numerical study of sink-flow boundary layers. *J. Fluid Mech.*, 172:307–, 1986. 35

[90] T. S. Lund, X. Wu, and K. D. Squires. Generation of turbulent inflow data for spatially-developing boundary layer simulation. *Journal of Computational Physics*, 140:233–258, 1998. 35, 36, 39, 53, 89, 92, 155

[91] S. Stolz and N.A. Adams. Large-eddy simulation of high-Reynolds-number supersonic boundary layers using the approximate deconvolution model and a rescaling and recycling technique. *Physics of Fluids*, 15(8):2398–2412, 2003. 36

[92] M. H. Baba-Ahmadi and G. Tabor. Inlet conditions for LES using mapping and feedback control. *Computers & Fluids*, 38:1299–1311, 2009. 36, 89

[93] F. Xiao, M. Dianat, and J. J. McGuirk. A recycling/rescaling method for LES inlet condition generation. In *Proc. of 8th ETMM Conference, Marseille, France, Vol. 1*, 2010. 37, 38, 39, 53, 89, 92, 95, 155

[94] B. E. Launder and D. B. Spalding. The numerical computation of turbulent flows. *Computer Methods in Applied Mechanics and Engineering*, Vol. 3:269–289, 1974. 38, 44, 61

[95] B. E. Launder and B. I. Sharma. Application of the energy-dissipation model of turbulence to the calculation of flow near a spinning disc. *Letters in Heat and Mass Transfer*, 1(2):131, 1974. 38, 42, 44, 61

[96] G. J. Page. DELTA User's Guide. Technical report, Department of Aeronautical and Automotive Engineering, Loughborough University, 1999. 41

[97] C. Rhie and W. Chow. Numerical study of the turbulent flow past an airfoil with trailing edge separation. *AIAA Journal*, 21:1525–1532, 1983. 41

[98] P. Birkby and G. J. Page. Numerical predictions of turbulent underexpanded sonic jets using a pressure-based methodology. *Proceedings of the Institution of Mechanical Engineers, Part G: Journal of Aerospace Engineering*, 215(3):165–173, 2001. 41, 51

[99] H. Salman, G. J. Page, and J. J. McGuirk. Prediction of lobed mixer vortical structures with a k-ϵ turbulence model. *AIAA J.*, Vol. 41(5):878–887, May 2003. 41, 51

[100] G. J. Page, J. J. McGuirk, L.R. Harper, and C.J. Penrose. Application of computational fluid dynamics to hot gas ingestion modelling. In *Proc. of Royal Aeronautical Society International Powered Lift Conference, London, UK*, Sep. 1998. 41, 42, 51

[101] X. Wu, G. J. Page, and J.J. McGuirk. Influence of nozzle modelling in LES of turbulent free jets. In *Proc. of 11th AIAA/CEAS Aeroacoustics Conference, Monterey, California, USA, AIAA-2005-2883*, pages 1–17, May, 2005. 41, 42, 51

[102] G. J. Page, H. Zhao, and J. J. McGuirk. A parallel multiblock Reynolds Averaged Navier-Stokes method for propulsion installation applications. In *Proc. of 12th International Symposium on Air Breathing Engines, Vol. 1*, pages 864–874, 1995. 42

[103] X. Wu, G. J. Page, and J.J. McGuirk. An approach to improve high-frequency noise prediction in LES of jets. In *Proc. of 12th AIAA/CEAS Aeroacoustics Conference, Mass., USA, AIAA-2006-2442*, 2006. 42, 50

[104] M.T. Trumper. *A Study of Nozzle Exit Boundary Layers in High Speed Jet Flows*. PhD thesis, Loughborough University, 2006. 42, 44

[105] W. P. Jones and B. E. Launder. The calculation of low-Reynolds-number phenomena with a two-equation model of turbulence. *International Journal of Heat and Mass Transfer*, 16(6):1119, 1973. 44, 45

[106] J. Smagorinsky. General circulation experiments with the primitive equations. *Monthly Weather Review*, pages 99–164, 1963. 47, 61

[107] E. R. van Driest. On turbulent flow near a wall. *Journal of Aeronautical Sciences*, Vol. 23(11):1007–1011, 1956. 48, 61

[108] W. H. Press et al. *Numerical recipes in FORTRAN 77: the art of scientific computing*. Cambridge University Press, Cambridge,UK, 1992. 49

[109] B. Van Leer. Towards the ultimate conservative difference scheme v. a second order sequel to godunov's method. *Journal of Computational Physics*, 32(1):101–136, 1979. 51

[110] J.H. Ferziger and M. Perić. *Computational Methods for Fluid Dynamics*. Springer, New York, 2002. 51

[111] J. H. Williamson. Low-storage runge-kutta schemes. *Journal of Computational Physics*, 35(1):48–56, 1980. 52

[112] S. Shahpar and L. Lapworth. PADRAM: PArametric Design and Rapid Meshing system for turbomachinery optimisation. In *Proc. of ASME Turbo Expo. Atlanta, Georgia, USA, ASME GT2003-38698*, 2003. 52, 57

[113] J. E. Bardina, P. G. Huang, and T. J. Coakley. Turbulence modeling validation,testing and development. Technical Report 110446, NASA Technical Memorandum, 1997. 58, 69

[114] I. Veloudis. *A Study of Subgrid Scale Modelling and Inflow Boundary Conditions for Large Eddy Simulation of Wall-bounded Flows*. PhD thesis, Loughborough University, 2006. 62

[115] G. Tabor and M.H. Baba-Ahmadi. Inlet Conditions for Large Eddy Simulation: A Review. *Computers & Fluids*, 39(4):553–567, 2010. 88

[116] T.A. Zang. Numerical simulation of the dynamics of turbulent boundary layers: Perspectives of a transition simulator. *Phil. Trans. Roy. Soc. Lond. A*, 336:95–102, 1991. 102

[117] J. C. R. Hunt, A. A. Wray, and P. Moin. Eddies, stream and convergence zones in turbulent flows. Technical Report CTR-S88, Center for Turbulence Research, 1988. 103

[118] Y. Dubief and F. Delcayre. On coherent-vortex identification in turbulence. *Journal of Turbulence*, 1:1–22, 2000. 103

[119] M. M. Gibson and B. E. Launder. On the calculation of horizontal, turbulent, free shear flows under gravitational influence. *Journal of Heat Transfer*, 98:81–87, 1976. 125

[120] S. E. Kim. Large eddy simulation using unstructured meshes and dynamic subgrid-scale turbulence models. In *Proc. of 34th Fluid Dynamics Conference and Exhibit, AIAA-2004-2548*, June 2004. 157